eISSN 2533-2260
Vol. 16 N. 2
March 2023

International Review of Automatic Control (IREACO)

Contents

Praise Worthy Prize

International Review of Automatic Control (IREACO)

The ***International Review of Automatic Control (IREACO)*** is a publication of the **Praise Worthy Prize S.r.l..**
The Review is published bimonthly, appearing on the last day of January, March, May, July, September, November.

Published and Printed in Italy by **Praise Worthy Prize S.r.l.,** Naples, March 31, 2023.

Praise Worthy Prize

International Review of Automatic Control (I.RE.A.CO.), Vol. 16, N. 2
ISSN 1974-6059 *March 2023*

Medium and Low-Level Energy Saving Control Strategies for Electric-Powered UAVs

Zeinab Hussein Keserwan[1], Majd Saied[2], Clovis Francis[3]

Abstract – *Flight endurance of an electric-powered Unmanned Aerial Vehicle (UAV) is restricted by its limited on-board energy, which might endanger the accomplishment of any mission it has been sent on. Therefore, the vehicle's energy consumption should be reduced as much as possible to prolong its flight. This paper deals with the minimization of the energy consumed by an electric-powered UAV as it tracks a desired target point by designing the necessary energy saving control techniques. Two approaches are proposed. The first one addresses the energy consumption problem by optimizing the UAV's low-level controller. The second approach makes use of the powerful Artificial Bee Colony algorithm to optimize the medium-level controller which guarantees not only target point tracking but also minimization of energy consumption. The effectiveness of both proposals is validated by simulations on MATLAB/Simulink.*

Keywords: *Unmanned Aerial Vehicle, Energy Optimization, Artificial Bee Colony algorithm, PID Controller Tuning*

Nomenclature

ABC	Artificial Bee Colony
BLDC	Brushless DC Motor
DC	Direct Current
KiBAM	Kinetic Battery Model
Li-Po	Lithium-Polymer
MOSFET	Metal-Oxide-Semiconductor Field-Effect Transistor
PD	Proportional Derivative
PID	Proportional Integral Derivative
PWM	Pulse Width Modulation
RMSE	Speed Root-Mean-Squared Error
SOC	State of Charge
UAV	Unmanned Aerial Vehicle
(x,y,z)	Hexarotor's Absolute Position
(Ø, θ, ψ)	Hexarotor's Euler Angles
g	Gravitational Acceleration
L	Motor Inductance
l	Hexarotor Arm Length
m	Hexarotor's Mass
(J_x, J_y, J_z)	Hexarotor's Inertia
(u_f, $\tau_Ø$, τ_θ, τ_ψ)	Virtual Inputs to Hexarotor Dynamics
f_i, τ_i	Thrust Force and Drag Moment of Motor i
ω_i	Angular Speed of Motor i
k_f	Thrust Coefficient
k_t	Drag Coefficient
V_a	Armature Voltage
I	Current Passing through Motor's Armature
R	Motor Internal Resistance
J	Motor-Propeller Inertia
C_s	Solid Friction
E	Counter Electromotive Force
τ_m	Motor's Torque due to Armature Voltage
τ_r	Load Friction Torque due to Propeller Drag
k_e	Electrical Constant
k_m	Mechanical Constant
k_r	Load Torque Constant
y_1	Capacity of Charges in Available Charge Well
y_2	Capacity of Charges in Bound Charge Well
h_1	Height of Available Charge Well
h_2	Height of Bound Charge Well
(c,k)	KiBaM Model Constants
i	Battery's Charge/Discharge Current
$C_{\max}$	Battery's Maximum Capacity
SOC	Battery's Maximum Capacity
V_{OC}	Battery's Open-Circuit Voltage
$K_{p_{i,i=x,y,z,\emptyset,\theta,\psi}}$	Proportional Gains
$K_{d_{i,i=x,y,z,\emptyset,\theta,\psi}}$	Derivative Gains
$\sigma_{p_{i,i=x,y,z,\emptyset,\theta,\psi}}$, $\sigma_{d_{i,i=x,y,z,\emptyset,\theta,\psi}}$	Saturation Functions
α	Threshold of Saturation Function
U	Desired Voltage to be applied to the BLDC motor
ω_r	Reference Speed
e_v	Velocity Error
K_L	Lyapunov-Based Controller Gain
s	Sliding Surface
k_s	Sliding Mode Controller Gain

 https://doi.org/10.15866/ireaco.v16i2.23120

e_ω	Speed Root-Mean-Squared Error
n	Number of Samples
E_b	Actual Percentage of Consumed Battery Energy
J_u	Control-Effort Index
T_s	Sampling Time
SS_{E_b}	Actual Energy Delivered Based Saving Score
SS_{J_u}	Control-Effort Based Saving Score
x_{ij}	Design Variable j at the i Food Source Position
$(x_j^{\min}, x_j^{\max})$	Predefined Limits for the j^{th} Design Variable
f	Cost function
u	Uniformly Distributed Random Variable in [-1,1]
p_i	Probability Value Associated with a Food Source
N_p	Number of Food Sources
ISE	Integrated Squared Error
e	Tracking Error
ST	Settling Time
OS	Overshoot
$f_{tracking}$, f_{energy}	Tracking and energy consumption parts of the Cost function
σ_x, σ_y, σ_z, σ_{OS}	Positive Parameters to be adjusted
ISU	Control Effort Index
λ	Trade-off Weight

I. Introduction

Over the last few years, the electric-powered unmanned aerial vehicle has become a major attraction.

It consists of a flying vehicle operated remotely or autonomously, and most commonly powered by a lithium-polymer (Li-Po) battery. It has been widely used over the recent years as it has proven to be effective for a wide range of civilian applications [1]-[3] in different areas and environment conditions [4]. However, the vehicle's achievement of any mission might be at risk due to its limited on-board energy that results in a limited flight endurance [5].

To overcome this risk, i.e., prolong the flight durations, several approaches have been proposed in the literature to reduce the energy consumption as much as possible. They mainly include improvement in UAV structure and material [6]-[9], usage of energy harvesting technologies [10]-[12], and design of energy saving control strategies [5], [13]. The work in [14] has considered the design of different control strategies applied to a generic UAV propulsion system to evaluate the impact of each control law on the energy consumption of the propulsion system. There are three well-defined levels of control in a UAV system.

The high Level consists of a path planning algorithm responsible for generating a reference trajectory to be followed by the UAV under some specifications such as minimizing energy consumption, avoiding obstacles, etc.

In [15], a flatness-based flight trajectory planning strategy was proposed to drive a quadrotor UAV from an initial position to a final one while minimizing the total energy consumed without hitting the actuator constraints.

The work in [16] considered the use of an improved A* algorithm for the real-time path planning of UAVs that guarantees high survival rates and low fuel consumption in a 3D large-scale battlefield. In [17], the authors' objective was to plan the path of a combat UAV in such a way that it ensures minimum probability of being found and minimum consumed fuel. They proposed the use of a Fitness-scaling Adaptive Chaotic Particle Swarm Optimization approach as a fast and robust approach for their path planning task. The medium level control consists of trajectory tracking control responsible for generating the desired thrusts and moments applied to the UAV to guarantee path following with bounded errors [18]. Some works in the literature have also exploited this level to address the problem of energy consumption. In [5], [19], [20] the control of a quadrotor UAV was achieved by minimizing a performance index that considers control efforts among other parameters. However, it is important to note that they do not take into account the real energy involved in the control strategy, but they rather reflect it by using the well-known control-effort index criterion. The low-level control consists of the UAV's propulsion system controller.

Its outputs are the desired voltages which should be applied to the motors so they rotate at the reference speeds and thus generate the desired thrusts and moments. The design of low-level controllers has mostly addressed the objective of making the motors rotate at desired speeds. Their design to achieve minimum energy consumption was slightly addressed in the literature although the propulsion systems are the most important source of energy consumption in a UAV. In [14], the authors designed several well-known control strategies to make the motor of a generic UAV propulsion system follow a given speed profile. After implementing each control strategy, the control-effort index and the actual percentage of energy consumed (among other criteria) were evaluated for comparison purposes of the different strategies.

The authors have concluded that it is not possible to reliably conclude about energy saving by analyzing the control-effort index alone as it is frequently encountered in the literature. In this work, our objective is to minimize the energy consumed by a Li-Po powered hexarotor UAV as it tracks a desired target point by designing the adequate medium and low-level controllers. To fulfil this objective, two approaches are proposed: the low-level approach and the medium-level approach. The low-level approach addresses the energy consumption problem by designing several low-level control strategies to determine the most energy saving one. This method is very similar to what has been done in [14]. The only differences are that: in our case, the desired speed profiles were evaluated from the desired thrusts and moments (medium-level controllers) rather

than being given, and the propulsion system was especially designed for the hexarotor UAV. On the other hand, since some works in the literature such as [21] and [22] have shown good results when using the Artificial Bee Colony (ABC) algorithm for the optimization of feedback gain controller parameters, the medium-level approach addresses the energy consumption problem by using this algorithm to find the optimal gains of the medium-level PD controllers which minimize a state and energy dependent cost function. The main contribution of this work in this regard is the proposition of a novel and appropriate form for the cost function.

The remaining part of this paper is organized as follows. Section II presents the model of the Li-Po powered hexarotor used for simulation. Section III elaborates the low-level approach, while Section IV elaborates the medium-level approach. The results obtained upon the MATLAB/Simulink implementation of both approaches are revealed and compared in Section V. The paper ends with conclusions and perspectives on future works in Section VI.

II. Li-Po Powered Hexarotor Model

The Li-Po powered hexarotor is a UAV with six rotors on which propellers are fixed. Its rotors are located at the ends of the arms of a symmetric body frame. The model which was used for the simulation of this vehicle consists of two parts: the hexarotor dynamic model and the propulsion system model.

II.1. Hexarotor Dynamic Model

The Newton-Euler method is adopted to derive the hexarotor's dynamic equations described as follows [23]:

$$\begin{aligned}
\ddot{x} &= (\cos\emptyset \sin\theta \cos\psi + \sin\emptyset \sin\psi)\frac{u_f}{m} \\
\ddot{y} &= (\cos\emptyset \sin\theta \sin\psi - \sin\emptyset \cos\psi)\frac{u_f}{m} \\
\ddot{z} &= (\cos\emptyset \cos\theta)\frac{u_f}{m} \\
\ddot{\emptyset} &= \frac{J_y - J_z}{J_x}\dot{\theta}\dot{\psi} + \frac{\tau_\emptyset}{J_x} \\
\ddot{\theta} &= \frac{J_z - J_x}{J_y}\dot{\emptyset}\dot{\psi} + \frac{\tau_\theta}{J_y} \\
\ddot{\psi} &= \frac{J_x - J_y}{J_z}\dot{\emptyset}\dot{\theta} + \frac{\tau_\psi}{J_z}
\end{aligned} \tag{1}$$

where x, y and z represent the hexarotor's absolute position, Φ, θ and ψ are the hexarotor's Euler angles known as the roll, pitch and yaw angles respectively. m is the hexarotor's mass, g is the gravitational acceleration, J_x, J_y and J_z are the diagonal elements of the hexarotor's inertia matrix. u_f, τ_Φ, τ_θ and τ_ψ are the four virtual inputs to the hexarotor dynamics described as linear combinations of the real inputs of the hexarotor, the motors thrusts and moments, and are given by:

$$\begin{aligned}
u_f &= \sum_{i=1}^{6} f_i \\
\tau_\emptyset &= l\left(-\frac{1}{2}f_1 + \frac{1}{2}f_2 + f_3 + \frac{1}{2}f_4 - \frac{1}{2}f_5 - f_6\right) \\
\tau_\theta &= l\frac{\sqrt{3}}{2}(f_1 + f_2 - f_4 - f_5) \\
\tau_\psi &= \tau_2 + \tau_3 + \tau_5 - \tau_1 - \tau_4 - \tau_6
\end{aligned} \tag{2}$$

l is the hexarotor's arm length, f_i and τ_i are respectively the thrust force and drag moment produced by motor i and are given by:

$$\begin{aligned}
f_i &= k_f \omega_i^2 \\
\tau_i &= k_t \omega_i^2
\end{aligned} \tag{3}$$

where ω_i is the angular speed of the motor i, and k_f and k_t are the thrust and drag coefficients respectively.

II.2. Propulsion System Model

Based on the generic UAV propulsion system proposed in [14], the Li-Po powered hexarotor's propulsion system consists of: a Li-Po battery, six BLDC motors with propellers, and a PID-PWM controlled buck converter for each motor. In the following, a brief overview of these components is presented and their corresponding models are introduced.

1) *BLDC Motor with Propellers*: The BLDC motor serves as the actuator of the hexarotor UAV system. Several authors in the literature have modelled this motor as a convectional DC motor. In this work, the equations used in [24] are adopted to model each of the six motor-propeller systems. They are as follows:

$$\begin{aligned}
V_a &= RI + L\frac{dI}{dt} + E \\
\tau_m &= J\frac{d\omega}{dt} + C_s + \tau_r \\
E &= k_e \omega \\
\tau_m &= k_m I \\
\tau_r &= k_r \omega^2
\end{aligned} \tag{4}$$

where V_a is the voltage across the motor'armature, I is the current passing through the motor's armature, R and L are the motor's internal resistance and inductance respectively, ω is the motor's angular speed, J is the motor-propeller inertia, C_s is the solid friction, E is the motor's counter electromotive force, τ_m is the motor's torque due to the voltage across it, τ_r is the load friction torque resulting from the propeller drag, k_e and k_m are the electrical and mechanical constants respectively, and K_r is the load torque constant (same as K_t).

2) *PID-PWM Controlled Buck Converter*: To make the BLDC motor rotate at different speeds, different voltages should be applied to its armature. However, the motor is supplied with a fixed voltage source which is the Li-Po battery. Therefore, a DC-DC

converter along with a voltage control block should be used to provide from the battery any desired armature voltage. In this work, the PID-PWM controlled buck converter used in [14] is adopted. Figure 1 illustrates its circuitry.

The buck converter transforms, due to the switching of its MOSFET, the fixed DC input from the battery to a lower variable DC output V_a which is to be applied to the armature. To make this output voltage V_a follow its desired value U, the PID-PWM controller is used to control the on and off switching of the MOSFET.

3) *Li-Po Battery*: The Li-Po battery is a dynamic system which features several chemical reactions, nonlinear behaviours and internal characteristics. Different models have been proposed in the literature to capture its performance and major characteristics. In this work, the hybrid model proposed in [25] which constitutes the KiBaM analytical model and an electrical circuit model is adopted. In the following, we introduce both of them.
   a) *KiBaM Model*: It is responsible for capturing the battery's chemical processes and the nonlinear capacity effects. From a mathematical point of view, it can be summarized as follows:

$$\begin{aligned} \frac{dy_1(t)}{dt} &= -i(t) + k[h_2(t) - h_1(t)] \\ \frac{dy_2(t)}{dt} &= -k[h_2(t) - h_1(t)] \\ h_1(t) &= \frac{y_1(t)}{c} \\ h_2(t) &= \frac{y_2(t)}{1-c} \end{aligned} \tag{5}$$

$$\begin{aligned} SOC(t) = 1 - \frac{1}{C_{max}}\Big(\int i(t)dt + \\ +(1-c)\big(h_2(t) - h_1(t)\big)\Big) \end{aligned} \tag{6}$$

where $y_1(t_0) = c \cdot C_{max}$ and $y_2(t_0) = (1-c)C_{max}$ are the initial conditions initial conditions, c and k are constants related to the KiBaM model, i is the battery's charge/discharge current, and C_{max} is the battery's maximum capacity. It is important to note that Eq. (5) depicts the battery's variation of charge, and Eq. (6) evaluates the battery's state of charge SOC which is the level of charge of the battery relative to its maximum capacity.

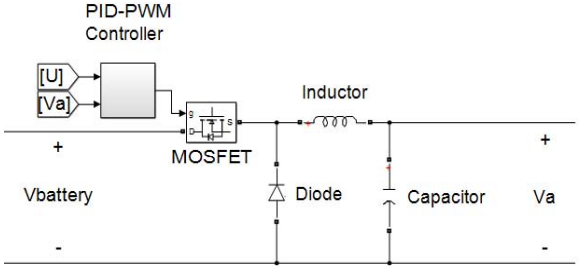

Fig. 1. PID-PWM controlled buck converter [14]

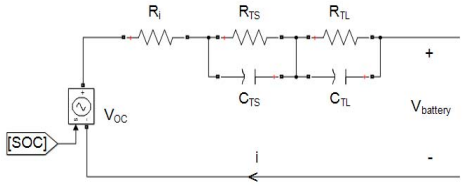

Fig. 2. Electrical model of the Li-Po battery

   b) *Electrical Circuit Model*: The electrical circuit model is responsible for capturing the *I-V* characteristics of the battery. As shown in Fig. 2, it is a series connection of a controlled voltage source V_{OC}, a resistor R_i, and two parallel *RC* networks [R_{TS},C_{TS}] and [R_{TL},C_{TL}]. The current i represents the battery's charge/discharge current, and the voltages $V_{battery}$ and V_{OC} represent the battery's terminal and open-circuit voltage respectively. It is important to note that the battery's open-circuit voltage is a function of its state of charge. In this work, the following equation which was used in [26] to estimate V_{OC} in terms of *SOC* is considered:

$$\begin{aligned} V_{OC}[SOC(t)] = A_0 e^{-A_1\, SOC(t)} + A_2 SOC^3(t) + \\ +A_3 SOC^2(t) + A_4 SOC(t) + A_5 \end{aligned} \tag{7}$$

where a_0, a_1, a_2, a_3, a_4 and a_5 are real coefficients to be adjusted.

III. Low-Level Approach

The low-level approach consists of designing several low-level control strategies that guarantee speed profile tracking to determine the most energy saving strategy. It also consists of designing a fixed-gain medium-level controller that guarantees target point tracking. In the following, the medium and low-level control strategies that were designed in the scope of this approach are presented. The indicators and saving scores used to evaluate the low-level control strategies performance are also introduced.

III.1. Medium-Level Control

The medium-level controller outputs are the desired thrust and moments, u_{fd}, $\tau_{\Phi d}$, $\tau_{\theta d}$, $\tau_{\psi d}$ to be applied to the hexarotor to track the desired states z_{ref}, x_{ref}, y_{ref}, Φ_{ref}, θ_{ref}, ψ_{ref}. For the first approach, a nested saturated PD controller with fixed gains is considered:

$$\begin{aligned} u_{fd} &= -\sigma_{p_z}\Big(K_{p_z}\big(z - z_{ref}\big)\Big) - \sigma_{d_z}\big(K_{d_z}\dot{z}\big) \\ \tau_{\psi_d} &= -\sigma_{p_\psi}\Big(K_{p_\psi}\big(\psi - \psi_{ref}\big)\Big) - \sigma_{d_\psi}\Big(K_{d_\psi}\dot{\psi}\Big) \\ \tau_{\phi_d} &= \frac{1}{g}\Big[\sigma_{p_y}\Big(K_{p_y}\big(y - y_{ref}\big)\Big) + \sigma_{d_y}\Big(K_{d_y}\dot{y}\Big) + \\ &\quad -\sigma_{p_\phi}\Big(K_{p_\phi}\big(\phi - \phi_{ref}\big)\Big) - \sigma_{d_\phi}\big(K_{d_\phi}\dot{\phi}\big)\Big] \\ \tau_{\theta_d} &= \frac{1}{g}\Big[-\sigma_{p_x}\Big(K_{p_x}\big(x - x_{ref}\big)\Big) - \sigma_{d_x}\big(K_{d_x}\dot{x}\big) + \\ &\quad -\sigma_{p_\theta}\Big(K_{p_\theta}\big(\theta - \theta_{ref}\big)\Big) - \sigma_{d_\theta}\big(K_{d_\theta}\dot{\theta}\big)\Big] \end{aligned} \tag{8}$$

where $K_{pi,\ i=x,y,z,\Phi,\theta,\psi,}$ and $K_{di,i=x,y,z,\Phi,\theta,\psi}$ are positive gains to be adjusted, $\sigma_{pi,\ i=x,y,z,\Phi,\theta,\psi}$ and $\sigma_{di,\ i=x,y,z,\Phi,\theta,\psi}$ are saturation functions defined as follows:

$$\begin{cases} \sigma(s) = \alpha & \text{if} \quad s > \alpha \\ \sigma(s) = s & \text{if} -\alpha < s < \alpha \\ \sigma(s) = -\alpha & \text{if} \quad s < -\alpha \end{cases} \tag{9}$$

III.2. Low-Level Control

To provide the hexarotor's dynamics with the desired values for u_f, τ_Φ, τ_θ and τ_ψ, its BLDC motors should follow certain speed profiles. The low-level controllers' outputs are the desired voltages U to be applied to the BLDC motors so they rotate at these desired speed profiles, and the PID-PWM controlled buck converters are in their turn responsible for making the actual voltages V_a applied to the motors follow their desired values.

It should be recalled that the hexarotor has six motors. Therefore, six low-level controllers should be designed. For the first approach, they are designed based on three different strategies: PID, Lyapunov, and sliding mode. In the following, we elaborate each strategy.

1) *PID Controller*: The classical PID controller is the most commonly used strategy for the low-level control. To make the BLDC motor rotate at its reference speed profile $\omega_r(t)$, the PID control law is formulated as follows:

$$U(t) = k_p e_v(t) + k_i \int e_v(t)dt + k_d \frac{de_v(t)}{dt} \tag{10}$$

where $e_v(t)$ is the velocity error given by $e_v(t)=\omega_r(t)-\omega(t)$, and k_p, k_i and k_d are positive gains to be adjusted.

2) *Lyapunov Based Controller*: The Lyapunov theory is a widely considered model-based tool that allows the design of stable controllers. To design a Lyapunov based controller for a certain system, the system's dynamics and equilibrium point should be identified first. Then, a control law should be proposed based on the dynamics. Finally, the closed-loop system in the presence of this control law should be proved to be stable in the Lyapunov sense. Using Eq. (4), and taking into consideration that the BLDC motor has very small inductance, the motor-propeller dynamic equation can be derived as follows:

$$\dot{\omega} = bV_a - a_0 - a_1\omega - a_2\omega^2 \tag{11}$$

where $a_0=C_s/J$, $a_1=k_e k_m/JR$, $a_2=k_r/J$ and $b=k_m/JR$. The equilibrium point in the case of the BLDC motor is defined as $\tilde{\omega} = \omega - \omega_r$ where ω_r is the reference speed. Based on the dynamics and equilibrium point, let the control action be given by:

$$U = \frac{1}{b}(a_0 + a_1\omega + a_2\omega^2 - K_L\tilde{\omega}) \tag{12}$$

where K_L is a positive gain to be adjusted. In the presence of the proposed control action, the closed loop system becomes:

$$\begin{gathered} \dot{\omega} = b\frac{1}{b}(a_0 + a_1\omega + a_2\omega^2 - K_L\tilde{\omega}) + \\ -a_0 - a_1\omega - a_2\omega^2 = -K_L\tilde{\omega} \end{gathered} \tag{13}$$

Consider the following Lyapunov candidate function $V = 1/2\ \tilde{\omega}^2$ and its corresponding derivative $\dot{V} = \tilde{\omega}\dot{\tilde{\omega}}$. Based on the Lyapunov theorem, a system is asymptotically stable if the derivative of the Lyapunov function is negative definite. Along the system's trajectories, $\dot{V} = \tilde{\omega}(\dot{\omega} - \dot{\omega}_r) = \tilde{\omega} = -K_L\tilde{\omega}^2 < 0$. Thus, the asymptotic stability of the controller given in Eq. (12) has been proved. It can now serve as a Lyapunov based controller for the motor-propeller system.

3) *Sliding Mode Controller*: The sliding mode controller is a robust state feedback controller that uses switching control actions to constrain the system states to stay on a sliding surface *s*. As long as the system is on this surface, it will exhibit its desirable features. To design a sliding mode controller, the first step is to choose the sliding surface s in terms of tracking errors. The surface should be chosen in such a way that the tracking errors exponentially converge to zero when s=0. The second step is to design a control law that satisfies the sliding condition $s\dot{s} < 0$. In the case of the motor-propeller system, the sliding surface can be defined as $s=\omega-\omega_r$. Thus, the time derivative of *s* is as follows:

$$\dot{s} = \dot{\omega} - \dot{\omega}_r = \dot{\omega} = bV_a - a_0 - a_1\omega - a_2\omega^2 \tag{14}$$

The control input that ensures s = 0 is given by:

$$\hat{U} = \frac{1}{b}(a_0 + a_1\omega + a_2\omega^2) \tag{15}$$

To satisfy the sliding condition, a term consisting of the sign function is added. The overall sliding mode control input becomes as follows:

$$U = \hat{U} - \frac{k_s}{b}sgn(s) \tag{16}$$

where k_s is a positive gain to be adjusted. The switching behavior of the sign function makes the sliding mode controller U robust to parameter uncertainties and external disturbances. However, it also leads to undesirable chattering, i.e., high-frequency oscillations of the control input that lead to an oscillating response of the motor-propeller system. To reduce the chattering effect, the sign function in U should be replaced by a saturation function $sat(s/\Phi)$. This will replace the on-off behavior of the sign function by a linear behavior in $[-\Phi,\Phi]$. Then the controller becomes as follows:

$$U = \widehat{U} - sat\left(\frac{S}{\Phi}\right) \quad (17)$$

where Φ is a positive design constant to be chosen.

III.3. Evaluation Criteria

To evaluate and compare the different strategies designed for the low-level control, the indicators and saving scores proposed in [14] are used. They are briefly defined in the following.

1) *Performance Indicators*: Three indicators can be computed for each control strategy at the end of simulation:
   - Speed Root-Mean-Squared Error (RMSE): It is given in discrete time by:

$$e_\omega = \sqrt{\frac{\sum_{j=1}^{n}(\omega(j) - \omega_r(j))^2}{n}} \quad (18)$$

   where n is the total number of samples. If this error is low, the low-level controller is said to be efficient in terms of speed profile tracking.
   - Actual Percentage of Consumed Battery Energy: It is the real percentage of energy consumed from the Li-Po battery. It is given at each instant by:

$$E_b(t) = 100 - 100\,SOC(t) \quad (19)$$

   - Control-Effort Index: It has been used a lot in the literature to reflect energy consumption. It is given in discrete time by:

$$J_u = T_s \sum_{j=1}^{n} U^2(j) \quad (20)$$

   where T_s is the sampling time.
2) *Saving Scores*: To compare the classical PID controller, which is considered as the reference controller, with the other low-level control strategies, two saving scores can be computed for each of them:
   - *Actual Energy Delivered Based Saving Score*: It takes into account the actual percentage of consumed battery energy in the presence of the PID controller $E_{b(PID)}$ and that in the presence of any of the other controllers $E_{b(CONT)}$. It is given by:

$$SS_{E_b} = E_{b(PID)} - E_{b(CONT)} \quad (21)$$

   A null value for this saving score indicates that there is neither energy saving nor loss between both controllers. On the other hand, a positive value for this saving score indicates that the considered controller saves energy with respect to the PID controller, and a negative value indicates that it wastes energy with respect to it.
   - *Control-Effort Based Saving Score*: It takes into account the control-effort indices of the PID controller $J_u(PID)$ and any of the other controllers $J_u(CONT)$. It is given by:

$$SS_{J_u} = \frac{J_u(PID) - J_u(CONT)}{J_u(PID)} \times 100 \quad (22)$$

   It is computed to check whether it agrees with SS_{Eb}.

IV. Medium-Level Approach

The medium-level approach consists of using the ABC algorithm to find the optimal gains of the medium-level PD controller (Eq. (8)) which minimizes a state and energy dependent cost function. It also consists of using the most energy saving low-level controller found in the low-level approach for speed profile tracking. In the following, the theory of the ABC algorithm is presented with its application for the tuning of the medium-level PD controllers.

IV.1. Artificial Bee Colony Algorithm

The ABC algorithm is a population-based optimization technique that is capable of handling constrained optimization problems with fast convergence and with a good quality of solutions [27]. It is based on the intelligent behaviour of a honeybee swarm. It searches for the optimal solution of an optimization problem by using a colony of artificial bees that searches for food sources [28]. In the following, an overview of the colony of artificial bees is given. The characteristics of the food source and their relation with the actual solution of the optimization problem are discussed with the concept of the search process.

1) *Colony of Artificial Bees*: The colony of artificial bees consists of three types of bees:
   - *Employed Bees*: These have the responsibility of exploiting the food sources visited by them before and giving information to the onlooker bees.
   - *Onlooker Bees*: These are the bees that wait in the hive (or dance area) to choose a food source based on information from the employed bees.
   - *Scout Bees*: They are employed bees whose food source has been abandoned. They become scouts and start to search for a new food source.
2) *Food Source*: A food source is characterized by its position and nectar amount. The position represents a possible solution to the optimization problem. On the other hand, the nectar amount reflects the quality (fitness) of the associated solution.
3) *Search Process*: The search process carried out by the artificial bees can be summarized as follows:
   - *Initialization*: A set of N_p food source positions are randomly selected by the employed bees, and their nectar amounts are determined. The random selection of food source positions is modeled as follows:

$$x_{ij} = x_j^{min} + rand(0,1)\left(x_j^{max} - x_j^{min}\right) \quad (23)$$

where i varies from 1 to N_p, j varies from 1 to the number D of design variables, and x_j^{min} and x_j^{max} are the predefined minimum and maximum limits for the j^{th} design variable. The nectar amount of each food source position $X_i=(x_{ij})_{j=1,\ldots,D}$ is calculated according to the following expression:

$$fit(X_i) = \begin{cases} \dfrac{1}{1+f(X_i)} & if\ f(X_i) \geq 0 \\ 1+|f(X_i)| & if\ f(X_i) < 0 \end{cases} \quad (24)$$

where $f(X_i)$ represents the value of a cost function f at X_i.

- *Search Process of the Employed Bees*: Every employed bee goes to the food source position already visited in the previous cycle since it exists in its memory. Next, it chooses a new food source position from the neighborhood by modifying the position in its memory. The modification of the food source position X_i is modeled as follows:

$$x'_{ij} = x_{ij} + u(x_{ij} - x_{kj}) \quad (25)$$

where u is a uniformly distributed random variable in [-1,1], j is any number between 1 and D, and k is any number between 1 and N_p but not equal to i. It is important to note that if a design variable produced by Eq. (25) exceeds its predetermined limit, it will be set to its limit value. Then, the employed bee tests the nectar amount of the new food source. Provided that its nectar amount is higher than that of the previous one, the bee memorizes the new position and forgets the old one.

- *Search Process of the Onlooker Bees*: After all the employed bees complete their search process, they share the nectar and position information of the food sources with the onlooker bees on the dance area. Each onlooker bee analyses all the information and chooses a food source based on the probability value associated with that food source which is given by:

$$p_i = \frac{fit(X_i)}{\sum_{i=1}^{N_p} fit(X_i)} \quad (26)$$

After that, as in the case of an employed bee, the onlooker bee produces a modification on the position in its memory and checks the nectar amount of the new food source position. Provided that its nectar amount is higher than that of the previous one, the bee memorizes the new position and forgets the old one.

- *Search Process of the Scout Bees*: If a food source is abandoned by the bees, this step will be executed. The employed bee of the abandoned food source automatically becomes a scout and starts searching for a new source. The scout will actually replace the abandoned position by a new randomly produced position (as in the initialization step). It is important to note that a food source is assumed to be exhausted and thus abandoned when it cannot be further improved through a predefined number of cycles called limit.
- *Storage of Best Food Source*: The food source position with the best fit (highest nectar amount or lowest cost) among the N_p food sources is stored. Then steps (2), (3), (4), and (5) are repeated until a stopping criterion is met.

IV.2. Problem Formulation

The goal is to find the gains of the medium-level PD controller (Eq. (8)) that guarantee not only target point tracking but also minimization of energy consumption.

This issue is formulated as an offline optimization problem and is solved using the ABC algorithm. In the following, The main elements of the formulated problem which are the design variables and the cost function are discussed.

1) *Design Variables*: To simplify the problem, the gains that are related to the hexarotor's absolute position (K_{pz}, K_{dz}, K_{py}, K_{dy}, K_{px} and K_{dx}) were considered as the design variables of the optimization problem, so $D = 6$. On the other hand, the gains that are related to the hexarotor's Euler angles were set to fixed values.
2) *Cost Function*: A cost function made up of two parts is designed: a part that considers the tracking performance of the design variables and a part that considers their energy consumption. The ABC algorithm should minimize the designed cost function to find the desired optimal gains. In the following, each part of the designed cost function is discussed. It will be then shown how they are integrated into the overall function.
   a) *Target Point Tracking Part*: The criteria used in [21] is adopted to reflect the tracking performance of the design variables, i.e., their ability in making the hexarotor's absolute position (x,y,z) reach its desired reference. These criteria are defined as follows:
      - Integrated Squared Error (ISE): It is given by:

$$ISE = \int_0^{\infty} e^2(t)dt \quad (27)$$

where $e(t)$ is the tracking error, i.e., the difference between the process variable and its reference value.

- Settling Time (ST): It is the time that it takes for the absolute error $|e(t)|$ to come within 2% of the reference value.
- Overshoot (OS): It is the amount that the process variable overshoots its reference value

expressed as a percentage of the reference value. It is considered that a good tracking performance for *x*, *y* and *z* is described by the following: minimum settling times, overshoots that do not exceed 5% and minimum integrated squared errors. Instead of simply weighting the criteria by constant coefficients and summing them up as is the case in [22], the tracking part of the cost function is designed as follows:

$$f_{tracking} = \frac{1}{(x_{ref} - x_0)^2}\left(e^{\frac{ST_x}{\sigma_x}} + e^{\frac{OS_x - 0.05}{\sigma_{OS}}}\right) ISE_x + \\ + \frac{1}{(y_{ref} - y_0)^2}\left(e^{\frac{ST_y}{\sigma_y}} + e^{\frac{OS_y - 0.05}{\sigma_{OS}}}\right) ISE_y + \\ + \frac{1}{(z_{ref} - z_0)^2}\left(e^{\frac{ST_z}{\sigma_z}} + e^{\frac{OS_z - 0.05}{\sigma_{OS}}}\right) ISE_z \quad (28)$$

where (x_0,y_0,z_0) is the initial position of the hexarotor, σ_x, σ_y and σ_z and are positive parameters to be adjusted depending on how strongly the settling times should be minimized, and σ_{OS} is a positive parameter to be adjusted depending on how strongly the overshoots should be limited to a maximum of 5%. In this manner, if the settling time is late and/or the overshoot exceeds 5%, the integrated squared error will be given a high weight. Otherwise, it will be given a low weight. Moreover, by minimizing $f_{tracking}$, the ABC algorithm will favor the values of K_{pz}, K_{dz}, K_{py}, K_{dy}, K_{px}, and K_{dx} that minimize the integrated square errors while ensuring, at the same time, minimum settling times and acceptable overshoots. It is important to note that the factors, which are related to the initial position and reference position, are for normalization purposes only.

b) *Energy Consumption Part*: The control-effort index used in [21] is adopted to reflect the energy consumption of the design variables. It is given by:

$$ISU = \int_0^\infty U^2(t)dt \quad (29)$$

where $U(t)$ is the control input. The control inputs that are affected by the design variables are u_{fd}, the first portion of $\tau_{\Phi d}$ and the first portion of $\tau_{\theta d}$. Therefore, the control-effort indices of these inputs are only considered and are denoted by ISU_z, ISU_y and ISU_x respectively. The energy consumption part of the cost function is designed as follows:

$$f_{energy} = (x_{ref} - x_0)^2 ISU_x + (y_{ref} - y_0)^2 ISU_y + \\ + 0.1(z_{ref} - z_0)^2 ISU_z \quad (30)$$

In this manner, by minimizing f_{energy}, the ABC algorithm will favor the values of K_{pz}, K_{dz}, K_{py}, K_{dy}, K_{px}, and K_{dx} that minimize the control-effort indices. It is important to note that the factors multiplying the control efforts are only for normalization purposes.

c) *Overall Cost Function*: To track the desired target point more efficiently, more energy is needed. Therefore, the gains that simultaneously guarantee the most efficient target point tracking and the least consumption of energy don't exist, and a trade-off should be made between these two desirable incompatible objectives. For this reason, The two parts of the cost function are given complementary weights λ and 1-λ where λ belongs to [0; 1]. Thus, the overall cost function becomes as:

$$f = \frac{1}{15}(\lambda f_{tracking} + (1 - \lambda) f_{energy}) \quad (31)$$

where the factor 1/15 was only used to step-down the values taken by f. In this manner, the more we care about tracking efficiency, the higher we will set the value of λ. On the other hand, the more we care about energy consumption, the lower we will set the value of λ.

V. Simulations and Results

It is considered that the Li-Po powered hexarotor is initially at (-8; -2; 0), and the target point that it should reach while stabilizing its Euler angles is set at (2; 2; 3).

Using the MATLAB/Simulink simulation environment, the vehicle's model is implemented and the low-level and medium-level approaches are applied. In the following, the implementation of each approach is discussed, and the results are analyzed and compared.

V.1. Low-Level Approach

First, the medium-level controller (Eq. (8)) and the low-level controllers (Eqs. (10), (12) and (16)) are tuned. Regarding the medium-level controllers, they are tuned in the absence of the low-level control scheme, i.e., it is assumed that the BLDC motors perfectly follow their desired speed profiles.

Table I shows the gain values obtained by trial and error that yield to a good target point tracking and stabilization of the Euler angles.

Regarding the low-level controllers, they are tuned in the absence of the medium-level control scheme, i.e., the motors are tuned to follow a set of practical reference speeds that were not calculated based on the medium-level controllers. Table II shows the gains, obtained by trial and error, of the PID, Lyapunov based and sliding mode strategies that yield to the best speed profile tracking.

TABLE I
GAINS OF THE MEDIUM-LEVEL PD CONTROLLERS

Parameter	Value	Parameter	Value
K_{pz}	120	$K_{p\psi}$	50
K_{dz}	50	$K_{d\psi}$	20
K_{py}	1	$K_{p\Phi}$	50
K_{dy}	4	$K_{d\Phi}$	20
K_{px}	2	$K_{p\theta}$	50
K_{dx}	5	$K_{d\theta}$	20

TABLE II
GAINS OF THE LOW-LEVEL CONTROLLERS

Controller	Parameter	Value
PID	K_p	0.003
	K_i	0.09
	K_d	0
Lyapunov Based	K_L	30
Sliding Mode	K_S	90000
	Φ	2400

Then, the overall model of the Li-Po powered hexarotor is controlled using:

- *Case 1:* Medium-level PD controllers with the PID strategy for low-level control.
- *Case 2:* Medium-level PD controllers with the Lyapunov based strategy for low-level control.
- *Case 3:* Medium-level PD controllers with the sliding mode strategy for low-level control.

For the three low level controllers cases, the responses of the hexarotor's degrees of freedom (x; y; z; Φ; θ; ψ) and motor speeds (ω_1; ω_2; ω_3; ω_4; ω_5; ω_6) were very similar. Therefore, only those of the first controller are shown in Figs. 3 and 4.

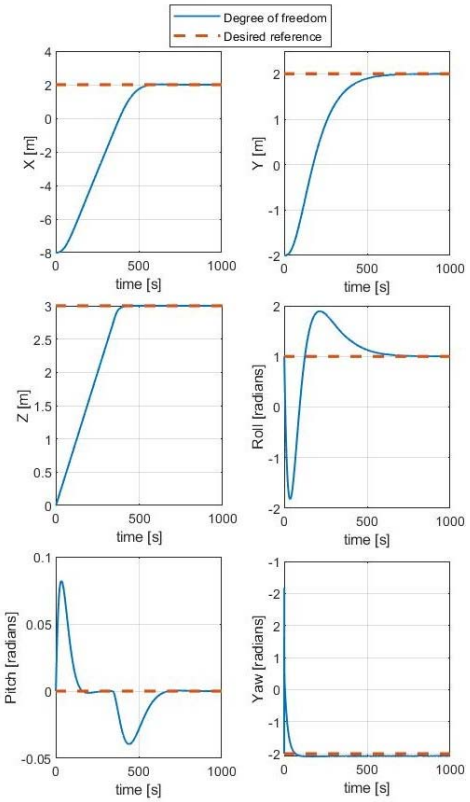

Fig. 3. Responses of the hexarotor's degree of freedom with PID low-level controller

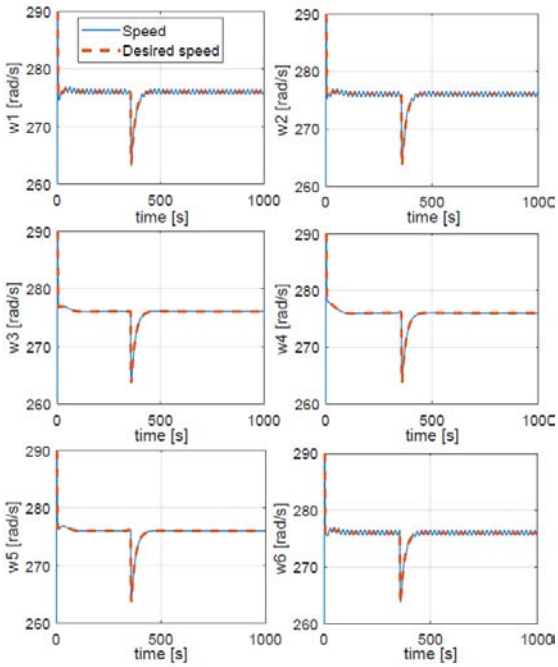

Fig. 4. Responses of the BLDC motors' speeds with PID low-level controller

Figure 3 illustrates how each degree of freedom of the hexarotor (solid blue) tracks its desired reference (dashed red), and Fig. 4 illustrates how the speed of each BLDC motor (solid blue) tracks its desired reference (dashed red). Based on these results, it is shown that the medium-level controller makes the hexarotor track successfully its target point while stabilizing its Euler angles, and the low-level controllers make the BLDC motors track successfully their desired speed profiles. For each low-level controller, the criteria detailed previously in Section III-C is detailed at the end of the simulations. The indicators are listed in Table III and the saving scores are listed in Table IV. Based on Table III data, it can be shown that the Lyapunov based and sliding mode controllers have lower speed $RMSE_s$ than those of the PID controller. Thus, they are more efficient than the PID controller in terms of speed tracking. However, based on Table IV data, it can be shown that the Lyapunov based and sliding mode controllers have negative values for their SS_{Eb}. Therefore, they consume more energy than the PID controller. Hence, the most energy saving low-level control strategy is the PID controller. It did consume the least amount of energy, but this came at the cost of being the least efficient in terms of speed tracking. Moreover, as shown in Table IV, SS_{Eb} and SS_{Ju} have the same sign for each case of low-level control. Therefore, in contrary to [14], they will give the same indication about energy consumption in any case.

V.2. Medium-Level Approach

Based on Section IV, the ABC algorithm is coded to find the optimal gains of the medium-level PD controller that minimize the overall cost function for a certain value

of λ. The algorithm stopping criteria corresponds to the case where the best cost can no longer be minimized or when the number of iterations exceeds its maximum limit *MaxIt*. The parameters related to the algorithm and those related to the cost function are set as shown in Table V.

To validate our approach, the ABC algorithm is used to find the optimal gains of three different scenarios:

- *Scenario 1:* The medium-level controllers should guarantee the most efficient target point tracking only. Therefore, we let λ=1;
- *Scenario 2:* The medium-level controllers should guarantee target point tracking and minimization of energy consumption. Therefore, λ is decreased to 0.6;
- *Scenario 3:* The medium-level controllers should guarantee more reduction in energy consumption than they do in Scenario 2. Therefore, λ is decreased to 0.4.

The optimal gains found in each scenario are listed in Table VI. To test and validate the behavior of the optimal gains found in each scenario, the overall model of the Li-Po powered hexarotor is controlled using:

- *Case 1:* Medium-level PD controllers tuned to the optimal gains of Scenario 1 in addition to the low-level PID controllers
- *Case 2:* Medium-level PD controllers tuned to the optimal gains of Scenario 2 in addition to the low-level PID controllers
- Case 3: Medium-level PD controllers tuned to the optimal gains of Scenario 3 in addition to the low-level PID controllers

It is important to note that, in all the three cases, the gains of the medium-level PD controllers were set to their values listed in Table I. Since the behavior of these gains is being studied, the responses of *x*, *y* and *z* are analyzed only. It is important to note that the Euler angles were stabilized in all three cases.

Figures 5, 6 and 7 illustrate how the hexarotor's position (solid blue) tracks its desired reference (dashed red) in cases 1, 2 and 3 respectively. Based on the figures, the optimal gains of all three scenarios are successful in making the hexarotor track its desired target point.

To compare the tracking efficiencies and energy consumption among the three cases, the following criteria are evaluated for each case: ST_x, ST_y, ST_z, OS_x, OS_y, OS_z, ISE_x, ISE_y, ISE_z and E_b. By decreasing λ (from Case 1 to Case 3), the settling times were delayed, and the integrated squared errors increased. However, the percentage of actual energy consumed decreased.

Therefore, by decreasing λ, the optimal gains found by the ABC algorithm guarantee lower energy consumption but less efficient target point tracking. When the ABC algorithm finds the optimal gains that minimize the overall cost function for a certain value of λ, it is actually finding the gains that guarantee a trade-off between efficient target tracking and minimization of energy consumption. By decreasing λ, the ABC algorithm finds the gains that minimize the energy consumed rather than increasing the tracking efficiency, and vice versa.

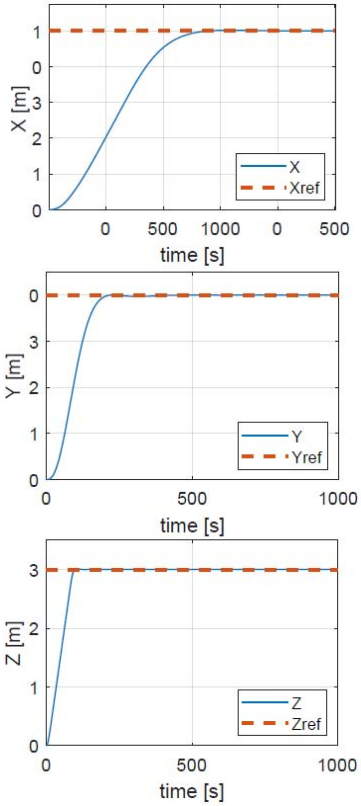

Fig. 5. Responses of x, y and z in Case 1

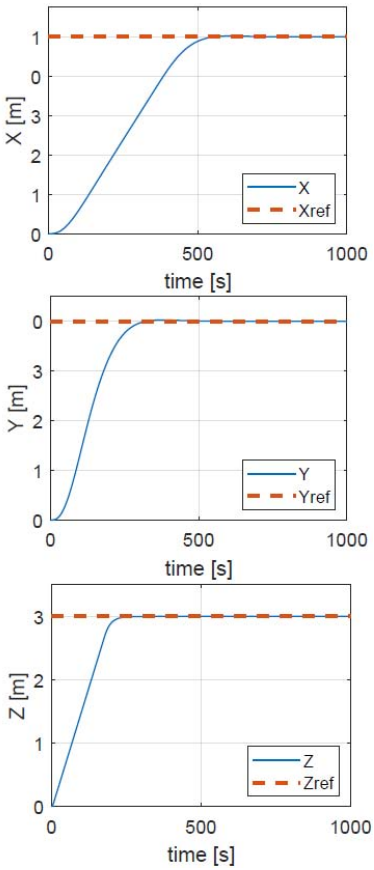

Fig. 6. Responses of x, y and z in Case 2

TABLE III
INDICATORS

Controller	$e_{\omega 1}$(rad/s)	$e_{\omega 2}$(rad/s)	$e_{\omega 3}$(rad/s)	$e_{\omega 4}$(rad/s)	$e_{\omega 5}$(rad/s)	$e_{\omega 6}$(rad/s)	E_b(%)	J_u(V^2 s)
PID	11.2833	11.1226	10.3651	9.7377	10.6154	11.0383	19.5997	99904
Lyapunov	11.2595	11.1043	10.3511	9.7316	10.6	11.0195	19.6472	100305
Sliding Mode	11.2589	11.1043	10.3509	9.7313	10.5997	11.0194	19.6551	100540

TABLE IV
SAVING SCORES WITH RESPECT TO THE PID CONTROLLER

Controller	SS_{Eb}(%)	SS_{Ju}(%)
Lyapunov Based	-0.0476	-0.4012
Sliding Mode	-0.0555	-0.6365

TABLE V
ABC PARAMETERS

Parameter	Value	Parameter	Value
N_p	100	σ_x	6.4
limit	150	σ_y	6.4
MaxIt	1000	σ_z	5.4
		σ_{OS}	0.02

TABLE VI
OPTIMAL GAINS OBTAINED IN EACH SCENARIO

Scenario	K_{pz}	K_{dz}	K_{py}	K_{dy}	K_{px}	K_{dx}
1	60.8251	11.4068	3.4379	6.7180	1.2767	4.0348
2	59.2259	25.9863	1.7614	4.7670	2.1	5.0095
3	74.8375	33.4401	1.1716	3.8659	2.5827	5.5918

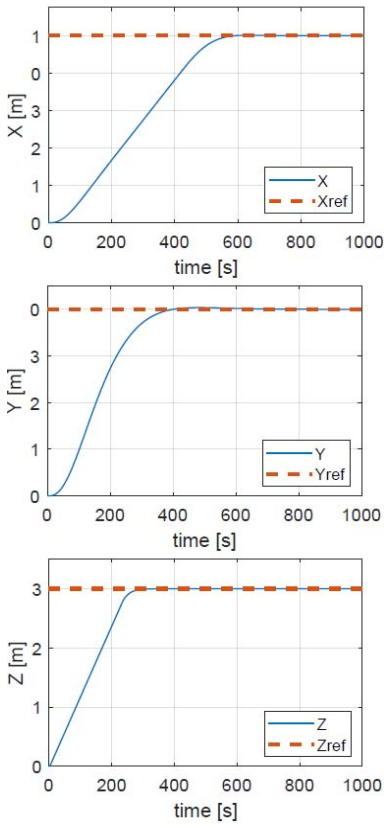

Fig. 7. Responses of x, y and z in Case 3

V.3. Discussion

The different simulations above were carried out obtaining a quantitative comparison between the different applied controllers and the two strategies. Conclusions about the energy saving in the low-level approach were drawn taking into account the consumed energy and a control-effort based index. It was found that the most energy saving strategy (PID) was the least efficient in terms of speed profile tracking. Therefore, speed profile tracking and minimum energy consumption are two incompatible objectives of low-level control, and designers should make a trade-off between them. On the other hand, each controller of the tested ones has its own advantages depending on the situation; for example, the sliding mode controller could be a suitable choice when robustness against perturbations is the main objective, even if it results in higher energy consumption. The PID controller offers generally a cost-effective solution as it does not require a mathematical model of the system, providing a significant cost/benefit ratio.

In the medium level approach, the ABC algorithm was used to tune the gains of the medium-level PID controllers to guarantee both target point tracking and minimum energy consumption. Since energy consumption was addressed using the control effort index in this method, and since this index does not actually reflect the real energy consumed, the low-level control scheme developed in the first method was still considered to evaluate the percentage of energy consumed and thus validate energy consumption minimization. It was found that the ABC algorithm was efficient and suitable for finding the optimal gains that guarantee a trade-off between efficient target tracking and minimization of energy consumption.

VI. Conclusion

Currently, most the UAVs using electric propulsion are powered with Lithium Polymer batteries. Based on this energy-limited scenario, in this paper, we proposed minimizing the energy consumed by an electric-powered UAV as it tracks a desired target point by designing its controllers in an energy saving manner and implementing them for a generic UAV propulsion system including the lithium polymer battery and the energy source. In a first attempt, the energy consumption problem was addressed through the design of the UAV's low-level control. In a second attempt, the energy consumption problem was addressed through the design of the UAV's medium-level control by using the ABC algorithm.

Based on the obtained results, in future works, we intend to test both approaches experimentally on a real Li-Po powered hexarotor UAV. We also intend to enhance both approaches and use them to minimize the energy consumed by an UAV as it executes a more complex mission such as being part of a formation flight which should converge to a target point while avoiding obstacles and collisions.

References

[1] H. Shakhatreh et al., Unmanned Aerial Vehicles (UAVs): A Survey on Civil Applications and Key Research Challenges, *IEEE Access*, Vol. 7:48572-48634, 2019.

[2] Uc Ríos, C., Teruel, P., Use of Unmanned Aerial Vehicles for Calibration of the Precision Approach Path Indicator System, (2021) *International Review of Aerospace Engineering (IREASE)*, 14 (4), pp. 192-200. doi: https://doi.org/10.15866/irease.v14i4.20709

[3] Salman, S., Al Dhaheri, M., Dawson, P., Anavatti, S., Autonomous Water Sampling Payload Design, (2020) *International Review of Aerospace Engineering (IREASE)*, 13 (3), pp. 120-125. doi: https://doi.org/10.15866/irease.v13i3.18374

[4] Alnuaimi, M., Perhinschi, M., Al-Sinbol, G., Immunity-Based Framework for Autonomous Flight in GNSS-Denied Environment, (2019) *International Review of Aerospace Engineering (IREASE)*, 12 (6), pp. 239-249. doi: https://doi.org/10.15866/irease.v12i6.16215

[5] F. Morbidi, R. Cano and D. Lara, Minimum-Energy Path Generation for a Quadrotor UAV, *IEEE International Coference on Robotics and Automation*, Stockholm, Sweden, May 2016.

[6] S. Driessens and P. Pounds, The Triangular Quadrotor: A More Efficient Quadrotor Configuration, *IEEE Transactions on Robotics*, Vol. 31:1517-1526, 2016.

[7] M. Ryll, H. Bulthoff and P. Giordano, A Novel Overactuated Quadrotor Unmanned Aerial Vehicle: Modeling, Control and Experimental Validation, *IEEE Transactions on Control Systems Technology*, Vol. 23:540-556, 2015.

[8] D. Gurdan, J. Stumpf, M. Achtelik, K. Doth, G. Hirzinger and D. Rus, Energy-efficient Autonomous Four-rotor Flying Robot Controlled at 1 khz, *IEEE International Conference on Robotics ad Automation*, Rome, Italy, April 2007.

[9] J.F. Roberts, J.-C. Zufferey and D. Floreano, Energy Management for Indoor Hovering Robots, *IEEE/RSJ International Conference on Intelligent Robots ad Systems*, Nice, France, September, 2008.

[10] A. Koszewnik and D. Oldziej, Performance assessment of an energy harvesting system located on a copter, *The European Physical Journal Special Topics*, Vol. 228:1677-1692, 2019.

[11] R. Sowah, M. Acquah, A. Ofoli, G. Mills and K. Koumadi, Rotational Energy Harvesting To Prolong Flight Duration of Quadcopters, *IEEE Transactions on Industry Applications*, Vol. 53:4965-4972, 2017.

[12] D. Gandolfo, L. Salinas, A. Brandao, and J. Toibero, Path Following for Unmanned Helicopter: An Approach on Energy Autonomy Improvement, *Information Technology and Control*, Vol. 45:86-98, 2016.

[13] D. Gandolfo, L. Salinas and J. Toibero, Energy Evaluation of Low-Level Cotrol in UAVs powered by Lithium Polymer Battery, *ISA Transactions*, Vol. 71:563-572, 2017.

[14] A. Chamseddine, Y. Zhang, C.A. Rabbath, C. Join, and D. Theilliol, Flatness-based Trajectory Planning/Replanning for a Quadrotor Unmanned Aerial Vehicle, *IEEE Transactions o Aerospace and Electronic Systems*, Vol. 48:2832-2848, 2012.

[15] W. Zhang, W. Wang, N. Chen and C. Wang, Efficient UAV path planning with multiconstraints in a 3D large battlefield environment, *Mathematical Problems in Engineering*, 1-12, 2014.

[16] Y. Zhang, L. Wu and S. Wang, UCAV Path Planning by Flitness-Scaling Adaptive Chaotic Particle Swarm Optimization, *Mathematical Problems in Engineering*, 2013.

[17] Mlayeh, H., Ghachem, S., Nasri, O., Ben Othman, K., Stabilization of a Quadrotor Vehicle Using PD and Recursive Nonlinear Control Techniques, (2021) *International Review of Aerospace Engineering (IREASE)*, 14 (4), pp. 211-219. doi: https://doi.org/10.15866/irease.v14i4.19739

[18] D. Cabecinhas, R. Naldi, L. Marconi, C. Silvestre and R. Cunha, Robust take-off for a Quadrotor Vehicle, *IEEE Transactions on Robotics*, Vol. 28: 734-742, 2012.

[19] M. Ryll, H. H. Bulthoff, and P. R. Giordano, Modeling and control of a quadrotor UAV with tilting propellers, *IEEE International Coference on Robotics and Automation*, Saint Paul, MN, USA, May 2012.

[20] S. Kolawole and D. Haibin, Satellite Formation Keeping via Chaotic Artificial Bee Colony, *Aircraft Engineering and Aerospace Technology*, Vol. 89: 246-256, 2017.

[21] M. Abachizadeh, M. Yazdi, and A. Yousefi-Koma, Optimal Tuning of PID Controllers using Artificial Bee Colony Algorithm, *IEEE/ASME International Coference on Advanced Intelligent Mechatronics*, Montreal, QC, Canada, July 2010.

[22] S. Bouabdallah, *Design and Control of Quadrotors with Application to Autonomous Flying*, Ph.D. dissertation, Faculte des Sciences et Techniques, Ecole Polytechnique Federale de Lausanne, Switzerland, 2007.

[23] F. Morbidi, R. Cano, and D. Lara, Minimum-Energy Path Generation for a Quadrotor UAV, *IEEE International Coference on Robotics and Automation*, Stockholm, Sweden, May 2016.

[24] T. Kim and W. Qiao, A Hybrid Battery Model Capable of Capturing Dynamic Circuit Characteristics and Nonlinear Capacity Effects, *IEEE Transactions on Energy Conversion*, Vol. 26: 1172-1180, 2011.

[25] D. Gandolfo, A. Brandao, D. Patino and M. Molina, Dynamic Model of Lithium Polymer Battery-Load Resistor Method for Electric Parameters Identification, *Journal of the Energy Institute*, Vol. 88: 470-479, 2015.

[26] D. Karaboga and B. Basturk, Artificial Bee Colony (ABC) Optimization Algorithm for Solving Constrained Optimization Problems, *International Fuzzy Systems Association World Congress*, Cancun, Mexico, June 2007.

[27] D. Karaboga, *An Idea Based on Honey Bee Swarm for Numerical Optimization*, Technical Report TR06, Dept. Computer. Eng., Erciyes Univ., Kayseri, Turkey, 2005.

Authors' information

[1]School of Electrical Engineering and Computer Science, University of Ottawa, Ontario, Canada.

[2]Department of Electrical and Electronics Engineering, Faculty of Engineering, Lebanese International University, Bekaa, Lebanon.

[3]Arts et Métiers ParisTech (ENSAM), Campus de Châlons en Champagne.

Zeinab Hussein Keserwan received her Bachelor of Engineering degree in Electrical and Electronics Engineering and her Master 2 Research degree in Robotics and Intelligent Systems from the Lebanese University, Hadath, Lebanon in 2020. She is currently pursuing a Master of Engineering degree in Electrical and Computer Engineering with Concentration in Applied Artificial Intelligence at the University of Ottawa, Ontario, Canada. Her domains of interest mainly include control systems, robotics, and artificial intelligence.
E-mail: zkese024@uottawa.ca

Majd Saied received her Ph.D. degree from the University of Technology of Compiègne and Lebanese University in 2016. She is an Assistant Professor with the Electrical and Electronics Engineering Department, Lebanese International University. Her current research interest concerns fault tolerance studies for unmanned aerial vehicles (UAV) systems.
E-mail: majd.saied@liu.edu.lb

Clovis Francis received his Engineering degree from the Lebanese University, Faculty of Engineering in 1990, the Master degree from the University Paul Sabatier – Toulouse in 1991, the Ph.D degree from the University paris XI – France in 1994 and the Habilitation to Direct Research (HDR) in 2009. From 1995 to 2022, He was a Professor at the Lebanese University in Automatic Control, Fault Tolerant Control and system diagnosis. Since September 2022, He joined Arts et Métiers ParisTech, France.

International Review of Automatic Control (I.RE.A.CO.), Vol. 16, N. 2
ISSN 1974-6059 March 2023

A Fuzzy Logic-Based Map Matching Approach to Increase Location Accuracy. Case Study Tirana, Albania

Luis Lamani

Abstract – *Albania has recently entered a new era in the realm of map development and digitalization. The development of the road network poses an added challenge for developers of smart city applications. Recent research on map-matching algorithms for land vehicle navigation has mostly used either traditional topological analysis or a probabilistic technique. These methods do not account for positioning errors, Horizontal Dilution Of Precision (HDOP), heading increment, and other crucial factors, which render them unreliable for complex metropolitan road networks like Albania's. Consequently, it may be difficult to pinpoint the route that the car is taking. By employing a fuzzy logic-based approach, the precision of the car's location can be significantly improved. This article describes how to implement a fuzzy logic-based system to match GPS vehicle trajectory data to a digital road network in Tirana using Python.*

Keywords*: Fuzzy Logic, Python Algorithm, GPS, Map Matching, Fuzzy Inference Systems*

Nomenclature

A	Fuzzy set for input variable X
a, b, c	Constant values determined by the last square method
API	Application Programming Interface
ATTS	Advanced Transport Telematics Systems
B	Fuzzy set for input variable Y
CSV	Comma-Separated Values
f	Fuzzy rule
FIS	Fuzzy Inference System
FL	Fuzzy Logic
FLS	Fuzzy Logic System
GPS	Global Positioning System
HDOP	Horizontal Dilution Of Precision
HE	Heading Error
IMP	Initial Matching Process
JOSM	Java OpenStreetMap Editor
MF	Membership Function
MM	Map Matching
OSM	OpenStreetMap
SMP	Subsequent Map Matching Processes
VC	Variance-Covariance
w	Membership degree of fuzzy rule
$\overline{w}$	Normalized membership degree
x, y	Input values
Z	Linear function

I. Introduction

Since its beginnings, the GPS has evolved into a vital global instrument with several applications, including transportation system management, land and agricultural management, company management, and so on.

Nowadays, GPS provides navigation and timing services for civic and business purposes all around the world. This article highlights its significance for mobility technology such as personal navigation aids [1]. Various advanced transport telematics systems that rely on GPS are currently available. ATTS consists of all types of sophisticated personal navigation aid systems and vehicle monitoring and tracking systems. All types of navigation systems use GPS devices of various types, whether for positioning, moving between locations, tracking an object or personal activity, or producing various types of maps. All of these systems are comprised of two fundamental elements: a device for determining a vehicle's location (e.g., a GPS tracking device) and a digital road map for referencing the vehicle's location.

Ideally, both of these components are 100% precise, and the position of the car aligns with the digital road network. Both GPS and digital road networks include flaws, which is unfortunate. GPS is susceptible to systematic mistakes, atmospheric interference errors, calculation and rounding problems, ephemeris (orbital route) data issues, etc. [2]. Albania has entered a new era of map digitization and growth. Obtaining two satellites, Albania 1 and Albania 2, will provide a significant benefit in this aspect, inter alia. This development necessitates ongoing data compatibility enhancement in order to pinpoint an exact position, along with periodic urban changes that raise building density and network complexity. This fast expansion of the road network in developing countries, such as Albania, results in regular data and information updates. The digital road network develops flaws as a result of the creation and digitization of maps [3], [4]. Therefore, it is highly unlikely that the GPS positions and the digital road network would match,

 https://doi.org/10.15866/ireaco.v16i2.23212

and further effort, known as map matching, is required to reconcile them. The fuzzy logic map matching method is the most successful of the available map matching algorithms in terms of recognizing proper linkages in the digital road network [3]. This study's objective is to implement the fuzzy logic-based map matching method in the Python programming language. The developed approach may be used to correlate imprecise GPS-derived car positions with a digital road network. The structure of implementation has consisted of three interconnected components: IMP, SMP-1, and SMP-2.

The initial matching process determines the location of the vehicle on the link. Subsequent Map Matching Processes (SMP-1 and SMP-2) match trailing positions to the link if the vehicle has not crossed the link (SMP-1) or passed an intersection (SMP-2). In all three procedures, fuzzy inference algorithms have been utilized to evaluate the likelihood of a match while considering various variables.

The sections of this paper are organized as follows. A literature review is provided in Section II. The methodology of the data collection, fuzzy logic, and motivation for using Python to implement the proposed algorithm are provided in Section III. The proposed architecture and the algorithm implementation are presented in Section IV. The results of this case study in Tirana are presented in Section V. The last section of this paper contains the conclusions.

II. Literature Review

MM algorithms have been extensively applied in road transportation and can be categorized as topological, geometric, probabilistic, and advanced, as outlined in [5].

The initial algorithm for car navigation utilizing the MM approach has been described in [6]. This particular algorithm is geometric in nature and relies on the shape of the road segment. The algorithm's lack of accuracy, particularly at intersections and parallel roads, can be attributed to its simplistic structure. Velaga et al. [7] have identified and tackled various shortcomings present in the current topological Molecular Modeling (MM) algorithms. They have proposed an improved weight-based topological MM algorithm that has incorporated two novel weights for intersections and link connectivity.

The experimental findings indicate that the improved MM algorithm outperforms the majority of current topological MM algorithms. Greenfeld [8] has presented a methodology for processing low-quality GPS data by using a topologically based approach. The match has been determined based on a weighted score calculation, with the highest score being selected. White et al. [9] have presented a pair of straightforward geometric and topological MM algorithms for comparative purposes.

Despite the conventional nature of the proposed algorithms, the authors provide insight into potential future directions for MM algorithms. Chen and Bierlaire [10] have introduced a probabilistic approach that utilizes a measurement model for smartphones to determine the probability of the observed data in transportation networks. The output of this approach is a set of potential road segments that align with the highest probabilities, using a probabilistic approach. Quddus and Washington [11] have developed a new weight-based shortest path and vehicle trajectory-aided MM algorithm, taking into account the low-frequency positioning data. The A algorithm, a widely recognized method for searching for the shortest path, has been utilized in this study.

Furthermore, two supplementary weights have been established to account for the shortest path and vehicle trajectory. The findings of the simulation suggest that the algorithm that has been created is appropriate for the provision of transport applications and services in real-time. Sharath et al. [12] have developed a dynamic 2-D MM algorithm that incorporates dynamic weight coefficients and road width. The road segment has been represented as a matrix of grids centered on its center line. The identification of location has been determined by assigning a weight score based on factors such as proximity, kinematics, turn-intent prediction, and connectivity. Krüger et al. [13] have introduced a visual interactive algorithm for multimedia matching that encompasses both preprocessing and matching procedures. The preprocessing parameters have been optimized through the utilization of immediate visual feedback. The effectiveness of this method has been demonstrated by using a large amount of car trajectory data. The authors of [14] have proposed a closed-loop multimodal framework to facilitate ground vehicle navigation by leveraging ambient signals of opportunity.

The proposed framework is based on the premise that the vehicle has pre-existing knowledge of its initial states. The subsequent states of the vehicle are evaluated by a particle filter. Most advanced MM algorithm approaches are Fuzzy Logic (FL)-based. The introduction of FL into the domain of MM has been initially attributed to Kim and Kim [6]. A new algorithm using fuzzy logic has been introduced for identifying accurately the specific road segment where a vehicle is located. The study conducted by Fu et al. [15] has considered the possible segments that are associated with the current road segment. These segments have been identified based on projected points that are located within the radius of positioning error detected by GPS. If there are multiple candidates, each segment of the candidates is evaluated through a fuzzy system that considers the differences in both distance and heading.

Jagadeeshet et al. [16] have developed a basic fuzzy inference system in order to determine the probability of each road in the potential set based on variations in distance and heading. According to Syed and Cannon's research [17], the initial GPS conditions indicate that the first segment is highly resilient. Consequently, a Fuzzy Logic System (FLS) has been utilized to ascertain whether the present GPS point is situated within the preceding segment. The level of confidence for the MM locations has been established, albeit without any further explication. Quddus et al. [18] have enhanced the

accuracy of the FLS-based MM algorithm. The current study differs from previous FL-based MM algorithms [15]-[17], and [19] by integrating an improved GPS positioning system that combines data from vehicle sensors. Therefore, the use of additional data, such as the speed and direction of the vehicle, the heading of the vehicle, and its difference, can act as precursors for the Fuzzy Logic System (FLS).

The objective of this work is to present a Python-based algorithm that shows a notable degree of accuracy in the context of MM. The implementation of fuzzy logic systems allows for the achievement of this goal.

III. Methodology

In this article, all of the essential data is tabular, requiring a quantitative analysis approach. Both the GPS data and the digital road map should be accessible for testing.

III.1. Data Collection

Using a GPS receiver (*Trimble Juno SB*), vehicle trajectory information has been gathered. *Trimble Juno* is a multifunctional GPS device that collects geodata in many file formats. The speed of the vehicle and the intervals between loggings, both of which have played significant roles in the calculations, have been measured with *RoadLabPro*. *OpenStreetMap* is a free, editable, open-source map of the entire world that volunteers have mostly created from scratch. All the acquired data is saved in *OpenStreetMap* databases using many software applications, JOSM in particular. This API is used as the data source for the second component due to its spatial coverage and the data's legibility.

III.2. Fuzzy Logic

Fuzzy logic is based on human reasoning rather than precise mathematical modeling [20]-[25]. Typically, the dynamic nature of a fuzzy system can be defined by a collection of linguistic fuzzy rules [20]. In the 1960s, Zadeh first introduced it [26]. Through his work in control engineering, Zadeh came up with the fuzzy theory to deal with processes that needed human operator competence but were only loosely expressed in words [27]. Fuzzy logic allows many truth values to be processed through a single variable [28]. Fuzzification is a mathematical process that involves the conversion of an element within the universe of discourse into a membership value of a fuzzy set [20]. The idea of different levels of membership or membership values has been made to reflect the meaning of certain words and phrases [29]. A collection of if-then rules is used to map an input space to an output space. These rules are based on the knowledge and on the experience of a human expert in that domain. Fuzzy rules are of the general form: if > antecedent(s) then consequent(s). The antecedent and the consequent of a fuzzy rule consist of propositions that incorporate linguistic variables [20].

Figure 1 depicts the whole Fuzzy Inference System (FIS) that performs this function. The Sugeno [30], [31] Fuzzy Inference System (FIS) is a key element in the fuzzy logic-based map matching algorithm. Its primary function is to assess the probability of a GPS location being matched to a particular link within the digital road network. However, it differs slightly from the FIS mentioned above. If the fuzzy rules in the FIS are described like this, i.e. if x is A and y is B, then z is C, then the rules in Sugeno's FIS look like this: if x is A and y is B, then $Z = f(x, y)$; as a linear function, hence $Z = ax + by + c$ or a constant if $a = b = 0$. Figure 2 provides a detailed mathematical explanation of how Sugeno's FIS operates.

Fuzzy rule:

$$\begin{aligned} f_1 &= a_1 x + b_1 y + c_1 \\ f_2 &= a_2 x + b_2 y + c_2 \end{aligned} \tag{1}$$

Defuzzification:

$$f = \frac{w_1 f_2 + w_2 f_2}{w_1 + w_2} = \bar{w}_1 f_1 + \bar{w}_2 f_2 \tag{2}$$

where A is the fuzzy set for input var X, B is the fuzzy set for input var Y, x, y are input values, f is the fuzzy rule, a, b, c are constant values determined by the last square method, w is the membership degree of fuzzy rule; $\bar{w}$ is the normalized membership degree.

III.3. Python

The fact that Python will be used to implement the presented approach is already noted. Because of its widespread adoption by major GIS systems, Python has risen to prominence as the language of choice for geospatial research, but its versatility as a data-analysis tool and its understandable syntax have also attracted a growing number of users [32].

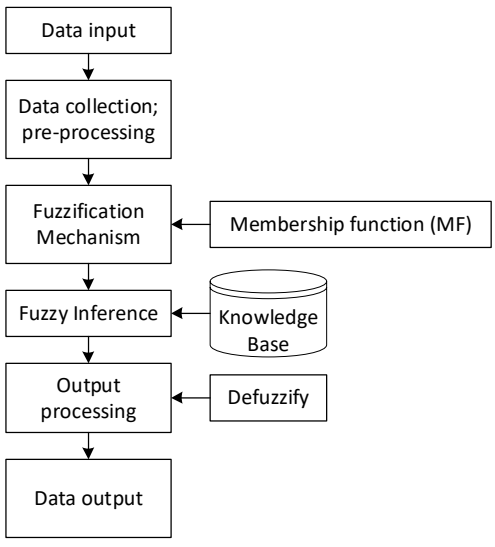

Fig. 1. Fuzzy Inference System

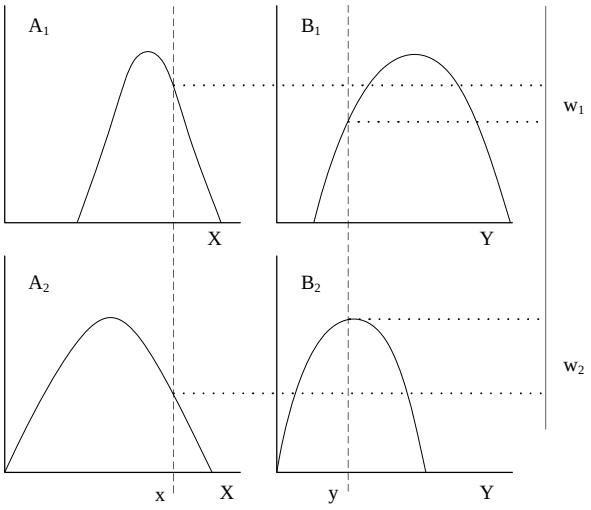

Fig. 2. Sugeno's Fuzzy Inference System

In addition, several tools have been designed from the beginning as open source, and their accessibility is steadily attracting more users. Several widely accessible modules and libraries can be quickly loaded and imported, allowing developers to create sophisticated applications with relatively few lines of code. The filtering and processing of data is a crucial starting step in this study, and Python makes it much simpler [32].

IV. The Algorithm's Implementation and Architecture

IV.1. The Structure of the Fuzzy Map Matching Algorithm

The fuzzy logic map-matching method divides the map-matching process into two parts. The Initial Map Matching Process (IMP) and the Subsequent Map Matching Process (SMP) are responsible for identifying the proper connection in the digital road network, which is the most challenging part. The second part involves determining the position of a vehicle on a connection [3].

The algorithm's structure is depicted in Figure 3. The Initial Map Matching Process (IMP) is the first and most crucial step in the map matching process since it identifies the initial link. The presence of an error in this context is likely to result in subsequent inconsistencies.

The methodology entails the correlation of an error zone, which may be elliptical or rectangular in shape, encompassing the GPS location with the existing road infrastructure. The error region is determined by utilizing the variance-covariance matrix that is linked to the GPS location error. The trajectory data that has been gathered does not possess the requisite information for the computation of the VC matrix. This includes parameters such as the topocentric distance between the satellite and the receiver as well as the range between the two entities.

The initial map matching process uses a fuzzy system to determine which link is suitable between candidate links after the formation of the error rectangle.

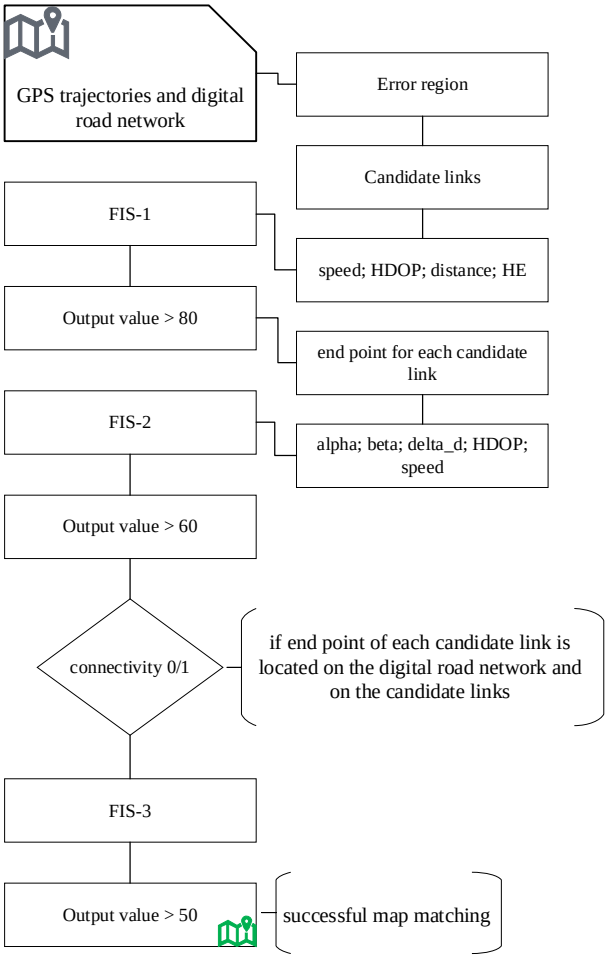

Fig. 3. Algorithm architecture for fuzzy logic map matching

The input variables of this fuzzy inference system are the vehicle's speed, *v* (m/s), the Horizontal Dilution Of Precision (HDOP), the distance to the link, and the heading error, HE (degrees), which is the absolute difference between the vehicle's direction and the link's.

The output represents the probability of matching a location fix to a candidate link. The subsequent map matching process starts after the initial map matching process has been successfully completed and is responsible for matching the subsequent positions. It is divided into two sections:

- The Subsequent Map Matching Process (SMP-1) checks if the vehicle has already crossed a junction or is likely to do so, and if not, matches subsequent positions to the connection provided by the IMP;
- If the vehicle has crossed a junction, the Subsequent Map Matching Process at the junction (SMP-2) selects a new connection among the candidate links.

IV.2. Data Acquisition and Processing

The input to the fuzzy logic map matching algorithm is a geodata frame, which is derived from trajectory data through many conversions. It contains the coordinates of the GPS track that should be matched with the digital

road network. In addition, it should include the following data for processing by the algorithm:

- GPS.Speed in km/h;
- GPS.Bearing;
- GPS.HDOP;
- HE;
- Time.

Missing values in the data are replaced with zeros since they might lead to improper matchings between the corresponding and succeeding points. In order to get started with the implementation of the algorithm, it is necessary to gather and store the digital road network (OSM) data, which can be conveniently accessed in Python through modules like osmnx and network.

Additional data increases the algorithm's latency. Hence, it is crucial to filter and validate the input.

IV.3. The implementation of the Initial Map Matching Process

As mentioned previously, the initial procedure for map matching involves constructing an error zone for each GPS trajectory point. Therefore, a fixed-length error rectangle should be generated at each point on the trajectory.

More modules should be imported to accomplish this. One of these modules is shapely, which is used for Python analysis of two-dimensional geometry. Following that, various FIS-1 variables are computed.

Calculating the distance between each GPS trajectory point and the highways (links) should come first, followed by determining the error in direction, which is the difference between each GPS trajectory point's azimuth and direction. The heading error is calculated as the difference between the directions (azimuth) of the links and the azimuth values for every point on the trajectory. The HDOP and velocity parameters are calculated by using the trajectory data. Then the data frame is saved as a CSV file and used as an input to FIS-1.

The Python code for fuzzy inference systems is nearly the same. The modules *pyFUME* and *simpful* are required for its implementation [33], [34]. The most essential aspect of this work is the development of fuzzy inference systems. The value obtained as a result of this calculation reflects, with regard to each FIS, the probability that these linkages are accurate. In addition to that, these modules provide membership function graphs, which are shown in Figure 4.

IV.4. The implementation of the Subsequent Map Matching Process

The starting point is the implementation of Subsequent Map Matching Process-1 in Python, which aims to determine the potential of matching future positions with existing links. The following FIS-2 variables are calculated after getting two positions from the GPS trajectories: a position known as the "last defined position" and a position called the "current position":

- Speed: calculated from trajectory data;
- Alpha: last fixed location, relative to the connection, as seen from the last current position [33];
- Beta: the location of the current fixed position relative to the connection as seen from the next junction;
- Delta_d: the difference between the distance between the last fixed position and the last point of each path and the distance the vehicle has travelled since the last fixed position;
- HI: calculated as the difference between azimuth values for consecutive points;

All data are saved in a *csv* file, just like in IMP, and then entered into FIS-2.

If a vehicle has passed through an intersection, SMP-2 will now determine new connections for candidate connections.

This step makes extensive use of the variables and data tables defined in the two preceding processes. Link connections are an additional variable that this Fuzzy Inference System (FIS) should consider.

The link association is established by generating a binary column in the data table, which consists of zeros and ones, in order to indicate the direct correlation between a potential link and a previously selected link.

As per the definition outlined in SMP-1, the numerical value of 1 indicates the connection of the candidate link with the preceding link.

On the other hand, 0 indicates that this association is not true. It starts with the points on the routes of the digital road network.

Then, for every point in this data series that corresponds to a potential connection point in the FIS-3 data series, a value of 1 is assigned. By using FIS-3 in the same manner as before, the data is stored and processed to obtain the result value (Fig. 5).

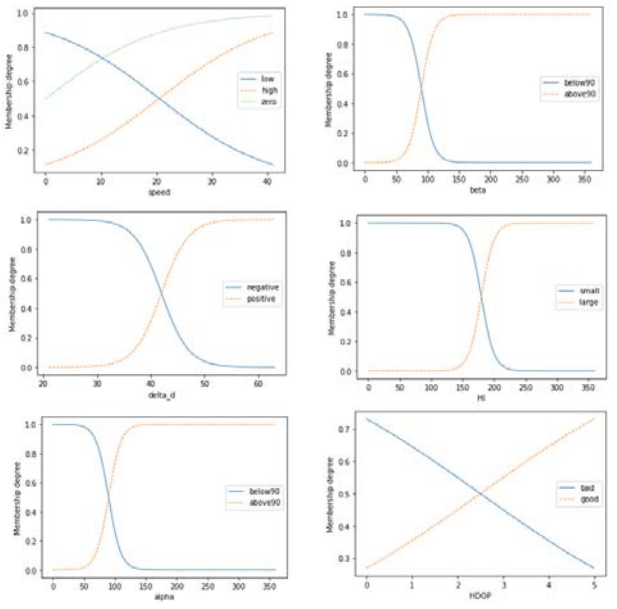

Fig. 4. Membership function graphs FIS-2

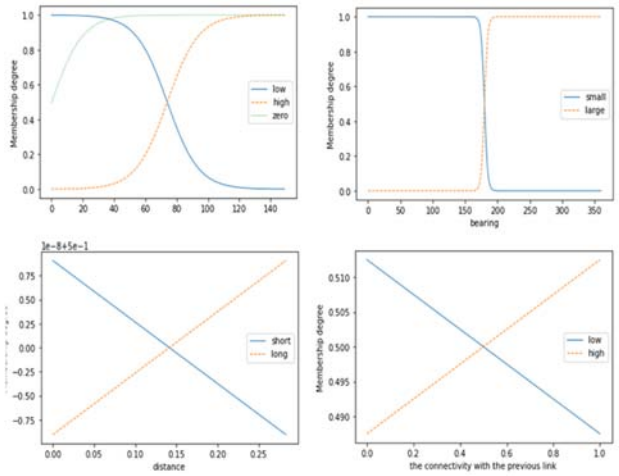

Fig. 5. Membership function graphs FIS-3

V. Result

The lack of relevant data related to the vehicle's location in user-generated trajectories poses a challenge in determining the adequacy of the established connections. The algorithm proposed in this paper aims to identify apparent inconsistencies and determine the conditions under which they arise. In order to assess the algorithm's performance across distinct geographic regions, namely rural and urban areas, varying ranges of values have been obtained and displayed from the data tables. As seen in Figure 6, the algorithm performs exceptionally well in rural areas (where green points represent trajectory positions and red points represent matching spots). In rural locations, the road density is low and GPS placements are more exact, making map matching easier and more precise. As demonstrated, the dislocation of trajectory locations occurs predominantly in turns, and the algorithm is able to match accurately those locations. In urban areas (Figure 7), the identification of the link is also effective. Even if the road density is significantly higher than in rural areas and GPS sites are sometimes fairly distant from the roads, the algorithm is able to detect accurately the linkages.

However, in this case, there is an issue with the determination of the vehicle's location with regard to the object. Although the algorithm can identify the correct connection, if the GPS position is ahead of the link, the link location frequently becomes the final link node. The majority of mismatches occur on multi-lane roadways where the matched location is in the incorrect lane. The lack of values in the digital road network table or the lack of values in the trajectory data might also result in mismatches. As a result, the findings indicate that: (1) the Python-based algorithm is highly efficient in accurately identifying the appropriate links; (2) using an area of fixed dimensions to create an "error zone" might not be the most optimal approach; however, it has no impact on the accurate identification of the specific points that the vehicle navigates; and (3) the removing or labeling (flagging) of trajectories lacking essential data in order to increase the performance. Subsequent to these results, the forthcoming work will consist of improving the Python algorithm by testing additional metropolitan regions.

This case study will also build a repository of taken-in trajectories to improve satellite-based digital mapping.

VI. Conclusion

The study outlines the deployment of a fuzzy logic-driven system to align GPS vehicle trajectory data with a digital road network in Tirana using the Python programming language. This approach has been chosen due to its proven efficacy in detecting connections.

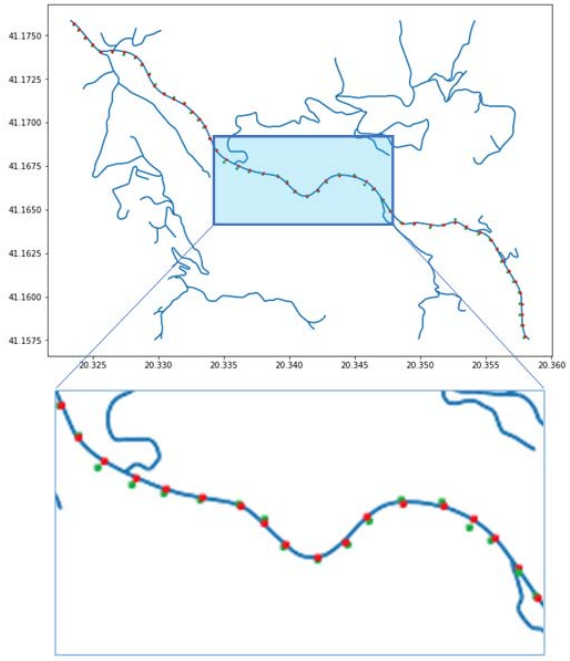

Fig. 6. Map matching in rural areas (Tirana); green points represent trajectory positions and red points represent matching spots

Fig. 7. Map matching in urban areas (map of Tirana - “Blloku” square); green points represent trajectory positions and red points represent matching spots

Due to insufficient data in the GPS trajectories, the VC matrix could not be generated, rendering its collection unattainable. Therefore, modifications have been made to various components of the algorithm, which have included the creation of an error location.

The error zone is defined with a fixed scale, and the location of the vehicle for the given link is determined by computing the nearest point along the link. Although not an optimal solution, it does not affect the primary function of the algorithm, which is to detect the pathways on which the vehicle is navigating. The outcome allows for the alignment of GPS-derived trajectories with a digital road network. It is essential to acknowledge that although the recently developed algorithm is functional, there are certain concerns that need to be considered.

Based on each iteration of the algorithm, it is necessary to retrieve and analyze the data in order to generate a digital representation of the road network. Depending on the size and characteristics of the region, this might increase latency. In terms of performance, a digital road network can exhibit superior outcomes when pre-existing knowledge of the location is available. In order to enhance further performance, it is possible to identify an alternative source for getting route data, such as an API that would allow queries, particularly if this source provides better data filtering. The outcome of this work includes both documentation and a functional code that enables users to align their GPS trajectories with a digital road network. Obtaining or producing an additional data repository for the digital road network could improve the algorithm's performance. This depends on the assumption that the data is downloaded and processed for each iteration, which may necessitate a substantial amount of time. Managing data from a large area or a highly interconnected transportation network can present significant difficulties. As the understanding of a specific region increases, its perceived size tends to decrease. Furthermore, the algorithm performs better when additional filters are applied to the provided data.

This will be done as part of ongoing work to improve the algorithm.

Appendix

FIS-1

```
from simpful import *
FS=FuzzySystem()
#the fuzzy rules
RULE1='IF (speed IS high) AND (bearing IS small) THEN (L1 IS average)'
RULE2='IF (speed IS high) AND (bearing IS large) THEN (L1 IS low)'
RULE3='IF (HDOP IS good) AND (distance IS short) THEN (L1 IS average)'
RULE4='IF (HDOP IS good) AND (distance IS long) THEN (L1 IS average)'
RULE5='IF (bearing IS small) AND (distance IS short) THEN (L1 IS high)'
RULE6='IF (bearing IS large) AND (distance IS long) THEN (L1 IS low)'
FS.add_rules([RULE1,RULE2,RULE3,RULE4,RULE5,RULE6])
#output values
FS.set_crisp_output_value('low',10)
FS.set_crisp_output_value('average',50)
FS.set_crisp_output_value('high',100)
#fuzzy sets for each input variable
#the fuzzy sets for the input variable speed
FS_1=FuzzySet(function=InvSigmoid_MF(c=74, a=0.1), term="low")
FS_2=FuzzySet(function=Sigmoid_MF(c=74, a=0.1), term="high")
FS_3=FuzzySet(function=Sigmoid_MF(c=74, a=0.1), term="zero")
MF_speed = LinguisticVariable([FS_1,FS_2,FS_3], concept="speed", universe_of_discourse=[0,149])
FS.add_linguistic_variable("speed", MF_speed)
#the fuzzy sets for the input variable bearing
FS_4=FuzzySet(function=InvSigmoid_MF(c=180, a=0.4), term="small")
FS_5=FuzzySet(function=Sigmoid_MF(c=180, a=0.4), term="large")
MF_bearing = LinguisticVariable([FS_4,FS_5], concept="bearing", universe_of_discourse=[0,360])
FS.add_linguistic_variable("bearing", MF_bearing)
#the fuzzy sets for the input variable distance
FS_6=FuzzySet(function=InvSigmoid_MF(c=0.141563, a=0.000000256), term="short")
FS_7=FuzzySet(function=Sigmoid_MF(c=0.141563, a=0.000000256), term="long")
MF_distance = LinguisticVariable([FS_6,FS_7], concept="distance", universe_of_discourse=[0,0.283126])
FS.add_linguistic_variable("distance", MF_distance)
#the fuzzy sets for the input variable HDOP
FS_8=FuzzySet(function=InvSigmoid_MF(c=2.5, a=0.4), term="bad")
FS_9=FuzzySet(function=Sigmoid_MF(c=2.5, a=0.4), term="good")
MF_HDOP = LinguisticVariable([FS_8,FS_9], concept="HDOP", universe_of_discourse=[0,5])
FS.add_linguistic_variable("HDOP", MF_HDOP)
# Plot all linguistic variable
FS.plot_variable('speed')
FS.plot_variable('bearing')
FS.plot_variable('HDOP')
FS.plot_variable('distance')
from pyfume import *
# Set the path to the data and choose the number of clusters (automatically two if not chosen)
path='./fis1_data.csv'
# Generate the Takagi-Sugeno FIS
FIS = pyFUME(datapath=path)
# Extract the model from the FIS object
model1=FIS.get_model()
# Perform inference and print predicted value
```

```
print(model1.Sugeno_inference(['L1']))
```

FIS-2

```
#in order to import packages run 'pip install 'name of package" on the terminal
from simpful import *
FS=FuzzySystem()
#the fuzzy rules
RULE1='IF (alpha IS below90) AND (beta IS below90) THEN (L2 IS high)'
RULE2='IF (delta_d IS positive) AND (alpha IS above90) THEN (L2 IS low)'
RULE3='IF (delta_d IS positive) AND (beta IS above90) THEN (L2 IS low)'
RULE4='IF (HI IS small) AND (alpha IS below90) AND (beta IS below90) THEN (L2 IS high)'
RULE5='IF (HI IS small) AND (delta_d IS positive) AND (alpha IS above90) THEN (L2 IS low)'
RULE6='IF (HI IS small) AND (delta_d IS positive) AND (beta IS above90) THEN (L2 IS low)'
RULE7='IF (HI IS large) AND (alpha IS below90) AND (beta IS below90) THEN (L2 IS low)'
RULE8='IF (HDOP IS good) AND (speed IS zero) THEN (L2 IS high)'
RULE9='IF (HDOP IS good) AND (delta_d IS negative) THEN (L2 IS average)'
RULE10='IF (HDOP IS good) AND (delta_d IS positive) THEN (L2 IS low)'
RULE11='IF (speed IS high) AND (HI IS small) THEN (L2 IS average)'
RULE12='IF (HDOP IS good) AND (speed IS high) AND (HI IS 180) THEN (L2 IS high)'
FS.add_rules([RULE1,RULE2,RULE3,RULE4,RULE5,RULE6,RULE7,RULE8,RULE9,RULE10,RULE11,RULE12])

#output values
FS.set_crisp_output_value('low',10)
FS.set_crisp_output_value('average',50)
FS.set_crisp_output_value('high',100)
#fuzzy sets for each input variable
#the fuzzy sets for the input variable speed
FS_1=FuzzySet(function=InvSigmoid_MF(c=20.5, a=0.1), term="low")
FS_2=FuzzySet(function=Sigmoid_MF(c=20.5, a=0.1), term="high")
FS_3=FuzzySet(function=Sigmoid_MF(c=0.1, a=0.1), term="zero")
MF_speed = LinguisticVariable([FS_1,FS_2,FS_3], concept="speed", universe_of_discourse=[0,41])
FS.add_linguistic_variable("speed", MF_speed)
#the fuzzy sets for the input variable delta_d
FS_4=FuzzySet(function=InvSigmoid_MF(c=42, a=0.4), term="negative")
FS_5=FuzzySet(function=Sigmoid_MF(c=42, a=0.4), term="positive")
MF_delta_d = LinguisticVariable([FS_4,FS_5], concept="delta_d", universe_of_discourse=[21,63])
FS.add_linguistic_variable("delta_d", MF_delta_d)
#the fuzzy sets for the input variable alpha
FS_6=FuzzySet(function=InvSigmoid_MF(c=90, a=0.1), term="below90")
FS_7=FuzzySet(function=Sigmoid_MF(c=90, a=0.1), term="above90")
MF_alpha = LinguisticVariable([FS_6,FS_7], concept="alpha", universe_of_discourse=[0,360])
FS.add_linguistic_variable("alpha", MF_alpha)
#the fuzzy sets for the input variable beta
FS_8=FuzzySet(function=InvSigmoid_MF(c=90, a=0.1), term="below90")
FS_9=FuzzySet(function=Sigmoid_MF(c=90, a=0.1), term="above90")
MF_beta = LinguisticVariable([FS_8,FS_9], concept="beta", universe_of_discourse=[0,360])
FS.add_linguistic_variable("beta", MF_beta)
#the fuzzy sets for the input variable HI
FS_10=FuzzySet(function=InvSigmoid_MF(c=180, a=0.1), term="small")
FS_11=FuzzySet(function=Sigmoid_MF(c=180, a=0.1), term="large")
MF_HI = LinguisticVariable([FS_10,FS_11], concept="HI", universe_of_discourse=[0,360])
FS.add_linguistic_variable("HI", MF_HI)
#the fuzzy sets for the input variable HDOP
FS_12=FuzzySet(function=InvSigmoid_MF(c=2.5, a=0.4), term="bad")
FS_13=FuzzySet(function=Sigmoid_MF(c=2.5, a=0.4), term="good")
MF_HDOP = LinguisticVariable([FS_12,FS_13], concept="HDOP", universe_of_discourse=[0,5])
FS.add_linguistic_variable("HDOP", MF_HDOP)
# Plot all linguistic variables
FS.plot_variable('speed')
FS.plot_variable('delta_d')
FS.plot_variable('alpha')
FS.plot_variable('beta')
FS.plot_variable('HI')
FS.plot_variable('HDOP')
from pyfume import *
# Set the path to the data and choose the number of clusters (automatically two if not chosen)
path='./fis2_data.csv'
# Generate the Takagi-Sugeno FIS
FIS = pyFUME(datapath=path)
# Extract the model from the FIS object
model2=FIS.get_model()
# Perform inference and print predicted value
print(model2.Sugeno_inference(['L2']))
```

FIS-3

```
from simpful import *
```

```
FS=FuzzySystem()
#fuzzy rules
#the fuzzy rules
RULE1='IF (speed IS high) AND (bearing IS small) THEN (L3 IS average)'
RULE2='IF (speed IS high) AND (bearing IS large) THEN (L3 IS low)'
RULE3='IF (HDOP IS good) AND (distance IS short) THEN (L3 IS average)'
RULE4='IF (HDOP IS good) AND (distance IS long) THEN (L3 IS average)'
RULE5='IF (bearing IS small) AND (distance IS short) THEN (L3 is high)'
RULE6='IF (bearing IS large) AND (distance IS long) THEN (L3 IS low)'
RULE7='IF (connectivity IS low) THEN (L3 IS low)'
RULE8='IF (connectivity IS high) THEN (L3 IS high)'
FS.add_rules([RULE1,RULE2,RULE3,RULE4,RULE5,RULE6,RULE7,RULE8])
#output values
FS.set_crisp_output_value('low',10)
FS.set_crisp_output_value('average',50)
FS.set_crisp_output_value('high',100)
#fuzzy sets for each input variable
#the fuzzy sets for the input variable speed
FS_1=FuzzySet(function=InvSigmoid_MF(c=74, a=0.1), term="low")
FS_2=FuzzySet(function=Sigmoid_MF(c=74, a=0.1), term="high")
FS_3=FuzzySet(function=Sigmoid_MF(c=74, a=0.1), term="zero")
MF_speed = LinguisticVariable([FS_1,FS_2,FS_3], concept="speed", universe_of_discourse=[0,149])
FS.add_linguistic_variable("speed", MF_speed)
#the fuzzy sets for the input variable bearing
FS_4=FuzzySet(function=InvSigmoid_MF(c=180, a=0.4), term="small")
FS_5=FuzzySet(function=Sigmoid_MF(c=180, a=0.4), term="large")
MF_bearing = LinguisticVariable([FS_4,FS_5], concept="bearing", universe_of_discourse=[0,360])
FS.add_linguistic_variable("bearing", MF_bearing)
#the fuzzy sets for the input variable distance
FS_6=FuzzySet(function=InvSigmoid_MF(c=0.141563, a=0.000000256), term="short")
FS_7=FuzzySet(function=Sigmoid_MF(c=0.141563, a=0.000000256), term="long")
MF_distance = LinguisticVariable([FS_6,FS_7], concept="distance", universe_of_discourse=[0,0.283126])
FS.add_linguistic_variable("distance", MF_distance)
#the fuzzy sets for the input variable HDOP
FS_8=FuzzySet(function=InvSigmoid_MF(c=2.5, a=0.4), term="bad")
FS_9=FuzzySet(function=Sigmoid_MF(c=2.5, a=0.4), term="good")
MF_HDOP = LinguisticVariable([FS_8,FS_9], concept="HDOP", universe_of_discourse=[0,5])
FS.add_linguistic_variable("HDOP", MF_HDOP)
#the fuzzy sets for the input variable connectivity
FS_10=FuzzySet(function=InvSigmoid_MF(c=1
,a=0), term="low")
FS_11=FuzzySet(function=Sigmoid_MF(c=1,a=0), term="high")
MF_connectivity = LinguisticVariable([FS_10,FS_11], concept="the connectivity with the previous link", universe_of_discourse=[0,1])
FS.add_linguistic_variable("connectivity", MF_connectivity)
# Plot linguistic variables
FS.plot_variable('speed')
FS.plot_variable('bearing')
FS.plot_variable('HDOP')
FS.plot_variable('distance')
FS.plot_variable('connectivity')
from pyfume import *
# Set the path to the data and choose the number of clusters (automatically two if not chosen)
path='./fis3_data.csv'
# Generate the Takagi-Sugeno FIS
FIS = pyFUME(datapath=path)
# Extract the model from the FIS object
model3=FIS.get_model()
# Perform inference and print predicted value
print(model3.Sugeno_inference(['L3']))
```

References

[1] Christopher E White, David Bernstein, Alain L Kornhauser, Some map matching algorithms for personal navigation assistants, *Transportation Research Part C: Emerging Technologies*, Vol. 8, (Issues 1 – 6), pp. 91-108, 2000.

[2] P. Ranacher and R. Brunauer and W. Trutschnig, S. Van der Spek, S. Reich, Why GPS makes distances bigger than they are, *International Journal of Geographical Information Science*, Vol 30, N. 2 pp. 316-333, 2016.

[3] Mohammed A. Quddus, *High Integrity Map Matching Algorithms for Advanced Transport Telematics Applications*, Ph.D. dissertation, Centre for Transport Studies Department of Civil and Environmental Engineering Imperial College, London, United Kingdom, January 2006.

[4] Mohammed A. Quddus, Ochieng, Washington Y., Zhao, L., & Noland, Robert B. A general map matching algorithm for transport telematics applications, *GPS Solutions*, Vol. 7 (3), 157–167, 2003.

[5] M. A. Quddus, W. Y. Ochieng, and R. B. Noland, Current map-matching algorithms for transport applications: State-of-the art and future research directions, *Transportation Research Part C: Emerging Technologies*, vol. 15, no. 5, pp. 312–328, 2007.

[6] J. S. Kim, J. H. Lee, T. H. Kang, W. Y. Lee, and Y. G. Kim, Node based map matching algorithm for car navigation system, *International Symposium on Automotive Technology & Automation*, 1996.

[7] N. R. Velaga, M. A. Quddus, and A. L. Bristow, *Developing an enhanced weight-based topological map-matching algorithm for intel- ligent transport systems*, Transportation Research Part C: Emerging Technologies, vol. 17, no. 6, pp. 672–683, 2009.

[8] J. S. Greenfeld, Matching GPS observations to locations on a digital map, *81th Annual Meeting of the Transportation Research Board*, vol. 1, no. 3, 2002, pp. 164–173.

[9] C. E. White, D. Bernstein, and A. L. Kornhauser, Some map matching algorithms for personal navigation assistants, *Transportation Research Part C: Emerging Technologies*, vol. 8,

no. 1-6, pp. 91–108, 2000.
[10] J. Chen and M. Bierlaire, Probabilistic multimodal map matching with rich smartphone data, *Journal of Intelligent Transportation Systems*, vol. 19, no. 2, pp. 134–148, 2015.
[11] M. Quddus and S. Washington, Shortest path and vehicle trajectory aided map-matching for low frequency GPS data, *Transportation Re- search Part C: Emerging Technologies*, vol. 55, pp. 328–339, 2015.
[12] M.N. Sharath, Nagendra R. Velaga, Mohammed A. Quddus, A dynamic two-dimensional (D2D) weight-based map-matching algorithm, *Transportation Research Part C: Emerging Technologies*, Volume 98, 2019, Pages 409-432, ISSN 0968-090X.
[13] R. Krüger, G. Simeonov, F. Beck, and T. Ertl, Visual interactive map matching, *IEEE Transactions on Visualization and Computer Graphics*, vol. 24, no. 6, pp. 1881–1892, 2018.
[14] M. Maaref and Z. M. Kassas, A closed-loop map-matching approach for ground vehicle navigation in GNNS-denied environments using signals of opportunity, *IEEE Transactions on Intelligent Transportation Systems*, 2019.
[15] M. Fu, J. Li, and M. Wang, A hybrid map matching algorithm based on fuzzy comprehensive judgment, in Proceedings, *7th International IEEE Conference on Intelligent Transportation Systems IEEE*, 2004, pp. 613–617.
[16] G. Jagadeesh, T. Srikanthan, and X. Zhang, A map matching method for GPS based real-time vehicle location, *The Journal of Navigation*, vol. 57, no. 3, pp. 429–440, 2004.
[17] S. Syed and M. E. Cannon, "Fuzzy logic-based map matching algorithm for vehicle navigation system in urban canyons," in *ION National Technical Meeting*, no. 1, 2004, pp. 26–28.
[18] M. A. Quddus, R. B. Noland, and W. Y. Ochieng, A high accuracy fuzzy logic-based map matching algorithm for road transport, *Journal of Intelligent Transportation Systems*, vol. 10, no. 3, pp. 103–115, 2006.
[19] S. Kim and J.-H. Kim, Adaptive fuzzy-network-based C-measure map- matching algorithm for car navigation system, *IEEE Transactions on Industrial Electronics*, vol. 48, no. 2, pp. 432–441, 2001.
[20] Ignatyev, V., Kovalev, A., Spiridonov, O., Kureychik, V., Soloviev, V., Ignatyeva, A., A Method of Optimizing the Rule Base in the Sugeno Fuzzy Inference System Using Fuzzy Cluster Analysis, (2020) *International Review of Electrical Engineering (IREE)*, 15 (4), pp. 316-327. doi:https://doi.org/10.15866/iree.v15i4.16545
[21] El Farnane, A., Youssefi, M., Mouhsen, A., Kachmar, M., Oumouh, A., El Aissaoui, A., Trajectory Tracking of Autonomous Driving Tricycle Robot with Fuzzy Control, (2022) *International Review of Automatic Control (IREACO)*, 15 (2), pp. 80-86. doi: https://doi.org/10.15866/ireaco.v15i2.21719
[22] Ngaleu, G., Tamtsia, A., Kom, C., Design and Robust Analysis of Internal Model Controllers for an Automatic Voltage Regulation System, (2020) *International Review of Electrical Engineering (IREE)*, 15 (6), pp. 474-483. doi: https://doi.org/10.15866/iree.v15i6.18191
[23] Mora, E., Ordóñez Bueno, M., Gómez, C., Structural Vulnerability Assessment Procedure for Large Areas Using Machine Learning and Fuzzy Logic, (2021) *International Review of Civil Engineering (IRECE)*, 12 (6), pp. 358-370. doi: https://doi.org/10.15866/irece.v12i6.19265
[24] Housny, H., Chater, E., El Fadil, H., Observer-Based Enhanced ANFIS Control for a Quadrotor UAV, (2021) *International Review on Modelling and Simulations (IREMOS)*, 14 (1), pp. 55-69. doi:https://doi.org/10.15866/iremos.v14i1.18991
[25] Boada Medina, M., Prieto, K., Mesa, F., Aristizabal, A., Design and Analysis of Renewable Energy Microgrids for Operations in Different Latitudes by Applying Fuzzy Logic Modeling, (2022) *International Journal on Engineering Applications (IREA)*, 10 (1), pp. 1-14. doi: https://doi.org/10.15866/irea.v10i1.20386
[26] Zadeh, Lotfi A., Fuzzy Sets, *Information and Control, 8*, (3): 338–353, 1965.
[27] E. Trillas, Lotfi A. Zadeh: On the man and his work, *Scientia Iranica*, Volume 18, Issue 3, (pp. 574-579), 2011.
[28] Cintula, Petr, Christian G. Fermüller, and Carles Noguera, *Fuzzy Logic*, The Stanford Encyclopedia of Philosophy, Metaphysics Research Lab, Stanford University, 2021.
[29] Mohammed A. Quddus, *High Integrity Map Matching Algorithms for Advanced Transport Telematics Applications* (p. 143) Ph.D. dissertation, Centre for Transport Studies Department of Civil and Environmental Engineering Imperial College, London, United Kingdom, January 2006.
[30] T. Takagi and M. Sugeno, Fuzzy identification of systems and its applications to modeling and control, *IEEE Transactions on Systems, Man, and Cybernetics*, vol. SMC-15, no. 1, pp. 116-132, 1985.
[31] M. Sugeno, G.T Kang, Structure identification of fuzzy model, *Fuzzy Sets and Systems*, Volume 28, Issue 1, pp. 15-33, 1988.
[32] Joel Lawhead, *Learning Geospatial Analysis with Python, third edition* (Packt Publishing, 2019).
[33] C. Fuchs, S. Spolaor, M. S. Nobile and U. Kaymak, pyFUME: a Python Package for Fuzzy Model Estimation, *IEEE International Conference on Fuzzy Systems (FUZZ-IEEE)*, pp. 1-8, Glasgow, UK, 2020.
[34] Spolaor S., Fuchs C., Cazzaniga P., Kaymak U., Besozzi D., Nobile M. S., Simpful: a user-friendly Python library for fuzzy logic, *International Journal of Computational Intelligence Systems*, 13 (1):1687 - 1698, 2020.
[35] Joel Lawhead, *Learning Geospatial Analysis with Python, third edition* (Packt Publishing, 2019, p. 195).

Authors' information

Polytechnic University of Tirana, Department of Geoinformatics, Albania.

Dr. Ing. **Luis Lamani** is a Lecturer at the Polytechnic University of Tirana since 2012. Web development, technical analysis of financial markets, and artificial intelligence are among his areas of interest. He completed the Doctoral degree in the field of Information System at University of Tirana, Faculty of Economics. Earlier, he completed the Bachelor and Master of Science degree in the field of Informatics Engineering. Previously, Dr. Ing. Lamani worked in the Business Relay and Innovation Centre (BRIC) within Albanian Investment and Development Agency and in the banking sector within Raiffeisen Bank in Albania, covering the strategy of business innovation and the information technology systems. He is author of several articles and books.

Praise Worthy Prize

International Review of Automatic Control (I.RE.A.CO.), Vol. 16, N. 2
ISSN 1974-6059 *March 2023*

Robust Adaptive Fuzzy Backstepping Control for 2-DOF Laboratory Helicopter System with Improved Tracking Performance

B. Ladjal[1], F. Berrabah[2], S. Zeghlache[3], A. Djerioui[1], A. Kessal[4], M. Defdaf[2], M. F. Benkhoris[5]

Abstract – *In this paper, a Robust Adaptive Fuzzy Backstepping Control (RAFBC) is applied to electromechanical system which called Twin Rotor Multi Input Multi Output System (TRMS) in order to follow the desired trajectory. This strategy yields robustness to various kinds of uncertainties and guaranteed stability of the closed-loop control system. The adaptive laws have been used in order to ameliorate the robustness against uncertainties, wind effects and external disturbances. The stability of system in the closed-loop has been demonstrated using Lyapunov method. In the control design, type 2 fuzzy logic systems are used to approximate the unknown functions. Hybrid adaptive robust tracking control schemes that are based upon a combination of bounds of type 2 fuzzy approximation parameters and the backstepping design are developed such that all the states and signals are bounded and the proposed approach alleviate the online computation burden and improves the robustness to dynamic uncertainties and external disturbances. In addition, the coupling effects between the horizontal and vertical subsystems of TRMS are considered as uncertainties. Thus, precise trajectory tracking is maintained under various operational conditions with the presence of various types of uncertainties. Unlike other controllers, the proposed control algorithm can estimate model uncertainties online and improve the robustness of the system. Experimental tests were carried out and the results demonstrate that the proposed algorithm performs well in tracking and under model uncertainties.*

Keywords: *TRMS, Robust Control, Adaptive Control, Fuzzy, Backstepping, Uncertainties, Wind Effects*

Nomenclature

a_1	Fixed constant for M1
a_2	Fixed constant1 for M1
b_1	Fixed constant for M2
b_2	Fixed constant2 for M2
$B_{1\psi}$	Friction momentum
$B_{1\varphi}$	Friction momentum
e_{ih}	Horizontal tracking error
e_{iv}	Vertical tracking error
I_1	Inertia of motor1
I_2	Inertia of motor2
K_c	Reaction momentum gain
K_{gy}	Gyroscopic momentum
K_{gx}	Gyroscopic momentum
K_{11}	Gain motor1
K_{22}	Gain motor2
M_1	Nonlinearity caused by rotor
M_{Fg}	Gravity momentum
T_{11}	Denominator motor1
T_{10}	Numerator motor1
T_{20}	Denominator motor1
T_{22}	Numerator motor2
T_0	Reaction momentum
T_p	Reaction momentum
w_{ih}	Horizontal wind effect
w_{iv}	Vertical wind effect
x	State vector
α_{ih}	Horizontal virtual control signal
α_{iv}	Vertical virtual control signal
λ_{ih}, λ_{iv}	Lyapunov parameters
$\Theta(X)$	Vector of fuzzy basis functions

I. Introduction

Recent developments of a large range of rotary-wing aerial vehicles and their vertical take-off and landing capability have stimulated many innovative applications.

Drones need a powerful control device to control position and location, as they are exposed to uncertain disturbances such as wind gales. Laboratory platforms are used to simulate complex drone trial and test new control strategies [1]. The Twin Rotor System (TRMS) is a Multi-Input and Multi-Output laboratory workbench (MIMO) whose dynamics are similar to the dynamics of the helicopter. TRMS is often used as a standard for the development of drone flight controllers. The TRMS consists of two custom rotors and two mortars of different sizes at the end of the package. These rotors are powered by separate permanent magnet DC motors. The package on a fixed vertical column is supported by a

 https://doi.org/10.15866/ireaco.v16i2.23442

hinge so that it has two separate degrees of freedom (yaw and pitch). Stack angle positions (yaw and pitch angles) can vary by changing the speed of rotors, i.e. aerodynamic thrust forces caused by rotor feathers. The angles of deviation and pervasiveness are measured with the help of increased encoders embedded in the axis. The TRMS system has an interface with a computer, and the controllers can be implemented in MATLAB/Simulink.

The inputs and outputs of rotors are strongly crossed. In addition, a flat flexible cable provides power for both engines, applies non-linear torque to the system and acts as an angle drop up stabilizer. Some TRMS cases are not directly measured and the system output is differently flat [2]. The aim of this paper is to modeling the dynamics of the multi-power field strongly paired in TRMS and design a powerful nonlinear controller for the system.

The dynamics of rotary-wing flying machines are particularly difficult to understand, the aerodynamic effects are numerous and the cross coupling between vertical and horizontal flight is complex, as well as being nonlinear in nature, and also force-coupled dynamics appear due to many unstable turbulence variables [3]. For the purpose of research on control strategies, Mechatronics engineers are interested in the development of nonlinear control laws for flying objects. Indeed, the nonlinear behavior of these devices such as the helicopter, implies the need to have the most reliable and robust flight controllers possible. In the literature, a variety of model-based control methods have been suggested for TRMS. Examples are fuzzy sliding controller [4], four PID controllers with gains set by a real value genetic algorithm [5], the predictive output feedback model controller with Unscented Kalman Filter (UKF) for the status estimation, the anticipation of active rejection of disturbances with input formatting, cascade control, control in sliding mode based on the disturbance observer in sliding mode, dual-border conditional integration with traditional backstepping controller [6], adaptive second-order SMC, and a radial-based neural network based on a SMC global fast dynamic terminal [7]. Several other controllers have been developed for other applications. In [8], the integral backstepping controller and the SMC were combined to make the controller robust to parameter uncertainties and reject paired and unpaired disturbances. A sliding recoil control scheme based on a non-linear disturbance observer was proposed in [9] for the knee exoskeleton. In [8], the backstepping controller was combined with the feedback linearization technique and higher order sliding modes. A robust backstepping controller with Type 2 adaptive fuzzy logic at interval was proposed in [10].

In this work, the presented study is in the framework of the nonlinear control called Robust Adaptive Fuzzy-Backstepping Control (RAFBC), based on the theory of fuzzy logic. In our case, these control strategies are applied experimentally on the TRMS model, which is a prototype of a helicopter characterized by its nature of non-linearity, multi-variable, strongly coupled and under actuated [2]. TRMS like other nonlinear systems presents a difficulty in obtaining an efficient controller and the problematic of following a desired trajectory. Recently, a lot of research on TRMS has been recorded in order to develop a robust controller, some of them in the context of the practical results discussing and comparing them to our work will be cited; for example: in [11], a Fuzzy Logic control technique used to control the TRMS, this technique has been widely used for nonlinear systems when the mathematical model is unknown and the available inference rules are provided by human experts. Fuzzy logic was mixed with other control methods in order to execute good tracking of the TRMS trajectory; for example, the author of [12] has developed a Neuro-Fuzzy method to transact with coupling problems, unfortunately, the methodology for determining fuzzy parameters (type of membership functions and number of bases) was absent and the results obtained were only simulated. The author in [13] used the combination of Fuzzy Logic with the Sliding Mode Control to control TRMS. In [14], [15], the SMC method was also used alone, is robust with regard to uncertainties and external disturbances, unfortunately, the problem of chattering is available which causes a high frequency in the input control voltage. The work mentioned in [16], [17] has proposed solutions to reduce the effects of chattering but the author have not developed any practical implementation. The author in [15] used method based on the linearization of non-linear model of TRMS, this approach is generally applied for systems which do not present any uncertainty in their dynamics, unfortunately, the disadvantage of this control is the sensitivity to external disturbances; the author here did not take into account the suitability of practical experimentation with the approved control method [18], [19]. Motivated by the previous problems and for the purpose of presenting the contributions of this paper, our controller has been validated in practical testbench to compensate for the effects of uncertainties, external disturbances and the effects of coupling between two subsystems of TRMS.

The control method is based on the theory of Fuzzy Logic, it is responsible for anticipating and compensating for interactions between control signals through internal states which are considered to be measurable disturbances influencing the dynamics and desired behavior of each sub-system [20]. An adaptation algorithm to correct the problem of the influence of the variation of the parameters on the desired behavior is considered, then to introduce the theory of Backstepping with uncertainty in the control loop where the stability of the system in the closed loop can be ensured by the Lyapunov method. The control approach adopted makes it possible to avoid modeling problems, to extend better robustness and to obtain a desired trajectory following with better precision in the presence of the wind effects frequency.

The rest of the paper is organized as follows; in Section II, a description of Twin Rotor Multi Input Multi Output system (TRMS) is detailed. The dynamic modeling is adopted in Section III. In Section IV, the

design of the Robust Adaptive Fuzzy Backstepping Control (RAFBC) is presented, the results of the experiment are provided in Section V. Finally, conclusion is given in Section VI.

II. Description of Twin Rotor Multi Input Multi Output System (TRMS)

The model studied on behalf of the TRMS, referring to Twin Rotor Mimo System in Fig. 1(a). It is a two-input, non-linear system that represents a helicopter. The concept is provided by the Feedback Company specializing in the design of engineering equipment.

Originally, the model is controlled by software running on Matlab. The acquisition of signals and the sending of commands are done by using an acquisition card of the company Advantech (PCI 1711). At each end of a rod pivoting relative to the base are two propellers driven by two DC motors. The tail propeller provides horizontal displacement while the main propeller provides vertical displacement. A counterweight makes it possible to adjust a desired position of balance. Two optical encoders (HEDS-95440) mounted at the swivel indicate the horizontal and vertical positions of the rod.

Two tachometers installed on the motors (one on each motor) indicate the angular speed of the motors. The system is controlled by the voltage control of the two motors [17].

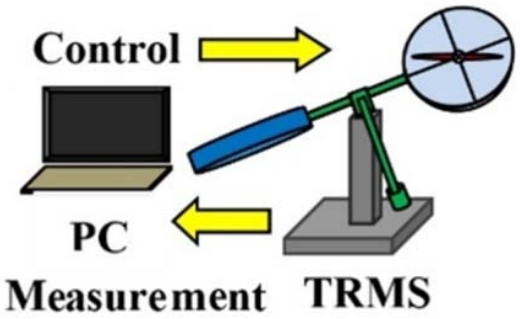

(a)

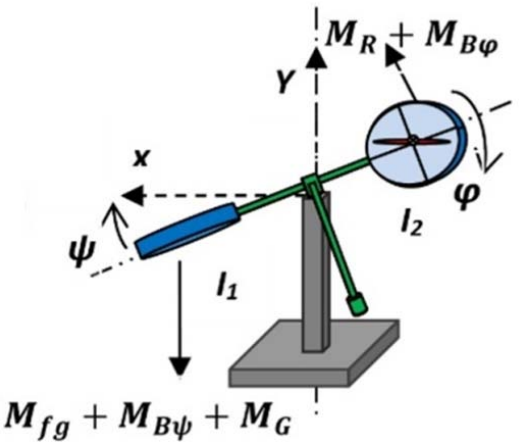

(b)

Figs. 1. TRMS's: (a) Configuration and (b) Simplified descriptive diagram

III. The Twin Rotor Multi Input Multi Output System Model

First, consider the rod rotation in the vertical plane Fig. 1(b), that is, around the horizontal axis. The following momentum equations can be derived for vertical motion [21], [22]:

$$I_1\ddot{\psi} = M_1 - M_{Fg} - M_{B\psi} - M_G \tag{1}$$

M_1 is the nonlinearity caused by the rotor and can be estimated as a second order polynomial:

$$M_1 = a_1\tau_1^2 + b_1\tau_1 \tag{2}$$

The weight of the helicopter provides a gravitational moment around the pivot point, which is described by:

$$M_{Fg} = M_g \sin\psi \tag{3}$$

The friction moment can be estimated by:

$$M_{B\psi} = B_{1\psi}\dot{\psi} - K_{gx}\sin(2\psi)\dot{\varphi}^2 \tag{4}$$

The gyroscopic moment is caused by the Coriolis force; this moment is the result of a change in the displacement position of the main rotor in the azimuth direction, it is described as follows:

$$M_G = K_{gy}M_1\dot{\varphi}\cos\psi \tag{5}$$

The motor M_1 and the electric control circuit are modeled by a transfer function of the first order:

$$\tau_1(S) = \frac{K_{11}}{T_{11}S + T_{10}}u_1(s) \tag{6}$$

Likewise, horizontal movement is described by:

$$I_2\ddot{\varphi} = M_2 - M_{B\varphi} - M_R \tag{7}$$

M_2 is the nonlinearity caused by the rotor and can be estimated as a second order polynomial:

$$M_2 = a_2\tau_2^2 + b_2\tau_2 \tag{8}$$

The friction moment can be estimated by:

$$M_{B\varphi} = B_{1\varphi}\dot{\varphi} \tag{9}$$

M_R is the coupling dynamics, written by the first order transfer function:

$$M_R(S) = \frac{K_c(T_0S + 1)}{T_pS + 1}M_1 \tag{10}$$

In time domain, it can be written as:

$$M_R = 0.375K_ce^{-0.5t}M_1 \tag{11}$$

The motor M_2 and the electric control circuit are modeled by a transfer function of the first order:

$$\tau_2(S) = \frac{K_{22}}{T_{22}S + T_{20}} u_2(s) \tag{12}$$

The dynamic model of the TRMS Fig. 2 is given in by using Newton-Euler method [17] expressed as:

$$\begin{cases} \ddot{\psi} = \frac{1}{I_1}\left[-(1 + K_{gy}\dot{\varphi}\cos\psi)(a_1\tau_1^2 + b_1\tau_1) + \right. \\ \quad -M_g \sin\psi - B_{1\psi}\dot{\psi} + K_{gx}\sin(2\psi)\dot{\varphi}^2\left.\right] \\ \ddot{\varphi} = \frac{1}{I_2}\left[-B_{1\varphi}\dot{\varphi} + a_2\tau_2^2 + b_2\tau_2 + \right. \\ \quad \left. -\left(\frac{K_c(T_0S+1)}{T_pS+1}\right) \times (a_1\tau_1^2 + b_1\tau_1)\right] \end{cases} \tag{13}$$

IV. Robust Adaptive Fuzzy Backstepping Control Design

The dynamic model in (13) can be rewritten in the state-space form, where the state vector is chosen as:

$$x = [x_1, x_2, x_3, x_4, x_5, x_6] = [\psi, \dot{\psi}, \varphi, \dot{\varphi}, \tau_1, \tau_2]^T$$

$$\begin{cases} \dot{x}_1 = x_2 + w_{1v} \\ \dot{x}_2 = -\frac{M_g}{I_1}\sin(x_1) - \frac{B_{1\psi}}{I_1}x_2 + \\ \quad + \frac{K_{gx}}{I_1}x_4{}^2 \sin(2x_1) + \\ \quad + \frac{a_1}{I_1}x_5^2 + \frac{b_1}{I_1}x_5 - \frac{b_1}{I_1}K_{gy}x_4\cos(x_1) + w_{2v} \\ \dot{x}_3 = x_4 + w_{1h} \\ \dot{x}_4 = -\frac{B_{1\varphi}}{I_2}x_4 - \frac{M_R}{I_2} + \frac{a_2}{I_2}x_6^2 + \frac{b_2}{I_2}x_6 + w_{2h} \\ \dot{x}_5 = -\frac{T_{10}}{T_{11}}x_5 + \frac{k_{11}}{T_{11}}u_1 + w_{3v} \\ \dot{x}_6 = -\frac{T_{20}}{T_{22}}x_6 + \frac{k_{22}}{T_{22}}u_2 + w_{3h} \end{cases} \tag{14}$$

where $\{w_{1v}, w_{2v}, w_{3v}, w_{1h}, w_{2h}, w_{3h}\}$ are the wind effects.

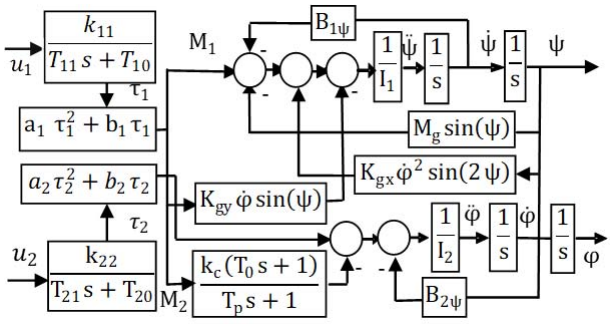

Fig. 2. Mathematical model of TRMS

The state space model (14) can be rearranged as:

$$\begin{cases} \dot{x}_1 = x_2 + w_{1v} \\ \dot{x}_2 = \frac{b_1}{I_1}x_5 + f_{1v} + w_{2v}; \\ \dot{x}_3 = x_4 + w_{1h} \\ \dot{x}_4 = \frac{b_2}{I_2}x_6 + f_{1h} + w_{2h} \\ \dot{x}_5 = f_{2v} + \frac{k_{11}}{T_{11}}u_1 + w_{3v} \\ \dot{x}_6 = f_{2h} + \frac{k_{22}}{T_{22}}u_2 + w_{3h} \end{cases} \tag{15}$$

where:

$$f_{1v} = -\frac{M_g}{I_1}\sin(x_1) - \frac{B_{1\psi}}{I_1}x_2 + \frac{K_{gx}}{I_1}x_4{}^2\sin(2x_1) + \\ + \frac{a_1}{I_1}x_5^2 - \frac{b_1}{I_1}K_{gy}x_4\cos(x_1); f_{2v} = -\frac{T_{10}}{T_{11}}x_5$$
$$f_{1h} = -\frac{B_{1\varphi}}{I_2}x_4 - \frac{M_R}{I_2} + \frac{a_2}{I_2}x_6^2;\ f_{2h} = -\frac{T_{20}}{T_{22}}x_6$$

For subsystem 1, the tracking error is defined as:

$$\begin{cases} e_{1v} = x_1 - x_{1d} \\ e_{1h} = x_3 - x_{3d} \end{cases} \tag{16}$$

Virtual control signals α_{1v} and α_{1h} are introduced:

$$\dot{e}_{1v} = \dot{x}_1 - \dot{x}_{1d} = x_2 + \alpha_{1v} - \alpha_{1v} + w_{1v} - \dot{x}_{1d} = \\ = e_{2v} + \alpha_{1v} + w_{1v} - \dot{x}_{1d}$$

where:

$$e_{2v} = x_2 - \alpha_{1v}$$
$$\dot{e}_{1h} = \dot{x}_3 - \dot{x}_{3d} = x_4 + \alpha_{1h} - \alpha_{1h} + w_3 - \dot{x}_{3d} = \\ = e_{2h} + \alpha_{1h} + w_{1h} - \dot{x}_{3d}$$

where $e_{2h} = x_4 - \alpha_{1h}$. For subsystem 2, a virtual control signal α_{2v} is introduced:

$$\dot{e}_{2v} = \dot{x}_2 - \dot{\alpha}_{1v}$$
$$\dot{e}_{2v} = \frac{b_1}{I_1}x_5 + \frac{b_1}{I_1}\alpha_{2v} - \frac{b_1}{I_1}\alpha_{2v} + f_{1v} + w_{2v} - \dot{\alpha}_{1v}$$
$$\dot{e}_{2v} = \frac{b_1}{I_1}e_{3v} + \frac{b_1}{I_1}\alpha_{2v} + f_{1v} + w_{2v} - \dot{\alpha}_{1v}$$

where $e_{3v} = x_5 - \alpha_{2v}$.

$$\dot{e}_{2h} = \dot{x}_4 - \dot{\alpha}_{1h}$$
$$\dot{e}_{2h} = \frac{b_2}{I_2}x_6 + \frac{b_2}{I_2}\alpha_{2h} - \frac{b_2}{I_2}\alpha_{2h} + f_{1h} + w_{2h} - \dot{\alpha}_{1h}$$
$$\dot{e}_{2h} = \frac{b_2}{I_2}e_{3h} + \frac{b_2}{I_2}\alpha_{2h} + f_{1h} + w_{2h} - \dot{\alpha}_{1h}$$

where $e_{3h} = x_6 - \alpha_{2h}$. For subsystem 3, a control law signals u_1 and u_2 are extracted:

$$\dot{e}_{3v} = \dot{x}_5 - \dot{\alpha}_{2v} = f_{2v} + \frac{k_{11}}{T_{11}}u_1 - \dot{\alpha}_{2v} + w_{3v}$$
$$\dot{e}_{3h} = \dot{x}_6 - \dot{\alpha}_{2h} = f_{2h} + \frac{k_{22}}{T_{22}}u_2 - \dot{\alpha}_{2h} + w_{3h}$$

The physical parameters of the TRMS are shown in Table I.

IV.1. Robust Adaptive Fuzzy Backstepping Control Using Lyapunov

Step 1, the Lyapunov function is redesigned as follows:

$$V_1 = \frac{1}{2\beta_{1v}}e_{1v}^2 + \frac{1}{2\beta_{1h}}e_{1h}^2 \tag{17}$$

with (β_{1v}, β_{1h})>1. The derivative of Equation (17) is given by the following expression:

$$\dot{V}_1 = \frac{1}{\beta_{1v}}e_{1v}\left(e_{2v} + \alpha_{1v} + \hat{f}_{1v}\right) + \frac{1}{\beta_{1v}}e_{1v}w_{1v} + \\ + \frac{1}{\beta_{1h}}e_{1h}\left(e_{2h} + \alpha_{1h} + \hat{f}_{1h}\right) + \frac{1}{\beta_{1h}}e_{1h}w_{1h} \tag{18}$$

where $\hat{f}_{1v} = -\dot{x}_{1d}$ and $\hat{f}_{1h} = -\dot{x}_{3d}$ define:

$$\begin{cases}\alpha_{1v} = -\lambda_{1v}\beta_{1v}e_{1v} - \varphi_{1v},\ \lambda_{1v} > 0\\ \alpha_{1h} = -\lambda_{1h}\beta_{1h}e_{1h} - \varphi_{1h},\ \lambda_{1h} > 0\end{cases} \tag{19}$$

where φ_{1v} and φ_{1h} are a fuzzy-system for approximating nonlinear functions$\hat{f}_{1v}$ and $\hat{f}_{1h}$,then:

$$\dot{V}_1 = -\lambda_{1v}e_{1v}^2 + \frac{1}{\beta_{1v}}e_{1v}e_{2v} + \frac{1}{\beta_{1v}}e_{1v}(\hat{f}_{1v} - \varphi_{1v}) + \\ + \frac{1}{\beta_{1v}}e_{1v}w_{1v} - \lambda_{1h}e_{1h}^2 + \frac{1}{\beta_{1h}}e_{1h}e_{2h} + \\ + \frac{1}{\beta_{1h}}e_{1h}w_{1h} + + \frac{1}{\beta_{1h}}e_{1h}(\hat{f}_{1h} - \varphi_{1h}) \tag{20}$$

TABLE I
PHYSICAL PARAMETERS OF TRMS [17]

	Definition	Value
I_1	Inertia of motor1	6.8×10^{-2} kg m^2
I_2	Inertia of motor2	2×10^{-2} kg m^2
a_1	Fixed constant for M1	0.0135
b_1	Fixed constant for M2	0.0924
a_2	Fixed constant1 for M1	0.02
b_2	Fixed constant2 for M2	0.09
M_{Fg}	Gravity momentum	0.32
$B_{1\psi}$	Friction momentum	6×10^{-3} N m s/rad
$B_{1\varphi}$	Friction momentum	1×10^{-1} N m s/rad
K_{gy}	Gyroscopic momentum	0.05 s/rad
K_{gx}	Gyroscopic momentum	0.0163 s/rad
K_{11}	Gain motor1	1.1
K_{22}	Gain motor2	0.8
T_{11}	Denominator motor1	1.2
T_{10}	Numerator motor1	1
T_{20}	Denominator motor1	1
T_{22}	Numerator motor2	1
T_0	Reaction momentum	3.5
T_p	Reaction momentum	2
K_c	Reaction momentum gain	-0.2

Step 2, the Lyapunov function is redesigned as:

$$V_2 = V_1 + \frac{I_1}{2b_1\beta_{2v}}e_{2v}^2 + \frac{I_2}{2b_2\beta_{2h}}e_{2h}^2 \tag{21}$$

with (β_{2v}, β_{2h})>1. The derivative of Equation (21) is given by the following expression:

$$\dot{V}_2 = \dot{V}_1 + \frac{I_1}{b_1\beta_{2v}}e_{2v}\dot{e}_{2v} + \frac{I_2}{b_2\beta_{2h}}e_{2h}\dot{e}_{2h} \\ \dot{V}_2 = \dot{V}_1 + \frac{1}{\beta_{2v}}e_{2v}\left(e_{3v} + \alpha_{2v} + \hat{f}_{2v}\right) + \\ + \frac{I_1}{b_1\beta_{2v}}e_{2v}w_{2v} + \frac{1}{\beta_{2h}}e_{2h}\left(e_{3h} + \alpha_{2h} + \hat{f}_{2h}\right) + \\ + \frac{I_2}{b_2\beta_{2h}}e_{2h}w_{2h} \tag{22}$$

where:

$$\hat{f}_{2v} = \frac{I_1}{b_1}(f_{1v} - \dot{\alpha}_{1v}), \qquad \hat{f}_{2h} = \frac{I_2}{b_2}(f_{1h} - \dot{\alpha}_{1h})$$

Define:

$$\begin{cases}\alpha_{2v} = -\lambda_{2v}\beta_{2v}e_{2v} - \dfrac{\beta_{2v}}{\beta_{1v}}e_{1v} - \varphi_{2v},\ \lambda_{2v} > 0\\ \alpha_{2h} = -\lambda_{2h}\beta_{2h}e_{2h} - \dfrac{\beta_{2h}}{\beta_{1h}}e_{1h} - \varphi_{2h},\ \lambda_{2h} > 0\end{cases} \tag{23}$$

where φ_{2v} and φ_{2h} are a fuzzy system for approximating nonlinear functions$\hat{f}_{2v}$ and $\hat{f}_{2h}$,then:

$$\dot{V}_2 = -\lambda_{1v}e_{1v}^2 - \lambda_{2v}e_{2v}^2 + \frac{1}{\beta_{2v}}e_{2v}e_{3v} + \\ + \frac{1}{\beta_{1v}}e_{1v}w_{1v} + \frac{I_1}{b_1\beta_{2v}}e_{2v}w_{2v} + \frac{1}{\beta_{1h}}e_{1h}w_{1h} + \\ + \frac{I_2}{b_2\beta_{2h}}e_{2h}w_{2h} - \lambda_{1h}e_{1h}^2 - \lambda_{2h}e_{2h}^2 + \\ + \frac{1}{\beta_{2h}}e_{2h}e_{3h} + \frac{1}{\beta_{1v}}e_{1v}(\hat{f}_{1v} - \varphi_{1v}) + \\ + \frac{1}{\beta_{2v}}e_{2v}(\hat{f}_{2v} - \varphi_{2v}) + \frac{1}{\beta_{1h}}e_{1h}(\hat{f}_{1h} - \varphi_{1h}) + \\ + \frac{1}{\beta_{2h}}e_{2h}(\hat{f}_{2h} - \varphi_{2h}) \tag{24}$$

Step 3, the Lyapunov function is redesigned as:

$$V_3 = V_2 + \frac{T_{11}}{2k_{11}\beta_{3v}}e_{3v}^2 + \frac{T_{22}}{2k_{22}\beta_{3h}}e_{3h}^2 \tag{25}$$

with (β_{3v}, β_{3h})>1. The derivative of Equation (25) is given by the following expression:

$$\dot{V}_3 = \dot{V}_2 + \frac{T_{11}}{k_{11}\beta_{3v}}e_{3v}\dot{e}_{3v} + \frac{T_{22}}{k_{22}\beta_{3h}}e_{3h}\dot{e}_{3h} \\ = \dot{V}_2 + \frac{1}{\beta_{3v}}e_{3v}(u_1 + \hat{f}_{3v}) + \frac{T_{11}}{\beta_3 k_{11}}e_{3v}w_{3v} \\ + \frac{1}{\beta_{3h}}e_{3h}(u_2 + \hat{f}_{3h}) + \frac{T_{22}}{\beta_{3h}k_{22}}e_{3h}w_{3h} \tag{26}$$

where:

$$\hat{f}_{3v} = \frac{T_{11}}{k_{11}}(f_{2v} - \dot{\alpha}_{2v});\ \hat{f}_{3h} = \frac{T_{22}}{k_{22}}(f_{2h} - \dot{\alpha}_{2h})$$

$$\begin{aligned}\dot{V}_3 = &-\lambda_{1v}e_{1v}^2 - \lambda_{2v}e_{2v}^2 + \frac{1}{\beta_{1v}}e_{1v}(\hat{f}_{1v} - \varphi_{1v}) \\ &+ \frac{1}{\beta_{2v}}e_{2v}(\hat{f}_{2v} - \varphi_{2v}) \\ &+ \frac{1}{\beta_{3v}}e_{3v}\left(u_1 + \hat{f}_{3v} + \frac{\beta_{3v}}{\beta_{2v}}e_{2v}\right) + \frac{1}{\beta_{1v}}e_{1v}w_{1v} \\ &+ \frac{I_1}{b_1\beta_{2v}}e_{2v}w_{2v} + \frac{T_{11}}{k_{11}\beta_{3v}}e_{3v}w_{3v} - \lambda_{1h}e_{1h}^2 \\ &- \lambda_{2h}e_{2h}^2 + \frac{1}{\beta_{1h}}e_{1h}(\hat{f}_{1h} - \varphi_{1h}) \\ &+ \frac{1}{\beta_{2h}}e_{2h}(\hat{f}_{2h} - \varphi_{2h}) \\ &+ \frac{1}{\beta_{3h}}e_{3h}\left(u_2 + \hat{f}_{3h} + \frac{\beta_{3h}}{\beta_{2h}}e_{2h}\right) + \frac{1}{\beta_{1h}}e_{1h}w_{1h} \\ &+ \frac{I_2}{b_2\beta_{2h}}e_{2h}w_{2h} + \frac{T_{22}}{k_{22}\beta_{3h}}e_{3h}w_{3h}\end{aligned} \tag{27}$$

The control law is redesigned as follows:

with, λ_{3v}>0:

$$u_1 = -\lambda_{3v}\beta_{3v}e_{3v} - \frac{\beta_{3v}}{\beta_{2v}}e_{2v} - \varphi_{3v}$$

with, λ_{3h}>0:

$$u_2 = -\lambda_{3h}\beta_{3h}e_{3h} - \frac{\beta_{3h}}{\beta_{2h}}e_{2h} - \varphi_{3h}$$

Then (27) can be rewritten as:

$$\begin{aligned}\dot{V}_3 = &-\lambda_{1v}e_{1v}^2 - \lambda_{2v}e_{2v}^2 - \lambda_{3v}e_{3v}^2 \\ &+ \frac{1}{\beta_{1v}}e_{1v}(\hat{f}_{1v} - \varphi_{1v}) + \frac{1}{\beta_{2v}}e_{2v}(\hat{f}_{2v} - \varphi_{2v}) \\ &+ \frac{1}{\beta_{3v}}e_{3v}(\hat{f}_{3v} - \varphi_{3v}) + \frac{1}{\beta_{1v}}e_{1v}w_{1v} \\ &+ \frac{I_1}{b_1\beta_{2v}}e_{2v}w_{2v} + \frac{T_{11}}{\beta_{3v}k_{11}}e_{3v}w_{3v} - \lambda_{1h}e_{1h}^2 \\ &- \lambda_{2h}e_{2h}^2 - \lambda_{3h}e_{3h}^2 + \frac{1}{\beta_{1h}}e_{1h}(\hat{f}_{1h} - \varphi_{1h}) \\ &+ \frac{1}{\beta_{2h}}e_{2h}(\hat{f}_{2h} - \varphi_{2h}) + \frac{1}{\beta_{3h}}e_{3h}(\hat{f}_{3h} - \varphi_{3h}) \\ &+ \frac{1}{\beta_{1h}}e_{1h}w_{1h} + \frac{I_2}{b_2\beta_{2h}}e_{2h}w_{2h} + \frac{T_{22}}{\beta_{3h}k_{22}}e_{3h}w_{3h}\end{aligned} \tag{28}$$

IV.2. Fuzzy Logic System

In this paper, the fuzzy logic with product inference, singleton fuzzifier and center average defuzzifier is used according to "IF-THEN theory", is written in the following from [16]:

R^k: IFx_1 is $F_1^k$and ..... x_n is, THEN y_i is G^k, k=1,2,....N

where the input vector is X=[x_1,.....,x_n]$\epsilon\mathbb{R}^n$ and the output vector is $\bar{Y}\epsilon\ \mathbb{R}^n$.

TABLE II
FUZZY SETS AND DEFINITIONS

Fuzzy sets				
NB	NS	ZE	PS	PB
negative big	negative small	zero environ	positive small	positive big

The fuzzy membership functions $\mu_{F_l^k}(x_l)$ and $\mu_{G^k}(\bar{Y})$ are associated with $F_l^k(l = 1, \dots\dots, n)$ and G^i respectively. To determine the output of the fuzzy logic system, the relation is followed as:

$$\bar{Y}\left(\frac{X}{W}\right) = \frac{\sum_{k=1}^{N}\bar{y}_k\prod_{l=1}^{n}\mu_{F_l^k}(x_l)}{\sum_{k=1}^{N}\left[\prod_{l=1}^{n}\mu_{F_l^k}(x_l)\right]} \tag{29}$$

where:

$$\bar{y}_k = \max_{y\,\epsilon\,R}\mu_{G^k}(y), \qquad \mu_{F_l^k}(x_l)$$

and, G^k denote Gaussian membership functions with respect to fuzzy Sets F_1^k and G^k let:

$$\Theta_i(X) = \frac{\prod_{l=1}^{n}\mu_{F_l^k}(x_l)}{\sum_{k=1}^{N}\left[\prod_{l=1}^{n}\mu_{F_l^k}(x_l)\right]} \tag{30}$$

Denoting, the vector of fuzzy basis functions is:

$$\Theta(X) = [\Theta_1(X), \Theta_2(X), \dots\dots, \Theta_N(X)]^T$$

and the vector of consequent parameters is:

$$[W^T = [\,\bar{y}_1, \bar{y}_2, \dots\dots, \bar{y}_N]^T = [W_1, W_2, \dots\dots, W_N]$$

Then, the fuzzy logic system can be rewritten as:

$$\bar{Y}\left(\frac{X}{W}\right) = W^T\Theta(X) \tag{31}$$

In our work, five fuzzy sets are defined for each variable $(e_v\ , e_h)$, are presented in Table II.

IV.3. Stability, Adaptive Law Design

Now, consider the following Lyapunov candidate function:

$$\begin{aligned}V = V_3 &+ \frac{1}{2r_{1v}\beta_{1v}}\tilde{\theta}_{1v}^T\tilde{\theta}_{1v} + \frac{1}{2r_{2v}\beta_{2v}}\tilde{\theta}_{2v}^T\tilde{\theta}_{2v} \\ &+ \frac{1}{2r_{3v}\beta_{3v}}\tilde{\theta}_{3v}^T\tilde{\theta}_{3v} + \frac{1}{2r_{1h}\beta_{1h}}\tilde{\theta}_{1h}^T\tilde{\theta}_{1h} \\ &+ \frac{1}{2r_{2h}\beta_{2h}}\tilde{\theta}_{2h}^T\tilde{\theta}_{2h} + \frac{1}{2r_{3h}\beta_{3h}}\tilde{\theta}_{3h}^T\tilde{\theta}_{3h}\end{aligned} \tag{32}$$

where (r_1,r_2,r_3)>0

$$\begin{cases}\tilde{\theta}_{1v} = \tilde{\theta}_{1v}^* - \tilde{\theta}_{1v} \\ \tilde{\theta}_{2v} = \tilde{\theta}_{2v}^* - \tilde{\theta}_{2v} \\ \tilde{\theta}_{3v} = \tilde{\theta}_{3v}^* - \tilde{\theta}_{3v}\end{cases} \text{and} \begin{cases}\tilde{\theta}_{1h} = \tilde{\theta}_{1h}^* - \tilde{\theta}_{1h} \\ \tilde{\theta}_{2h} = \tilde{\theta}_{2h}^* - \tilde{\theta}_{2h} \\ \tilde{\theta}_{3h} = \tilde{\theta}_{3h}^* - \tilde{\theta}_{3h}\end{cases}$$

The time derivative of Equation (32) is given by the following expression:

$$\begin{aligned}\dot{V} &= \dot{V}_3 + \frac{1}{r_{1v}\beta_{1v}}\tilde{\theta}_{1v}^T\dot{\tilde{\theta}}_{1v} + \frac{1}{r_{2v}\beta_{2v}}\tilde{\theta}_{2v}^T\dot{\tilde{\theta}}_{2v} \\ &+ \frac{1}{r_{3v}\beta_{3v}}\tilde{\theta}_{3v}^T\dot{\tilde{\theta}}_{3v} + \frac{1}{r_{1h}\beta_{1h}}\tilde{\theta}_{1h}^T\dot{\tilde{\theta}}_{1h} + \frac{1}{r_{2h}\beta_{2h}}\tilde{\theta}_{2h}^T\dot{\tilde{\theta}}_{2h} \\ &+ \frac{1}{r_{3h}\beta_{3h}}\tilde{\theta}_{3h}^T\dot{\tilde{\theta}}_{3h} = -\lambda_{1v}e_{1v}^2 - \lambda_{2v}e_{2v}^2 - \lambda_{3v}e_{3v}^2 \\ &+ \frac{1}{\beta_{1v}}e_{1v}\left(\hat{f}_{1v} - \tilde{\theta}_{1v}^{*\,T}\xi_{1v}\right) + \frac{1}{\beta_{2v}}e_{2v}\left(\hat{f}_{2v} - \tilde{\theta}_{2v}^{*\,T}\xi_{2v}\right) \\ &+ \frac{1}{\beta_{3v}}e_{3v}\left(\hat{f}_{3v} - \tilde{\theta}_{3v}^{*\,T}\xi_{3v}\right) + \frac{1}{\beta_{1v}}e_{1v}\tilde{\theta}_{1v}^{\,T}\xi_{1v} \\ &+ \frac{1}{\beta_{2v}}e_{2v}\tilde{\theta}_{2v}^{\,T}\xi_{2v} + \frac{1}{\beta_{3v}}e_{3v}\tilde{\theta}_{3v}^{\,T}\xi_{3v} - \frac{1}{r_{1v}\beta_{1v}}\tilde{\theta}_{1v}^T\dot{\theta}_{1v} \\ &- \frac{1}{r_{2v}\beta_{2v}}\tilde{\theta}_{2v}^T\dot{\theta}_{2v} - \frac{1}{r_{3v}\beta_{3v}}\tilde{\theta}_{3v}^T\dot{\theta}_{3v} + \frac{1}{\beta_{1v}}e_{1v}w_{1v} \\ &+ \frac{I_1}{b_1\beta_{2v}}e_{2v}w_{2v} + \frac{T_{11}}{\beta_{3v}k_{11}}e_{3v}w_{3v} - \lambda_{1h}e_{1h}^2 \\ &- \lambda_{2h}e_{2h}^2 - \lambda_{3h}e_{3h}^2 + \frac{1}{\beta_{1h}}e_{1h}\left(\hat{f}_{1h} - \tilde{\theta}_{1h}^{*\,T}\xi_{1h}\right) \\ &+ \frac{1}{\beta_{2h}}e_{2h}\left(\hat{f}_{2h} - \tilde{\theta}_{2h}^{*\,T}\xi_{2h}\right) \\ &+ \frac{1}{\beta_{3h}}e_{3h}\left(\hat{f}_{3h} - \tilde{\theta}_{3h}^{*\,T}\xi_{3h}\right) + \frac{1}{\beta_{1h}}e_{1h}\tilde{\theta}_{1h}^{\,T}\xi_{1h} \\ &+ \frac{1}{\beta_{2h}}e_{2h}\tilde{\theta}_{2h}^{\,T}\xi_{2h} + \frac{1}{\beta_{3h}}e_{3h}\tilde{\theta}_{3h}^{\,T}\xi_{3h} \\ &- \frac{1}{r_{1h}\beta_{1h}}\tilde{\theta}_{1h}^T\dot{\theta}_{1h} - \frac{1}{r_{2h}\beta_{2h}}\tilde{\theta}_{2h}^T\dot{\theta}_{2h} - \frac{1}{r_{3h}\beta_{3h}}\tilde{\theta}_{3h}^T\dot{\theta}_{3h} \\ &+ \frac{1}{\beta_{1h}}e_{1h}w_{1h} + \frac{I_2}{b_2\beta_{2h}}e_{2h}w_{2h} + \frac{T_{22}}{\beta_{3h}k_{22}}e_{3h}w_{3h} \\ &\le -\lambda_{1v}e_{1v}^2 - \lambda_{2v}e_{2v}^2 - \lambda_{3v}e_{3v}^2 + \frac{1}{\beta_{1v}}|e_{1v}\varepsilon_{1v}| \\ &+ \frac{1}{\beta_{2v}}|e_{2v}\varepsilon_{2v}| + \frac{1}{\beta_{3v}}|e_{3v}\varepsilon_{3v}| \\ &+ \tilde{\theta}_{1v}^{\,T}\frac{1}{\beta_{1v}}\left(e_{1v}\xi_{1v} - \frac{1}{r_{1v}}\dot{\theta}_{1v}\right) + \frac{I_1}{b_1\beta_{2v}}e_{2v}w_{2v} \\ &+ \tilde{\theta}_{2v}^{\,T}\frac{1}{\beta_{2v}}\left(e_{2v}\xi_{2v} - \frac{1}{r_{2v}}\dot{\theta}_{2v}\right) + \frac{1}{\beta_{1v}}e_{1v}w_{1v} \\ &+ \tilde{\theta}_{3v}^{\,T}\frac{1}{\beta_{3v}}\left(e_{3v}\xi_{3v} - \frac{1}{r_{3v}}\dot{\theta}_{3v}\right) + \frac{T_{11}}{\beta_3 k_{11}}e_{3v}w_{3v} \\ &- \lambda_{1h}e_{1h}^2 - \lambda_{2h}e_{2h}^2 - \lambda_{3h}e_{3h}^2 + \frac{1}{\beta_{1h}}|e_{1h}\varepsilon_{1h}| \\ &+ \frac{1}{\beta_{2h}}|e_{2h}\varepsilon_{2h}| + \frac{1}{\beta_{3h}}|e_{3h}\varepsilon_{3h}| \\ &+ \tilde{\theta}_{1h}^{\,T}\frac{1}{\beta_{1h}}\left(e_{1h}\xi_{1h} - \frac{1}{r_{1h}}\dot{\theta}_{1h}\right) + \frac{1}{\beta_{1h}}e_{1h}w_{1h} \\ &+ \tilde{\theta}_{2h}^{\,T}\frac{1}{\beta_{2h}}\left(e_{2h}\xi_{2h} - \frac{1}{r_{2h}}\dot{\theta}_{2h}\right) + \frac{I_2}{b_2\beta_{2h}}e_{2h}w_{2h} \\ &+ \tilde{\theta}_{3h}^{\,T}\frac{1}{\beta_{3h}}\left(e_{3h}\xi_{3h} - \frac{1}{r_{3h}}\dot{\theta}_{3h}\right) + \frac{T_{22}}{\beta_{3h}k_{22}}e_{3h}w_{3h}\end{aligned} \tag{33}$$

Equation (33) shows that for the same control parameters λ_{1v}, λ_{2v}, λ_{3v}, λ_{1h}, λ_{2h} and λ_{3h}, as long as: the designed parameters: (β_{1v}, β_{2v}, β_{3v} β_{1h} β_{2h} and β_{3h})>1, the influence of fuzzy approximation error and external disturbance on system stability can be reduced. For convenience, symbol (Γ) is introduced, where:

$$\begin{aligned}\Gamma &= -\lambda_{1v}e_{1v}^2 - \lambda_{2v}e_{2v}^2 - \lambda_{3v}e_{3v}^2 + \frac{1}{\beta_{1v}}|e_{1v}\varepsilon_{1v}| \\ &+ \frac{1}{\beta_{2v}}|e_{2v}\varepsilon_{2v}| + \frac{1}{\beta_{3v}}|e_{3v}\varepsilon_{3v}| \\ &+ \tilde{\theta}_{1v}^{\,T}\frac{1}{\beta_{1v}}\left(e_{1v}\xi_{1v} - \frac{1}{r_{1v}}\dot{\theta}_{1v}\right) - \lambda_{1h}e_{1h}^2 - \lambda_{2h}e_{2h}^2 \\ &- \lambda_{3h}e_{3h}^2 + \frac{1}{\beta_{1h}}|e_{1h}\varepsilon_{1h}| + \frac{1}{\beta_{2h}}|e_{2h}\varepsilon_{2h}| \\ &+ \frac{1}{\beta_{3h}}|e_{3h}\varepsilon_{3h}| + \tilde{\theta}_{1h}^{\,T}\frac{1}{\beta_{1h}}\left(e_{1h}\xi_{1h} - \frac{1}{r_{1h}}\dot{\theta}_{1h}\right) \\ &+ \frac{1}{\beta_{1h}}e_{1h}w_{1h} + \tilde{\theta}_{2h}^{\,T}\frac{1}{\beta_{2h}}\left(e_{2h}\xi_{2h} - \frac{1}{r_{2h}}\dot{\theta}_{2h}\right) \\ &+ \frac{I_2}{b_2\beta_{2h}}e_{2h}w_{2h} + \tilde{\theta}_{3h}^{\,T}\frac{1}{\beta_{3h}}\left(e_{3h}\xi_{3h} - \frac{1}{r_{3h}}\dot{\theta}_{3h}\right) \\ &+ \frac{T_{22}}{\beta_{3h}k_{22}}e_{3h}w_{3h}\end{aligned} \tag{34}$$

Select the positive coefficients $\lambda_{1v}, \lambda_{2v}, \lambda_{3v}$, $\lambda_{1h}, \lambda_{2h}$and λ_{3h} as:

$$\begin{cases}\lambda_{1v} = \eta_{1v} + \frac{1}{2} + \frac{1}{2\rho_v{}^2\beta_{1v}^2} \\ \lambda_{2v} = \eta_{2v} + \frac{1}{2} + \frac{1}{2\rho_v{}^2\left(\frac{b_1}{I_1}\beta_{2v}\right)^2} \\ \lambda_{3v} = \eta_{3v} + \frac{1}{2} + \frac{1}{2\rho_v{}^2\left(\frac{k_{11}}{T_{11}}\beta_{3v}\right)^2}\end{cases} \tag{35}$$

$$\begin{cases}\lambda_{1h} = \eta_{1h} + \frac{1}{2} + \frac{1}{2\rho_h{}^2\beta_{1h}^2} \\ \lambda_{2h} = \eta_{2h} + \frac{1}{2} + \frac{1}{2\rho_h{}^2\left(\frac{b_2}{I_2}\beta_{2h}\right)^2} \\ \lambda_{3h} = \eta_{3h} + \frac{1}{2} + \frac{1}{2\rho_h{}^2\left(\frac{k_{22}}{T_{22}}\beta_{3h}\right)^2}\end{cases}$$

where: $\eta_{1v}, \eta_{2v}, \eta_{3v}, \eta_{1h}, \eta_{2h}, \eta_{3h}, \rho_v$ and ρ_h are constants, so ($\lambda_{1v}, \lambda_{2v}, \lambda_{3v}, \lambda_{1h}, \lambda_{2h}$ and λ_{3h})>0.5.

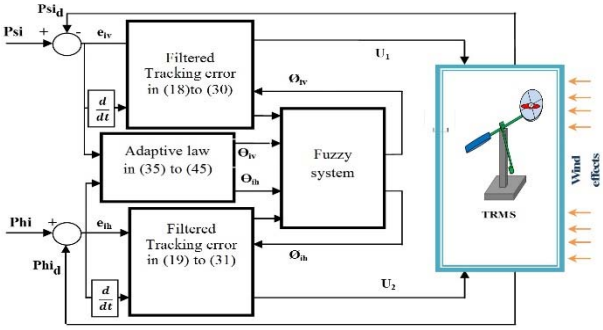

Fig. 3. Proposed Adaptive Fuzzy Backstepping Control strategy

Substituting (35) into (34) results in:

$$\begin{aligned}\Gamma = &-\eta_{1v}e_{1v}^2-\eta_{2v}e_{2v}^2-\eta_{3v}e_{3v}^2-\frac{1}{2}e_{1v}^2-\frac{1}{2}e_{2v}^2-\frac{1}{2}e_{3v}^2-\frac{1}{2\rho_v{}^2\beta_{1v}^2}e_{1v}^2-\frac{1}{2\rho_v{}^2\left(\frac{b_1}{I_1}\beta_{2v}\right)^2}e_{2v}^2\\&-\frac{1}{2\rho_v{}^2\left(\frac{k_{11}}{T_{11}}\beta_{3v}\right)^2}e_{3v}^2+\tilde{\theta}_{1v}{}^T\frac{1}{\beta_{1v}}\left(e_{1v}\xi_{1v}-\frac{1}{r_{1v}}\dot{\theta}_{1v}\right)+\frac{1}{\beta_{2v}}|e_{2v}\varepsilon_{2v}|\\&+\tilde{\theta}_{2v}{}^T\frac{1}{\beta_{2v}}\left(e_{2v}\xi_{2v}-\frac{1}{r_{2v}}\dot{\theta}_{2v}\right)+\tilde{\theta}_{3v}{}^T\frac{1}{\beta_{3v}}\left(e_{3v}\xi_{3v}-\frac{1}{r_{3v}}\dot{\theta}_{3v}\right)+\frac{1}{\beta_{1v}}|e_{1v}\varepsilon_{1v}|+\frac{1}{\beta_{3v}}|e_{3v}\varepsilon_{3v}|\\&+\frac{1}{\beta_{1v}}e_{1v}w_{1v}+\frac{I_1}{b_1\beta_{2v}}e_{2v}w_{2v}+\frac{T_{11}}{\beta_{3v}k_{11}}e_{3v}w_{3v}-\eta_{1h}e_{1h}^2-\eta_{2h}e_{2h}^2-\eta_{3h}e_{3h}^2-\frac{1}{2}e_{1h}^2-\frac{1}{2}e_{2h}^2\\&-\frac{1}{2}e_{3h}^2-\frac{1}{2\rho_h{}^2\beta_{1h}^2}e_{1h}^2-\frac{1}{2\rho_h{}^2\left(\frac{b_2}{I_2}\beta_{2h}\right)}e_{2h}^2-\frac{1}{\beta_{1h}}|e_{1h}\varepsilon_{1h}|+\frac{1}{2\rho_h{}^2\left(\frac{k_{22}}{T_{22}}\beta_{3h}\right)^2}e_{3h}^2\\&+\tilde{\theta}_{1h}{}^T\frac{1}{\beta_{1h}}\left(e_{1h}\xi_{1h}-\frac{1}{r_{1h}}\dot{\theta}_{1h}\right)+\tilde{\theta}_{2h}{}^T\frac{1}{\beta_{2h}}\left(e_{2h}\xi_{2h}-\frac{1}{r_{2h}}\dot{\theta}_{2h}\right)+\frac{1}{\beta_{2h}}|e_{2h}\varepsilon_{2h}|\\&+\tilde{\theta}_{3h}{}^T\frac{1}{\beta_{3h}}\left(e_{3h}\xi_{3h}-\frac{1}{r_{3h}}\dot{\theta}_{3h}\right)+\frac{1}{\beta_{3h}}|e_{3h}\varepsilon_{3h}|+\frac{1}{\beta_{1h}}e_{1h}w_{1h}+\frac{I_2}{b_2\beta_{2h}}e_{2h}w_{2h}+\frac{T_{22}}{\beta_{3h}k_{22}}e_{3h}w_{3h}\end{aligned}\tag{36}$$

Because (β_1, β_2 and β_3)≥ 1:

$$\begin{aligned}&-\frac{1}{2}e_{1v}^2-\frac{1}{2}e_{2v}^2-\frac{1}{2}e_{3v}^2+\frac{1}{\beta_{1v}}|e_{1v}\varepsilon_{1v}|+\frac{1}{\beta_{2v}}|e_{2v}\varepsilon_{2v}|+\frac{1}{\beta_{3v}}|e_{3v}\varepsilon_{3v}|\\&\leq\frac{1}{2}\varepsilon_{1v}^2+\frac{1}{2}\varepsilon_{2v}^2+\frac{1}{2}\varepsilon_{3v}^2-\frac{1}{2}e_{1h}^2-\frac{1}{2}e_{2h}^2-\frac{1}{2}e_{3h}^2+\frac{1}{\beta_{1h}}|e_{1h}\varepsilon_{1h}|+\frac{1}{\beta_{2h}}|e_{2h}\varepsilon_{2h}|+\frac{1}{\beta_{3h}}|e_{3h}\varepsilon_{3h}|\\&\leq\ \frac{1}{2}\varepsilon_{1h}^2+\frac{1}{2}\varepsilon_{2h}^2+\frac{1}{2}\varepsilon_{3h}^2-\frac{1}{2\rho_v{}^2\beta_{1v}^2}e_{1v}^2-\frac{1}{2\rho_v{}^2\left(\frac{b_1}{I_1}\beta_{2v}\right)^2}e_{2v}^2-\frac{1}{2\rho_v{}^2\left(\frac{k_{11}}{T_{11}}\beta_{3v}\right)^2}e_{3v}^2\\&+\ \frac{1}{\beta_{1v}}e_{1v}w_{1v}+\frac{I_1}{b_1\beta_{2v}}e_{2v}w_{2v}+\frac{T_{11}}{\beta_{3v}k_{11}}e_{3v}w_{3v}\\&\leq\frac{1}{2}\rho_v{}^2w_{1v}^2+\frac{1}{2}\rho_v{}^2w_{2v}^2+\frac{1}{2}\rho_v{}^2w_{3v}^2-\frac{1}{2\rho_h{}^2\beta_{1h}^2}e_{1h}^2-\frac{1}{2\rho_h{}^2\left(\frac{b_1}{I_1}\beta_{2h}\right)^2}e_{2h}^2-\frac{1}{2\rho_h{}^2\left(\frac{k_{22}}{T_{22}}\beta_{3h}\right)^2}e_{3h}^2\\&+\frac{1}{\beta_{1h}}e_{1h}w_{1h}+\frac{I_2}{b_2\beta_{2h}}e_{2h}w_{2h}+\frac{T_{22}}{\beta_{3h}k_{22}}e_{3h}w_{3h}\leq\frac{1}{2}\rho_h{}^2w_{1h}^2+\frac{1}{2}\rho_h{}^2w_{2h}^2+\frac{1}{2}\rho_h{}^2w_{3h}^2\end{aligned}\tag{37}$$

Then, the inequality can be obtained as follows:

$$\begin{aligned}\Gamma\leq&-\eta_{1v}e_{1v}^2-\eta_{2v}e_{2v}^2-\eta_{3v}e_{3v}^2+\tilde{\theta}_{1v}{}^T\frac{1}{\beta_{1v}}\left(e_{1v}\xi_{1v}-\frac{1}{r_{1v}}\dot{\theta}_{1v}\right)+\frac{1}{2}\varepsilon_{1v}^2+\frac{1}{2}\rho_v{}^2w_{1v}^2+\tilde{\theta}_{2v}{}^T\frac{1}{\beta_{2v}}\left(e_{2v}\xi_{2v}-\frac{1}{r_{2v}}\dot{\theta}_{2v}\right)\\&+\frac{1}{2}\varepsilon_{2v}^2+\frac{1}{2}\rho_v{}^2w_{2v}^2+\tilde{\theta}_{3v}{}^T\frac{1}{\beta_{3v}}\left(e_{3v}\xi_{3v}-\frac{1}{r_{3v}}\dot{\theta}_{3v}\right)+\frac{1}{2}\varepsilon_{3v}^2+\frac{1}{2}\rho_v{}^2w_{3v}^2\\&+\tilde{\theta}_{1h}{}^T\frac{1}{\beta_{1h}}\left(e_{1h}\xi_{1h}-\frac{1}{r_{1h}}\dot{\theta}_{1h}\right)-\eta_{1h}e_{1h}^2+\frac{1}{2}\varepsilon_{1h}^2+\tilde{\theta}_{2h}{}^T\frac{1}{\beta_{2h}}\left(e_{2h}\xi_{2h}-\frac{1}{r_{2h}}\dot{\theta}_{2h}\right)-\eta_{2h}e_{2h}^2\\&+\frac{1}{2}\varepsilon_{2h}^2+\tilde{\theta}_{3h}{}^T\frac{1}{\beta_{3h}}\left(e_{3h}\xi_{3h}-\frac{1}{r_{3h}}\dot{\theta}_{3h}\right)-\eta_{3h}e_{3h}^2+\frac{1}{2}\varepsilon_{3h}^2+\frac{1}{2}\rho_h{}^2w_{1h}^2+\frac{1}{2}\rho_h{}^2w_{2h}^2+\frac{1}{2}\rho_h{}^2w_{3h}^2\end{aligned}\tag{38}$$

Define the adaptative updating law as:

$$\begin{cases}\dot{\theta}_{1v}=r_{1v}e_{1v}\xi_{1v}-2k_{1v}\theta_{1v}\\\dot{\theta}_{2v}=r_{2v}e_{2v}\xi_{2v}-2k_{2v}\theta_{2v}\\\dot{\theta}_{3v}=r_{3v}e_{3v}\xi_{3v}-2k_{3v}\theta_{3v}\end{cases}\tag{39a}$$

$$\begin{cases}\dot{\theta}_{1h}=r_{1h}e_{1h}\xi_{1h}-2k_{1h}\theta_{1h}\\\dot{\theta}_{2h}=r_{2h}e_{2h}\xi_{2h}-2k_{2h}\theta_{2h}\\\dot{\theta}_{3h}=r_{3h}e_{3h}\xi_{3h}-2k_{3h}\theta_{3h}\end{cases}\tag{39b}$$

where: ($k_{1v}, k_{2v}, k_{3v}, k_{1h}, k_{2h}$ and k_{3h})$>\ 0$.

Substituting (39a), (39b) into (38) results in:

$$
\begin{aligned}
\Gamma \leq & -\eta_{1v}e_{1v}^2 - \eta_{2v}e_{2v}^2 - \eta_{3v}e_{3v}^2 + \frac{2k_{1v}}{\beta_{1v}r_{1v}}(\theta_{1v}^* - \theta_{1v})^T\theta_{1v} + \frac{2k_{2v}}{\beta_{2v}r_{2v}}(\theta_{2v}^* - \theta_{2v})^T\theta_{2v} \\
& + \frac{2k_{3v}}{\beta_{3v}r_{3v}}(\theta_{3v}^* - \theta_{3v})^T\theta_{3v} + \frac{1}{2}\varepsilon_{1v}^2 + \frac{1}{2}\varepsilon_{2v}^2 + \frac{1}{2}\varepsilon_{3v}^2 + \frac{1}{2}{\rho_v}^2 w_{1v}^2 + \frac{1}{2}{\rho_v}^2 w_{2v}^2 + \frac{1}{2}{\rho_v}^2 w_{3v}^2 \\
& - \eta_{1h}e_{1h}^2 - \eta_{2h}e_{2h}^2 - \eta_{3h}e_{3h}^2 + \frac{2k_{1h}}{\beta_{1h}r_{1h}}(\theta_{1h}^* - \theta_{1h})^T\theta_{1h} + \frac{2k_{2h}}{\beta_{2h}r_{2h}}(\theta_{2h}^* - \theta_{2h})^T\theta_{2h} \\
& + \frac{2k_{3h}}{\beta_{3h}r_{3h}}(\theta_{3h}^* - \theta_{3h})^T\theta_{3h} + \frac{1}{2}\varepsilon_{1h}^2 + \frac{1}{2}\varepsilon_{2h}^2 + \frac{1}{2}\varepsilon_{3h}^2 + \frac{1}{2}{\rho_h}^2 w_{1h}^2 + \frac{1}{2}{\rho_h}^2 w_{2h}^2 + \frac{1}{2}{\rho_h}^2 w_{3h}^2 \\
& + \frac{k_{3h}}{\beta_{3h}r_{3h}}(2\theta_{3h}^{*T}\theta_{3h} - 2\theta_{3h}^T\theta_{3h}) + \frac{1}{2}\varepsilon_{3h}^2 + \frac{1}{2}{\rho_h}^2 w_{3h}^2 \\
& \leq -\eta_{2v}e_{2v}^2 - \eta_{1v}e_{1v}^2 - \eta_{3v}e_{3v}^2 + \frac{k_{1v}}{\beta_{1v}r_{1v}}(\theta_{1v}^{*T}\theta_{1v}^* - \theta_{1v}^T\theta_{1v}) + \frac{1}{2}\varepsilon_{1v}^2 + \frac{1}{2}{\rho_v}^2 w_{1v}^2 \\
& + \frac{k_{2v}}{\beta_{2v}r_{2v}}(\theta_{2v}^{*T}\theta_{2v}^* - \theta_{2v}^T\theta_{2v}) + \frac{1}{2}\varepsilon_{2v}^2 + \frac{1}{2}{\rho_v}^2 w_{2v}^2 \\
& + \frac{k_{3v}}{\beta_{3v}r_{3v}}(\theta_{3v}^{*T}\theta_{3v}^* - \theta_{3v}^T\theta_{3v}) + \frac{1}{2}\varepsilon_{3v}^2 + \frac{1}{2}{\rho_v}^2 w_{3v}^2 + \frac{k_{1h}}{\beta_{1h}r_{1h}}(\theta_{1h}^{*T}\theta_{1h}^* - \theta_{1h}^T\theta_{1h}) + \frac{1}{2}\varepsilon_{1h}^2 \\
& + \frac{1}{2}{\rho_h}^2 w_{1h}^2 + \frac{k_{2h}}{\beta_{2h}r_{2h}}(\theta_{2h}^{*T}\theta_{2h}^* - \theta_{2h}^T\theta_{2h}) + \frac{1}{2}\varepsilon_{2h}^2 + \frac{1}{2}{\rho_h}^2 w_{2h}^2 + \frac{k_{3h}}{\beta_{3h}r_{3h}}(\theta_{3h}^{*T}\theta_{3h}^* - \theta_{3h}^T\theta_{3h}) \\
& + \frac{1}{2}\varepsilon_{3h}^2 + \frac{1}{2}{\rho_h}^2 w_{3h}^2 - \eta_{1h}e_{1h}^2 - \eta_{2h}e_{2h}^2 - \eta_{3h}e_{3h}^2 \\
& \leq -\eta_{1v}e_{1v}^2 - \eta_{2v}e_{2v}^2 - \eta_{3v}e_{3v}^2 + \frac{k_{1v}}{\beta_{1v}r_{1v}}(\theta_{1v}^{*T}\theta_{1v}^* - \theta_{1v}^T\theta_{1v}) + \frac{k_{2v}}{\beta_{2v}r_{2v}}(\theta_{2v}^{*T}\theta_{2v}^* - \theta_{2v}^T\theta_{2v}) \\
& + \frac{k_{3v}}{\beta_{3v}r_{3v}}(\theta_{3v}^{*T}\theta_{3v}^* - \theta_{3v}^T\theta_{3v}) + \frac{1}{2}\varepsilon_{2v}^2 + \frac{2k_{1v}}{\beta_{1v}r_{1v}}\theta_{1v}^{*T}\theta_{1v}^* + \frac{2k_{2v}}{\beta_{2v}r_{2v}}\theta_{2v}^{*T}\theta_{2v}^* + \frac{2k_{3v}}{\beta_{3v}r_{3v}}\theta_{3v}^{*T}\theta_{3v}^* \\
& + \frac{1}{2}\varepsilon_{1v}^2 + \frac{1}{2}\varepsilon_{3v}^2 + \frac{1}{2}{\rho_v}^2 w_{1v}^2 + \frac{1}{2}{\rho_v}^2 w_{2v}^2 + \frac{1}{2}{\rho_v}^2 w_{3v}^2 - \eta_{1h}e_{1h}^2 - \eta_{3h}e_{3h}^2 \\
& + \frac{k_{1h}}{\beta_{1h}r_{1h}}(\theta_{1h}^{*T}\theta_{1h}^* - \theta_{1h}^T\theta_{1h}) + \frac{1}{2}{\rho_h}^2 w_{1h}^2 + \frac{k_{2h}}{\beta_{2h}r_{2h}}(\theta_{2h}^{*T}\theta_{2h}^* - \theta_{2h}^T\theta_{2h}) + \frac{1}{2}\varepsilon_{2h}^2 - \eta_{2h}e_{2h}^2 \\
& + \frac{1}{2}{\rho_h}^2 w_{2h}^2 + \frac{k_{3h}}{\beta_{3h}r_{3h}}(\theta_{3h}^{*T}\theta_{3h}^* - \theta_{3h}^T\theta_{3h}) + \frac{1}{2}\varepsilon_{3h}^2 + \frac{2k_{1h}}{\beta_{1h}r_{1h}}\theta_{1h}^{*T}\theta_{1h}^* + \frac{2k_{2h}}{\beta_{2h}r_{2h}}\theta_{2h}^{*T}\theta_{2h}^* \\
& + \frac{1}{2}{\rho_h}^2 w_{3h}^2 + \frac{2k_{3h}}{\beta_{3h}r_{3h}}\theta_{3h}^{*T}\theta_{3h}^* + \frac{1}{2}\varepsilon_{1h}^2
\end{aligned}
\tag{40}
$$

since:

$$
\begin{cases}
\tilde{\theta}_{1v}^T\tilde{\theta}_{1v} = (\theta_{1v}^* - \theta_{1v})^T(\theta_{1v}^* - \theta_{1v}) = \theta_{1v}^{*T}\theta_{1v}^* - \\
\quad 2\theta_{1v}^{*T}\theta_{1v} + \theta_{1v}^T\theta_{1v} \leq \ 2\theta_{1v}^{*T}\theta_{1v}^* + 2\,\theta_{1v}^T\theta_{1v} \\
\tilde{\theta}_{2v}^T\tilde{\theta}_{2v} = (\theta_{2v}^* - \theta_{2v})^T(\theta_{2v}^* - \theta_{2v}) = \theta_{2v}^{*T}\theta_{2v}^* - \\
\quad 2\theta_{2v}^{*T}\theta_{2v} + \theta_{2v}^T\theta_{2v} \leq \ 2\theta_{2v}^{*T}\theta_{2v}^* + 2\,\theta_{2v}^T\theta_{2v} \\
\tilde{\theta}_{3v}^T\tilde{\theta}_{3v} = (\theta_{3v}^* - \theta_{3v})^T(\theta_{3v}^* - \theta_{3v}) = \theta_{3v}^{*T}\theta_{3v}^* - \\
\quad 2\theta_{3v}^{*T}\theta_{3v} + \theta_{3v}^T\theta_{3v} \ \leq \ 2\theta_{3v}^{*T}\theta_{3v}^* + 2\,\theta_{3v}^T\theta_{3v}
\end{cases}
$$

$$
\begin{cases}
\tilde{\theta}_{1h}^T\tilde{\theta}_{1h} = (\theta_{1h}^* - \theta_{1h})^T(\theta_{1h}^* - \theta_{1h}) = \theta_{1h}^{*T}\theta_{1h}^* - \\
\quad 2\theta_{1h}^{*T}\theta_{1h} + \theta_{1h}^T\theta_{1h} \leq \ 2\theta_{1h}^{*T}\theta_{1h}^* + 2\,\theta_{1h}^T\theta_{1h} \\
\tilde{\theta}_{2h}^T\tilde{\theta}_{2h} = (\theta_{2h}^* - \theta_{2h})^T(\theta_{2h}^* - \theta_{2h}) = \theta_{2h}^{*T}\theta_{2h}^* - \\
\quad 2\theta_{2h}^{*T}\theta_{2h} + \theta_{2h}^T\theta_{2h} \leq \ 2\theta_{2h}^{*T}\theta_{2h}^* + 2\,\theta_{2h}^T\theta_{2h} \\
\tilde{\theta}_{3h}^T\tilde{\theta}_{3h} = (\theta_{3h}^* - \theta_{3h})^T(\theta_{3h}^* - \theta_{3h}) = \theta_{3h}^{*T}\theta_{3h}^* - \\
\quad 2\theta_{3h}^{*T}\theta_{3h} + \theta_{3h}^T\theta_{3h} \leq \ 2\theta_{3h}^{*T}\theta_{3h}^* + 2\,\theta_{3h}^T\theta_{3h}
\end{cases}
\tag{41}
$$

and:

$$\begin{cases} -\frac{1}{2}\tilde{\theta}_{1v}^{T}\tilde{\theta}_{1v} \geq -\theta_{1v}^{*T}\theta_{1v}^{*} - \theta_{1v}^{T}\theta_{1v} \\ -\frac{1}{2}\tilde{\theta}_{2v}^{T}\tilde{\theta}_{2v} \geq -\theta_{2v}^{*T}\theta_{2v}^{*} - \theta_{2v}^{T}\theta_{2v} \\ -\frac{1}{2}\tilde{\theta}_{3v}^{T}\tilde{\theta}_{3v} \geq -\theta_{3v}^{*T}\theta_{3v}^{*} - \theta_{3v}^{T}\theta_{3v} \\ -\frac{1}{2}\tilde{\theta}_{1h}^{T}\tilde{\theta}_{1h} \geq -\theta_{1h}^{*T}\theta_{1h}^{*} - \theta_{1h}^{T}\theta_{1h} \\ -\frac{1}{2}\tilde{\theta}_{2h}^{T}\tilde{\theta}_{2h} \geq -\theta_{2h}^{*T}\theta_{2h}^{*} - \theta_{2h}^{T}\theta_{2h} \\ -\frac{1}{2}\tilde{\theta}_{3h}^{T}\tilde{\theta}_{3h} \geq -\theta_{3h}^{*T}\theta_{3h}^{*} - \theta_{3h}^{T}\theta_{3h} \end{cases} \tag{42}$$

Substituting (42) into (40) results in:

$$\begin{aligned} \dot{V} \leq & -\eta_{1v}\frac{2\beta_{1v}}{2\beta_{1v}}e_{1v}^{2} - \eta_{2v}\frac{2\left(\frac{b_{1m}}{I_{1m}}\right)\beta_{2v}}{2\left(\frac{b_1}{I_1}\right)\beta_{2v}}e_{2v}^{2} - \eta_{3v}\frac{2\left(\frac{k_{11m}}{T_{11m}}\right)\beta_{3v}}{2\left(\frac{k_{11}}{T_{11}}\right)\beta_{3v}}e_{3v}^{2} - \frac{k_{1v}}{2\beta_{1v}r_{1v}}\tilde{\theta}_{1v}^{T}\tilde{\theta}_{1v} - \frac{k_{2v}}{2\beta_{2v}r_{2v}}\tilde{\theta}_{2v}^{T}\tilde{\theta}_{2v} \\ & - \frac{k_{3v}}{2\beta_{3v}r_{3v}}\tilde{\theta}_{3v}^{T}\tilde{\theta}_{3v} + \frac{2k_{1v}}{\beta_{1v}r_{1v}}\theta_{1v}^{*T}\theta_{1v}^{*} + \frac{2k_{2v}}{\beta_{2v}r_{2v}}\theta_{2v}^{*T}\theta_{2v}^{*} + \frac{2k_{3v}}{\beta_{3v}r_{3v}}\theta_{3v}^{*T}\theta_{3v}^{*} \\ & + \frac{1}{2}\varepsilon_{1v}^{2} + \frac{1}{2}\varepsilon_{2v}^{2} + \frac{1}{2}\varepsilon_{3v}^{2} + \frac{1}{2}{\rho_v}^{2}w_{1v}^{2} + \frac{1}{2}{\rho_v}^{2}w_{2v}^{2} + \frac{2k_{2h}}{\beta_{2h}r_{2h}}\theta_{2h}^{*T}\theta_{2h}^{*} + \frac{2k_{3h}}{\beta_{3h}r_{3h}}\theta_{3h}^{*T}\theta_{3h}^{*} + \frac{1}{2}\varepsilon_{1h}^{2} \\ & + \frac{1}{2}\varepsilon_{2h}^{2} + \frac{1}{2}\varepsilon_{3h}^{2} + \frac{1}{2}{\rho_h}^{2}w_{1h}^{2} + \frac{1}{2}{\rho_h}^{2}w_{2h}^{2} + \frac{1}{2}{\rho_h}^{2}w_{3h}^{2} \end{aligned} \tag{43}$$

$\{(w_{1v}, w_{2v}, w_{3v}, w_{1h}, w_{2h}, w_{3h})\}$ (disturbances), so:

$$\begin{cases} w_{1v}^{2} \leq c_{1v} \\ w_{2v}^{2} \leq c_{2v} \\ w_{3v}^{2} \leq c_{3v} \end{cases} \quad \text{and} \quad \begin{cases} w_{1h}^{2} \leq c_{1h} \\ w_{2h}^{2} \leq c_{2h} \\ w_{3h}^{2} \leq c_{3h} \end{cases}$$

Define:

$$c = \frac{1}{2}{\rho_v}^{2}c_{1v}^{2} + \frac{1}{2}{\rho_v}^{2}c_{2v}^{2} + \frac{1}{2}{\rho_v}^{2}c_{3v}^{2} + \frac{1}{2}{\rho_h}^{2}c_{1h}^{2} + \frac{1}{2}{\rho_h}^{2}c_{2h}^{2} + \frac{1}{2}{\rho_h}^{2}c_{3h}^{2} \tag{44}$$

$$\begin{aligned} \dot{V} \leq & -A\left(\frac{1}{2\beta_{1v}}e_{1v}^{2} + \frac{I_1}{2b_1\beta_{2v}}e_{2v}^{2} - \frac{T_{11}}{2k_{11}\beta_{3v}}e_{3v}^{2} + \frac{1}{2\beta_{1v}r_{1v}}\tilde{\theta}_{1v}^{T}\tilde{\theta}_{1v} + \frac{1}{2\beta_{2v}r_{2v}}\tilde{\theta}_{2v}^{T}\tilde{\theta}_{2v} + \frac{1}{2\beta_{3v}r_{3v}}\tilde{\theta}_{3v}^{T}\tilde{\theta}_{3v}\frac{1}{2\beta_{1h}}e_{1h}^{2}\right. \\ & \left. + \frac{I_2}{2b_2\beta_{2h}}e_{2h}^{2} - \frac{T_{22}}{2k_{22}\beta_{3h}}e_{3h}^{2} + \frac{1}{2\beta_{1h}r_{1h}}\tilde{\theta}_{1h}^{T}\tilde{\theta}_{1h} + \frac{1}{2\beta_{2h}r_{2h}}\tilde{\theta}_{2h}^{T}\tilde{\theta}_{2h} + \frac{1}{2\beta_{3h}r_{3h}}\tilde{\theta}_{3h}^{T}\tilde{\theta}_{3h}\right) + B + C \end{aligned} \tag{45}$$

$$\dot{V} \leq -AV + B + C \tag{46}$$

where: *A*, *B*, *C* are positive constants:

$$V(t) \leq V(0) + \frac{B + C}{A}, \quad \forall t \geq 0 \tag{47}$$

From (47), it's proved that all the signals of the designed control system are semi-globally uniformly ultimately bounded.

V. Experimental Results

The experimental part is illustrated in Fig. 8 and Fig. 9, the developed control strategy has proven to be effective for many desirable signals that include various operating areas. The tracking responses are presented in Figs. 4 to Figs. 7 and Figs. 10 to Figs. 12.

V.1. Experience 1: Sine Wave Tracking

Figs. 4 and Figs. 5, present the experimental results illustrate the tracking responses of the TRMS, using a sinusoidal input signal for the subsystems where the horizontal is presented by the angle *(ϕ)* and the vertical is presented by the angle *(ψ)*.

The results of horizontal and vertical system are demonstrated in Figs. 4(a) and (b), prove the robustness of the control strategists used in our work whose trajectory following problem has been solved. The control input voltages for the horizontal and vertical DC motors shown in Figs. 4(c) and (d), show their limits within the allowable range.

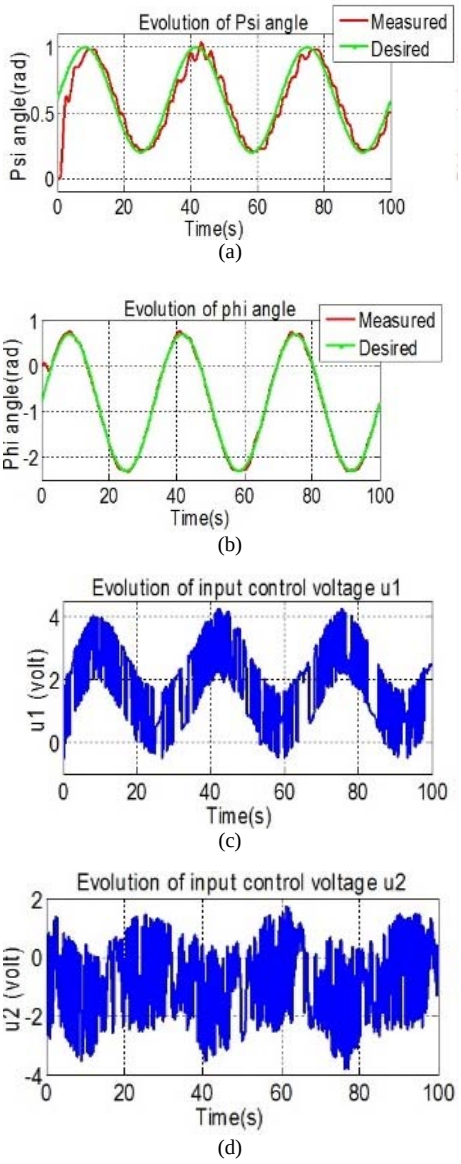

Figs. 4. Results for sine wave tracking

V.2. Experience 2: Triangle Wave Tracking

Figs. 6 and Figs. 7 show the feasibility and efficiency of experimentally proposed control with desired triangular trajectories. The performance of the TRMS controlled in trajectory tracking is confirmed in these figures. It is seen that the monitoring effectiveness is proven in the practical implementation, as shown in Figs. 6(a) and (b). The control input voltages for the horizontal and vertical DC motors shown in Figs. 6(c) and (d), are limited in the permit interval.

V.3. Experience 4: Sine and Triangular Wave Tracking with Different Frequencies

Moreover, to what was previously explained, to determine the effectiveness of the proposed control method to address and reduce the cross effects between the two subsystems, Figs. 5(a) and (b) and Figs. 7(a) and (b) respectively shows the path performed by TRMS with respect to the sinusoidal and triangular reference path respectively with different experimental frequencies.

Small overshoots may be observed in the experimental curves at horizontal and vertical angles as shown in Figs. 7(a) and (b), due to the discontinuous nature of triangular signal.

V.4. Experience 5: Robustness Test

In order to demonstrate the ability of the proposed control method and observe the effect and effectiveness, TRMS was attacked experimentally during operation by external turbulence represented by the wind in the first experiment Fig. 8, and by giving few vibrations in the second experiment, during the horizontal movement and vertical.

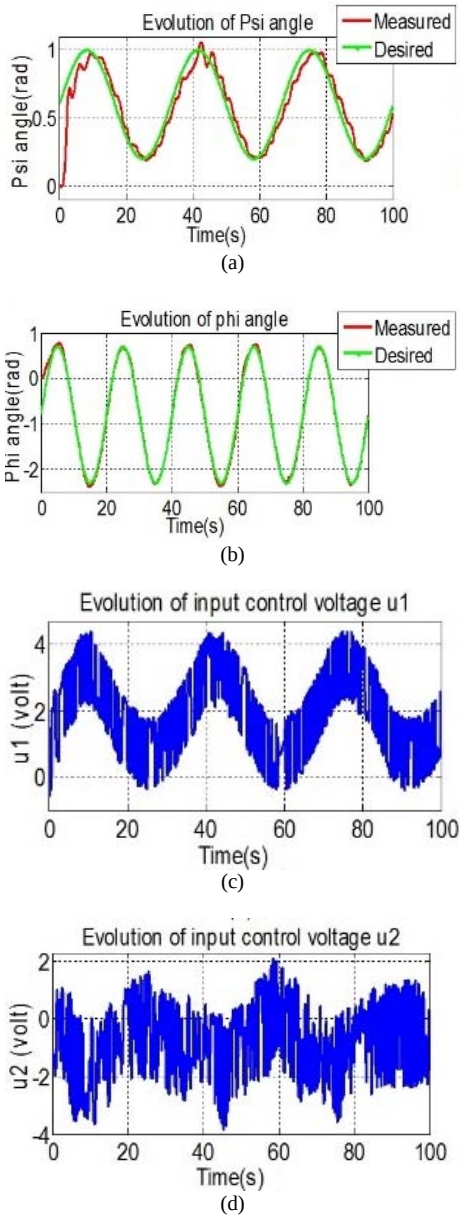

Figs. 5. Results for sine wave tracking with different frequencies

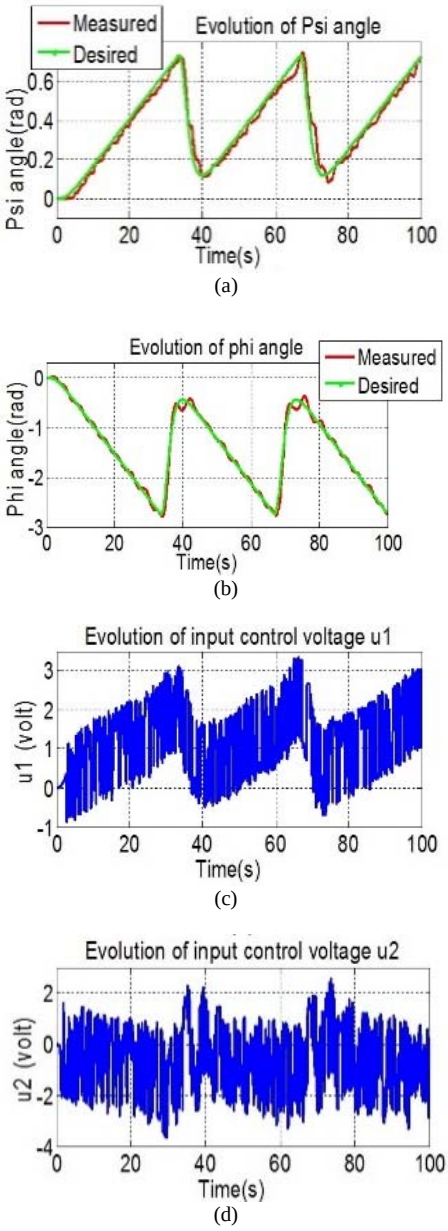

Figs. 6. Results for triangle wave tracking

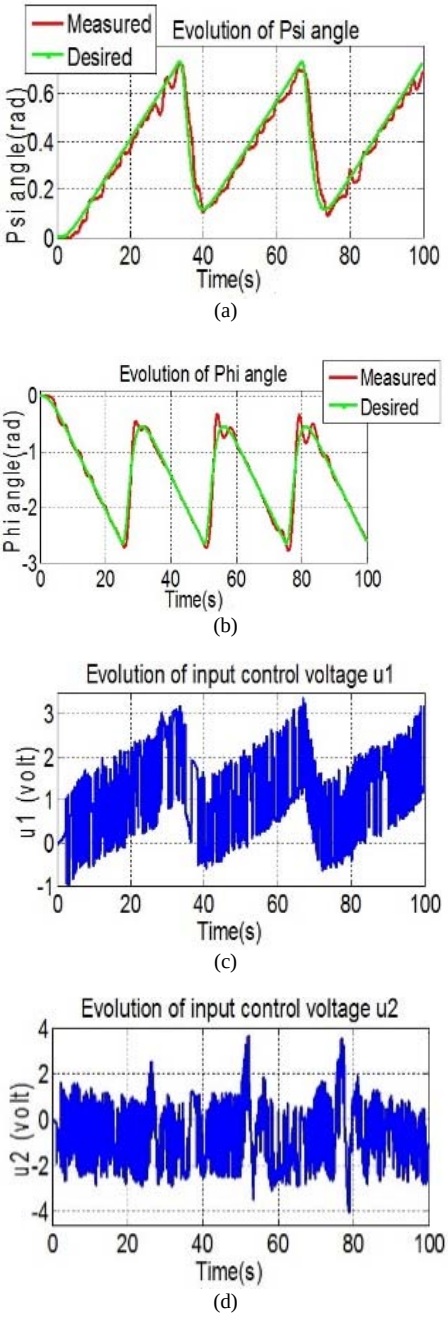

Figs. 7. Results for triangle wave tracking with different frequencies

V.5. Wind Effects Test

By using two different inputs signals, the results of this experiment are shown in Figs. 10 and Figs. 11. With great accuracy, the absolute position of TRMS in the horizontal and vertical plane in the presence of gusts of wind at 3.8 m/s is proved.

It means that the proposed control method makes it possible to obtain good resistance to external disturbances, which indicates good toughness, as shown in Figs. 10(a) and (b) and Figs. 11(a) and (b).

The control input signals are limited within the allowed range, as shown in the Figs. 10(c) and (d) and Figs. 11(c) and (d).

Fig. 8. Workbench (Presence of wind effects)

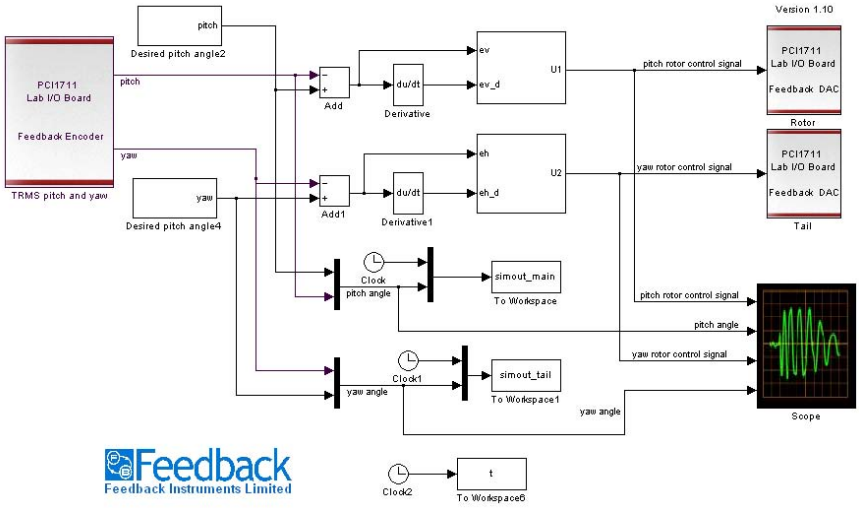

Fig. 9. MATLAB/Simulink block (Wind disturbance rejection)

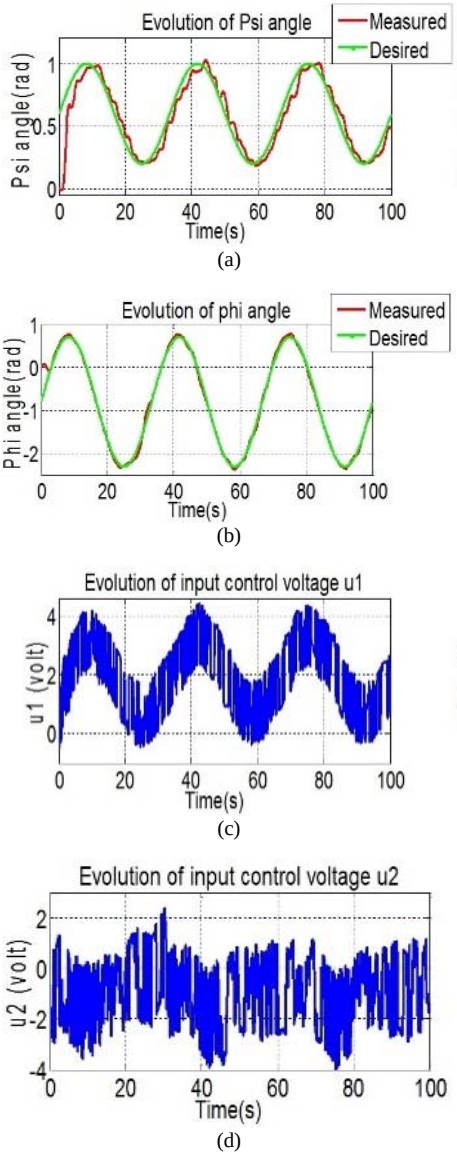

Figs. 10. Sine wave tracking results (wind effects)

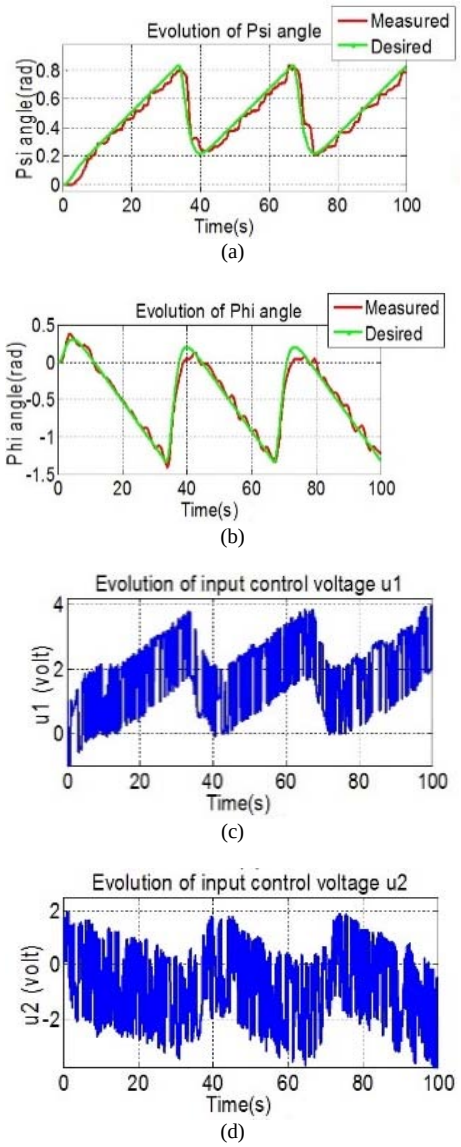

Figs. 11. Triangle wave tracking results (wind effects)

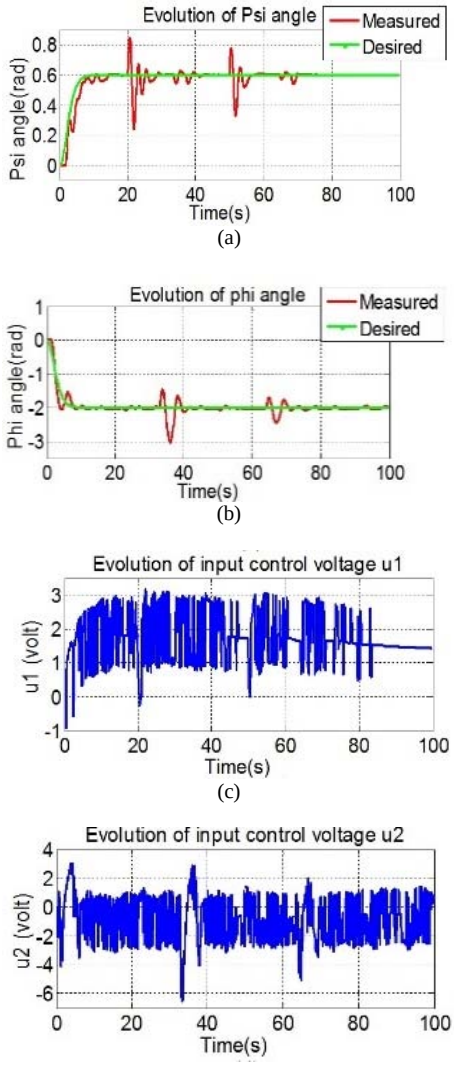

Figs. 12. Results for Step responses of the TRMS (External disturbance)

V.5.1. External Disturbance Test

Another method was conducted experimentally with the aim of testing the effectiveness of our proposed control strategy, by a simple push of the hand on the TRMS during its movement. The TRMS trying to the resist and maintain his instantaneous position, with a rapid reaction. The experimental results are shown in Figs. 12(a) and (b), it's noted that TRMS with the proposed controller is robust in presence of external disturbances.

VI. Conclusion

In this paper, an adaptive fuzzy robust control approach based on backstepping design is proposed for Twin Rotor Multi Input Multi Output system. The type 2 fuzzy systems are used to approximate unknown nonlinear functions (interconnections between the chaotic subsystems and derivative of the virtual control).

The Lyapunov method was used to demonstrate the stability of the system in a closed loop, with reinforcement of adaptive laws in order to increase durability in the presence of gusts of wind, external disturbances and uncertainties. The performance of the proposed control was experimented with using different desired signals, and it was found that the TRMS system can track the reference paths with good performance. The proposed scheme can guarantee that all the close loop signals are bounded and that the outputs of the system converge to a small neighborhood of the desired trajectory. Simulations results show that the proposed method is very effective and robust against system uncertainty. The obtained experimental results demonstrated the good tracking performance of the proposed control strategy despite the external influences.

Finally, this study can be extended for future work if other control schemes are included. One may use the following modern control methodologies for this purpose such as active disturbance control, super-twisting sliding mode control, projection adaptive sliding mode control, etc.

References

[1] L. M. Belmonte, R. Morales, A. Fernández-Caballero and J. A. Somolinos, "A Tandem Active Disturbance Rejection Control for a Laboratory Helicopter with Variable-Speed Rotors," in *IEEE Transactions on Industrial Electronics*, vol. 63, no. 10, pp. 6395-6406, Oct. 2016.
doi: 10.1109/TIE.2016.2587238

[2] Rahideh A, Shaheed MH. "Mathematical dynamic modelling of a twin-rotor multiple input-multiple output system". *Proceedings of the Institution of Mechanical Engineers, Part I: Journal of Systems and Control Engineering*. 2007;221(1):89-101.
doi: 10.1243/09596518JSCE292

[3] Ying Xin, Zhi-Chang Qin, Jian-Qiao Sun, "Input-output tracking control of a 2-DOF laboratory helicopter with improved algebraic differential estimation", *Mechanical Systems and Signal Processing*, Volume 116, 2019, Pages 843-857.
doi:https://doi.org/10.1016/j.ymssp.2018.07.027

[4] Ignatyev, V., Kovalev, A., Spiridonov, O., Kureychik, V., Soloviev, V., Ignatyeva, A., A Method of Optimizing the Rule Base in the Sugeno Fuzzy Inference System Using Fuzzy Cluster Analysis, (2020) *International Review of Electrical Engineering (IREE)*, 15 (4), pp. 316-327.
doi:https://doi.org/10.15866/iree.v15i4.16545

[5] J. -G. Juang, M. -T. Huang and W. -K. Liu, "PID Control Using Presearched Genetic Algorithms for a MIMO System," in *IEEE Transactions on Systems, Man, and Cybernetics, Part C (Applications and Reviews)*, vol. 38, no. 5, pp. 716-727, Sept. 2008.
doi: 10.1109/TSMCC.2008.923890

[6] A. Haruna, Z. Mohamed, M.Ö. Efe, M.A.M. Basri, "Improved integral backstepping control of variable speed motion systems with application to a laboratory helicopter", *ISA Transactions*, Volume 97, 2020, Pages 1-13.
doi:https://doi.org/10.1016/j.isatra.2019.07.016

[7] Mohammed Zinelaabidine Ghellab, Samir Zeghlache, Ali Djerioui, Loutfi Benyettou, "Experimental validation of adaptive RBFNN global fast dynamic terminal sliding mode control for twin rotor MIMO system against wind effects", *Measurement, Volume* 168, 2021, 108472.
doi:https://doi.org/10.1016/j.measurement.2020.108472

[8] C. -W. Tao, J. -S. Taur, Y. -H. Chang and C. -W. Chang, "A Novel Fuzzy-Sliding and Fuzzy-Integral-Sliding Controller for the Twin-Rotor Multi-Input–Multi-Output System," in *IEEE*

Transactions on Fuzzy Systems, vol. 18, no. 5, pp. 893-905, Oct. 2010.
doi: 10.1109/TFUZZ.2010.2051447

[9] M. Khamar, M. Edrisi, "Designing a backstepping sliding mode controller for an assistant human knee exoskeleton based on nonlinear disturbance observer", *Mechatronics*, Volume 54, 2018, Pages 121-132.
doi:https://doi.org/10.1016/j.mechatronics.2018.07.010

[10] Abdillah, M., Nugroho, T., Pertiwi, N., Multi-Objective Interval Type 2 Fuzzy Sine Cosine Algorithm for Solving Optimal Power Flow Problem, (2021) *International Review of Electrical Engineering (IREE)*, 16 (2), pp. 118-126.
doi:https://doi.org/10.15866/iree.v16i2.18188

[11] S. K. Valluru, R. Kumar and R. Kumar, "Design of Precise FLC for Trajectory Tracking and Stabilization of Twin Rotor MIMO System," 2019 IEEE 6th *International Conference on Engineering Technologies and Applied Sciences (ICETAS)*, Kuala Lumpur, Malaysia, 2019, pp. 1-6.
doi:https://doi.org/10.1109/ICETAS48360.2019.9117570

[12] K. Kalyani and S. Kanagalakshmi, "Control of Trms using Adaptive Neuro Fuzzy Inference System (ANFIS)," 2020 *International Conference on System, Computation, Automation and Networking (ICSCAN)*, Pondicherry, India, 2020, pp. 1-5.
doi:https://doi.org/10.1109/ICSCAN49426.2020.9262417

[13] Batayneh, W., Aburmaileh, Y., Bataineh, A., Experimental Implementation of Tracking Error Elimination for Omnidirectional Wheelchair Using PD-Fuzzy-P Controller, (2021) *International Review of Automatic Control (IREACO)*, 14 (2), pp. 102-112.
doi:https://doi.org/10.15866/ireaco.v14i2.20654

[14] C. Mishra, S. K. Swain, S. Kumar Mishra and S. K. Yadav, "Fractional Order Sliding Mode Controller for the Twin Rotor MIMO System," 2019 *International Conference on Intelligent Computing and Control Systems (ICCS)*, Madurai, India, 2019, pp. 662-667.
doi:https://doi.org/10.1109/ICCS45141.2019.9065331

[15] G. Rohith, Fractional power rate reaching law for augmented sliding mode performance, *Journal of the Franklin Institute*, Volume 358, Issue 1, 2021, Pages 856-876.
doi:https://doi.org/10.1016/j.jfranklin.2020.11.018

[16] Rached, B., Elharoussi, M., Abdelmounim, E., New Dynamic Fuzzy High Gain Observer Combined with a Nonlinear Control Approach for Performance Enhancement in WECS Based on DFIG: Design and DSP Implementation, (2021) *International Review of Automatic Control (IREACO)*, 14 (5), pp. 250-261.
doi:https://doi.org/10.15866/ireaco.v14i5.20669

[17] S. H. Shah, S. G. Khan, J. Iqbal and M. Alharthi, "Modeling and Robust Control of Twin Rotor MIMO System," 2019 *International Conference on Robotics and Automation in Industry (ICRAI)*, Rawalpindi, Pakistan, 2019, pp. 1-5.
https://doi.org/10.1109/ICRAI47710.2019.8967355

[18] *Twin Rotor MIMO System Manual*, Feedback Instruments Ltd., UK, 2006.

[19] Nithya, M., Rashmi, M., Gazebo – Simulink Framework for Trajectory Tracking in a Multi-Quadcopter Environment, (2022) *International Review of Automatic Control (IREACO)*, 15 (4), pp. 164-175.
doi:https://doi.org/10.15866/ireaco.v15i4.21432

[20] Wan M, Liu Q. Adaptive fuzzy backstepping control for uncertain nonlinear systems with tracking error constraints. *Advances in Mechanical Engineering*. 2019,11(5).
doi:10.1177/1687814019851309

[21] Belkhiri, D., Alaoui, M., Improved Tracking of Optimal Torque by Artificial Neural Network for Wind Energy Systems, (2021) *International Review on Modelling and Simulations (IREMOS)*, 14 (2), pp. 110-117.
doi:https://doi.org/10.15866/iremos.v14i2.19157

[22] Tawfeic, S., Multiplicative and Additive Error Compensation Techniques for Perfect Reference Tracking, (2023) *International Review of Automatic Control (IREACO)*, 16 (1), pp. 10-16.
doi:https://doi.org/10.15866/ireaco.v16i1.22902

Authors' information

[1]LGE, Laboratory of Electrical Engineering, University of M'sila, Algeria.

[2]Department of Electrical Engineering, Faculty of Technology, University of M'sila, Algeria.

[3]LASS, Laboratory of Analysis of Signals and Systems, University of M'sila, Algeria.

[4]LPMRN Laboratory, University Mohammed El Bachir El Ibrahimi of Bordj Bou Arreridj, Algeria.
E-mail: Abdelhalim.kessal@univ-bba.dz

[5]IREENA Laboratory, University of Nantes, Saint-Nazaire, France.

Badreddine Ladjal was born in 1982, in M'Sila, Algeria. He is currently a PhD student in Mechatronic in the Faculty of technology, University Mohamed Boudiaf of M'sila (Algeria). He received his Master in Electromechanics in June, 2015 and His engineer in June 2005 from University Mohamed Boudiaf of M'sila and baccalaureate in sciences from Tamimi High School in M'sila in June, 2000. He is actually a researcher in the LGE, Laboratory of Electrical Engineering, University of M'sila, Algeria. He is co-authored a number of researches and currently working to many research interests include the electrical machine, TRMS, the electromechanically systems.

Fouad Berrabah was born in m'sila, in 1979. He received the B.Sc., M.Sc. and Ph.D. degrees in Electromechanical Engineering from Badji-Mokhtar Annaba University Algeria in 2002, 2008 and 2017 respectively. He is a lecturer senior at the University of M'sila in Algeria. His research interests include electrical machine and drive modeling and analysis, electrical machine and drive control and converters as well as electrical machine and drive fault diagnosis and tolerance.

Samir Zeghlache was born in Sétif, Algeria. He received his Engineer degree in Automatic from M'Sila University, Algeria, in 2006 and the Magister Diploma from Military Polytechnic School, -Bordj el Bahri- Algiers, Algeria, in 2009, all in Electrical Engineering. He received the doctorate degree in electronic from the University of M'Sila, Algeria. In 2011, he joined M'Sila University, Algeria, where he works currently as lecturer. His research interests are nonlinear system control. He is the author and co-author of numerous articles on the fault-tolerant control of vertical flight devices. In 2017, he created the first doctoral school in automatic in the history of the University of M'Sila.

Ali Djerioui received the Engineer degree in electrical engineering from the University of M'Sila, Algeria. He received M.Sc. degree in electrical engineering from the Polytechnic Military Academy and Ph.D. degree in electronic instrumentation systems from University of Sciences and Technology Houari Boumediene, Algiers, Algeria, in 2011 and 2016, respectively. He received the HdR in 2018 from the University of M'Sila, Algeria. He is currently an Associate Professor with the Department of electronics, M'Sila University, Algeria. His current research interests include power electronics, control, microgrids and power quality.

Abdelhalim Kessal was born in Bordj Bou Arreridj, Algeria in 1975. He is currently full professor at the Department of Electrical Engineering and head of the Electro-Energetic Converters Research Team at the Laboratory of Materials Physics, Radiation and Nanostructures, Bordj Bou Arreridj University, Algeria. In 1997, He received the degree of engineer in electrical engineering from university of Setif, Algeria. Next, he received the degree of M.Sc. in electrical engineering and Ph.D. in power electronics from the same university, in 2012. He was once head of the Department Electromechanics and the dean of Sciences and Technology Faculty at Bordj Bou Arreridj University. Presently, he holds the position of Vice Rector. His areas of interest are power electronic systems, renewable energy resources, trans active control and intelligent technologies.

Mabrouk Defdaf received his B.Sc., M.Sc. and Ph.D. degrees in Electromechanical Engineering from Badji-Mokhtar Annaba University Algeria in 2000, 2007 and 2018 respectively. He is a lecturer senior at the University of M'sila in Algeria. His research interests include electrical machine and drive modeling and analysis, electrical machine and drive control and converters as well as electrical machine and drive fault diagnosis and tolerance.

Mohamed Fouad Benkhoris was born in Boussaada, Algeria, on September 17, 1963. He received the engineer degree in electrical engineering from the ENP Algiers, El Harrach, Algeria, in 1986, and the Ph.D. degree in electrical engineering and the HDR from the National Polytechnic Institute of Lorraine, Nancy, France, in 1991 and 2004, respectively. Since 1991, he has been an Assistant Professor with the Department of Electrical Engineering, Polytech Nantes, Nantes, France, where he has been a professor since 2006. He does his research with the Institut de Recherche en ´ Energie ´ Electrique de Nantes Atlantiques, Saint-Nazaire, France. His research interests include dynamical modeling, simulation, and control of electrical drives, and especially multiphase drive, multi-converter systems, and embarked networks.

Praise Worthy Prize

International Review of Automatic Control (I.RE.A.CO.), Vol. 16, N. 2
ISSN 1974-6059 *March 2023*

Processor in the Loop Experimentation of an Integral Backstepping Control Strategy Based Torque Observer for Induction Motor Drive

Mohammed El Haissouf, Mustapha El Haroussi, Abdellfattah Ba-Razzouk

Abstract – *This paper proposes the design and the implementation, using Processor In the Loop "PIL" approach, of a Backstepping control strategy for induction motor "IM". The proposed control strategy is based on a state-space model of IM in the rotor flux reference frame and uses an integrator to enhance the accuracy of the controlled system. This work also presents the design of a load torque observer using Luenberger method. The load torque estimation is indeed required for accurate determination of the control law. Code generation and validation of the proposed control algorithm use Matlab/Simulink R2017b and Code Composer Studio CCSv7 software platform. In addition, LAUNCHXL-F28069M development board based on TMS320F28069 DSP from Texas instruments is used as target for implementation. It should be noted that, in this work, parameters of controller and observer are calculated according to the desired performances. Obtained results prove that these requirements are met.*

Keywords: *Integral Backstepping Control, Induction Motor, Processor in the Loop, Space Vector Modulation, Load Torque Luenberger Observer*

Nomenclature

$\Omega, \widetilde{\Omega}$	Rotor speed and estimated rotor speed [rad/s]
p	Pole pairs
$T_M, T_L, \tilde{T}_L$	Electromagnetic torque, load torques, and estimated load torque [N m]
v_{sd}, v_{sq}	Direct and quadrature components of stator voltage [V]
i_{sd}, i_{sq}	Direct and quadrature components of stator current [A]
$\varphi_{rd}, \varphi_{rq}$	Direct and quadrature components of rotor flux [Wb]
$i_{\varphi d}, i_{\varphi q}$	Direct and quadrature components of rotor flux reduced in current form [A]
$\rho s, \omega s$	Frame angle and speed relative to the stator [rad] and [rad/s]
$\rho r, \omega r$	Frame angle and speed relative to the rotor [rad] and [rad/s]
x_1, x_2, x_3, x_4	New notation for state space variables of induction motor oriented model
X_1, X_2	Vector variables
X_{1ref}, X_{2ref}	Vector references
E_1, E_2	Vector errors
U	Vector input
Rs, Rr	Stator and rotor resistances [Ω]
Ls, Lr, Msr	Stator, rotor and mutual inductances [H]
J, f	Inertia and friction coefficient [kg m^2] and [Nm/rad s^{-1}]
Ts, Tr	Stator and rotor time-constants [s]
Tc	Current time-constant [s]
σ	Dispersion coefficient of induction motor
f_{PWM}, f_{SMP}	Modulation and sampling frequency
PIL	Processor In the Loop
CCS	Code Composer Studio
PWM	Pulse Width Modulation
SVM	Space Vector Modulation
SPWM	Sinusoidal Pulse Width Modulation
DTC	Direct Torque Control
MIMO	Multi-Inputs Multi-Outputs
s	Laplace variable
$\mathcal{L}$	Laplace transform
IDE	Integrated Development Environment
DSP	Digital Signal Processor

I. Introduction

Induction motor is a nonlinear system, so the classical control strategies cannot be used directly [1], [2], because they require special operations such as linearization, decoupling, commutation table, etc… [3], [4]. As a result, traditional control strategies have complex algorithms and do not give always a good results over a wide operating range [5], [6]. On one hand, scalar control of induction motor is a simple strategy but it cannot give good dynamic performances since it is based on steady-state model. From this point of view, vector controls of induction motor such as Field Oriented Control ensure better performances but need linearization-decoupling algorithm as well as PI controllers. On the other hand, Direct Torque Control gives good dynamic performances but induces high torque and rotor flux ripples and high total harmonic

 https://doi.org/10.15866/ireaco.v16i2.23063

distortion of stator currents except for SVM based DTC, which needs complex design and approximations. In addition, DTC in general needs an additional controller for rotor speed. Backstepping is an advanced control strategy for dynamic systems, based on Lyapunov stability theory [7]-[9]. It is designed in several steps, depending on the order of the system, starting from controlled variable to control variable. This concept is easily adapted to the nonlinear systems in strict feedback form, but also to other forms of nonlinear systems by applying appropriate variable changes. For each step, an elementary control law is expressed and then the main control law is the association of all these elementary controls.

Figure 1 illustrates the principle the Backstepping control strategy where each control step generates the reference to the next step. In fact, Backstepping control strategy has several advantages: it can be applied easily to nonlinear MIMO systems with no need for other mathematic operations and it can include observed disturbances and integrators in the control law in order to enhance control performances. In addition, Backstepping is a simplified control strategy since it is designed by steps of first order elementary systems with possibility of separating their dynamics.

This technique reduces control law complexity. Several researches have been interested in the Backstepping control of induction motors and different solutions have been proposed such as sensorless Backstepping control [10], PI based control [11], using fuzzy logic [12], variable gain Backstepping [13], combination with other control strategies such as sliding modes approach [14], [15], on-line identification motor parameters such as time constants [16]; as well as other techniques. In general, published studies on Backstepping control strategies for induction motor have weaknesses sometimes in term of controller and observer parameters calculation taking into account system behaviour and requirements, or in term of sampling frequency effect on ripples and distortion. In addition, the load torque effect is neglected in many researches especially when integrators are introduced.

This paper proposes a simple state-space vector model of the induction motor expressed in the rotor flux reference frame, which is suitable for a direct and easy use of the Backstepping control strategy. Then the control law is determined and integrators added to Backstepping control scheme for more accuracy and robustness against parameters variations [9]. Two integrators are added for each step of the controller design, so four integrators are needed for induction motor controller.

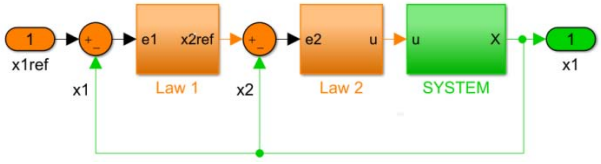

Fig. 1. Backstepping control principle

Since the studied control law requires the knowledge of rotor flux and load torque, this work proposes the design of a flux estimator and a load torque observer according to Luenberger method [17]. For rotor flux determination, a simple estimator based on motor equations is used. This solution needs only stator currents unlike rotor flux observer, which requires stator voltage measurement under a different sampling frequency. In fact, a very higher frequency is needed. The controller design proposed in this work is based on a cascaded approach with dynamic separation. Hence, first step dynamic is sufficiently slower than the second step dynamic and so on. The last step dynamic is the fastest one. This approach allows simplifying the control law expression relative to each step, which is not affected by the previous step control law. Proposed control strategy, by combining Backstepping with integrators and torque observer for induction motor control, is validated first on Matlab/Simulink, and then by Processor In the Loop technique [3]. PIL validation platform is based on Matlab/Simulink R2017b combined with Texas Instruments IDE: Code Composer Studio CCSv7 and the development board LAUNCHXL-F28069M using the DSP TMS320F28069.

This work is organized as follows. Section II presents the induction motor state-space representation in rotor flux reference frame and gives a vector strict feedback form of the induction motor state-space equation. The obtained compact model expressed in this particular reference frame is very important to perform a consistent controller design and clearly express control law. Section III explains the theoretical principle of a new Backstepping controller design based on the induction motor vector representation and integrating integrators for more robustness. In this section, dynamic separation is ensured by choosing distant response times and then controller parameters are calculated to guarantee the required response time for each step. Section IV presents the design of rotor flux estimator, load torque observer and the compensation filter. Rotor flux estimator is an important part of this design because rotor flux is the second variable that should be controlled. Load torque observer improves disturbance rejection when combined with integrators. Compensating filter suppresses speed overshoot. Section V discusses the results of PIL experimentation based on the DSP implementation and evaluates the performance of the proposed control strategy. In this section, the sampling and the carrier frequency effect on waveforms quality are also examined.

PIL experimentation is performed under two sampling frequencies, i.e. 2 kHz and 10 kHz , in order to compare first, torque ripples, and secondly stator currents distortions for these frequencies.

II. Induction Motor Modelling for Control Design

In the two-phase reference frame, electromagnetic

state-space representation of induction motor contains four variables.

For this study, the variables are the stator currents and two virtual currents replacing rotor flux components in reduced form [1]. Electromagnetic state-space equation is given by Equation (1) and completed by mechanical Equation (2):

$$\frac{d}{dt}\begin{bmatrix} i_{sd} \\ i_{sq} \\ i_{\varphi d} \\ i_{\varphi q} \end{bmatrix} = \begin{bmatrix} -\frac{1}{Tc} & \frac{d\rho s}{dt} & \frac{1-\sigma}{\sigma Tr} & \frac{1-\sigma}{\sigma} p\Omega \\ -\frac{d\rho s}{dt} & -\frac{1}{Tc} & -\frac{1-\sigma}{\sigma} p\Omega & \frac{1-\sigma}{\sigma Tr} \\ \frac{1}{Tr} & 0 & -\frac{1}{Tr} & \frac{d\rho r}{dt} \\ 0 & \frac{1}{Tr} & -\frac{d\rho r}{dt} & -\frac{1}{Tr} \end{bmatrix} \begin{bmatrix} i_{sd} \\ i_{sq} \\ i_{\varphi d} \\ i_{\varphi q} \end{bmatrix} + \frac{1}{\sigma Ls} \begin{bmatrix} 1 & 0 \\ 0 & 1 \\ 0 & 0 \\ 0 & 0 \end{bmatrix} \begin{bmatrix} v_{sd} \\ v_{sq} \end{bmatrix} \quad (1)$$

$$\frac{d\Omega}{dt} = -\frac{f}{J}\Omega + \frac{T_M}{J} - \frac{T_L}{J} \quad (2)$$

with:

$$T_M = \frac{3}{2} p(1-\sigma) Ls \left(i_{\varphi d} i_{sq} - i_{\varphi q} i_{sd} \right) \quad (3)$$

$$i_{\varphi d} = \frac{\varphi_{rd}}{Msr}; \quad i_{\varphi q} = \frac{\varphi_{rq}}{Msr} \quad (4)$$

$$\frac{1}{Tc} = \left(\frac{1}{\sigma Ts} + \frac{1-\sigma}{\sigma Tr} \right); \ \sigma = 1 - \frac{Msr^2}{LsLr} \quad (5)$$

The same frame is used for all the variables, so the relation between frame velocities and rotor velocity is given in (6):

$$\frac{d\rho s}{dt} = p\Omega + \frac{d\rho r}{dt} \quad (6)$$

II.1. Induction Motor Model in Rotor Flux Frame

Backstepping strategy can be applied to induction motor in the static frame but the equations will be very complex in this case, as well as the resulting control law.

This work proposes to apply Backstepping strategy in the rotor flux reference frame, so that rotor flux is defined by a single state variable instead of two [18]. In the new reference frame, electromagnetic state-space representation is given by Equation (7), completed by the mechanical Equation (8):

$$\frac{d}{dt}\begin{bmatrix} i_{sd} \\ i_{sq} \\ i_{\varphi d} \end{bmatrix} = \begin{bmatrix} -\frac{1}{Tc} & \frac{d\rho s}{dt} & \frac{1-\sigma}{\sigma Tr} \\ -\frac{d\rho s}{dt} & -\frac{1}{Tc} & -\frac{1-\sigma}{\sigma} p\Omega \\ \frac{1}{Tr} & 0 & -\frac{1}{Tr} \end{bmatrix} \begin{bmatrix} i_{sd} \\ i_{sq} \\ i_{\varphi d} \end{bmatrix} + \frac{1}{\sigma Ls} \begin{bmatrix} 1 & 0 \\ 0 & 1 \\ 0 & 0 \end{bmatrix} \begin{bmatrix} v_{sd} \\ v_{sq} \end{bmatrix} \quad (7)$$

which is a tri-dimensional equation:

$$\frac{d\Omega}{dt} = -\frac{f}{J}\Omega + \frac{T_M}{J} - \frac{T_L}{J} \quad (8)$$

with:

$$T_M = \frac{3}{2} p(1-\sigma) Ls i_{\varphi d} i_{sq} \quad (9)$$

Induction motor model becomes simpler with only four variables instead of five, and a shorter expression of the electromagnetic torque.

II.2. Variables Definition

Induction motor representation in rotor flux reference frame has four state-space variables. Motor speed and rotor flux are the main variables and stator currents are intermediate variables [18], [19]:

$$\frac{d}{dt}\Omega = -\frac{f}{J}\Omega - \frac{T_L}{J} + \frac{3p}{2J}(1-\sigma) Ls i_{\varphi d} i_{sq} \quad (10)$$

$$\frac{d}{dt} i_{\varphi d} = -\frac{1}{Tr} i_{\varphi d} + \frac{1}{Tr} i_{sd} \quad (11)$$

$$\frac{d}{dt} i_{sd} = -\frac{1}{Tc} i_{sd} + \omega_s i_{sq} + \frac{1-\sigma}{\sigma Tr} i_{\varphi d} + \frac{1}{\sigma Ls} v_{sd} \quad (12)$$

$$\frac{d}{dt} i_{sq} = -\frac{1}{Tc} i_{sq} - \omega_s i_{sd} - \frac{1-\sigma}{\sigma} p\Omega i_{\varphi d} + \frac{1}{\sigma Ls} v_{sq} \quad (13)$$

Rotor flux references frame velocity relative to the stator is not a separate variable, because it depends on the other variables. Therefore, there is no need to define a new variable or even express it by using the other variables:

$$\omega_s = p\Omega + \frac{1}{Tr} \frac{i_{sq}}{i_{\varphi d}} \quad (14)$$

For simplicity, this paper proposes the following notation change for variables:

$$\begin{bmatrix} x_1 \\ x_2 \\ x_3 \\ x_4 \end{bmatrix} = \begin{bmatrix} \Omega \\ i_{sd} \\ i_{\varphi d} \\ i_{sq} \end{bmatrix} \quad (15)$$

The resulting state-space representation using this new notation is given by four equations (16), (17), (18) and (19):

$$\dot{x}_1 = -\frac{f}{J}x_1 - \frac{T_L}{J} + \frac{3p}{2J}(1-\sigma)Lsx_3x_2 \quad (16)$$

$$\dot{x}_2 = -\frac{1}{Tc}x_2 + \omega_s x_4 + \frac{1-\sigma}{\sigma Tr}x_3 + \frac{1}{\sigma Ls}v_{sd} \quad (17)$$

$$\dot{x}_3 = -\frac{1}{Tr}x_3 + \frac{1}{Tr}x_2 \quad (18)$$

$$\dot{x}_4 = -\frac{1}{Tc}x_4 - \omega_s x_2 - \frac{1-\sigma}{\sigma}px_1x_3 + \frac{1}{\sigma Ls}v_{sq} \quad (19)$$

II.3. Induction Motor Vector Model

In order to simplify the design of Backstepping control for induction motor, this work uses two-dimensional vectors for inputs and state-space variables [20]. State-space model is given by the vector equations (20) and (21):

$$\begin{bmatrix}\dot{x}_1\\ \dot{x}_3\end{bmatrix} = -\begin{bmatrix}\frac{f}{J}x_1 + \frac{T_L}{J}\\ \frac{1}{Tr}x_3\end{bmatrix} + \begin{bmatrix}0 & \frac{3p}{2J}(1-\sigma)Lsx_3\\ \frac{1}{Tr} & 0\end{bmatrix}\begin{bmatrix}x_2\\ x_4\end{bmatrix} \quad (20)$$

$$\begin{bmatrix}\dot{x}_2\\ \dot{x}_4\end{bmatrix} = \begin{bmatrix}-\frac{1}{Tc}x_2 + \omega s x_4 + \frac{1-\sigma}{\sigma Tr}x_3\\ -\omega s x_2 - \frac{1}{Tc}x_4 - \frac{1-\sigma}{\sigma}px_1x_3\end{bmatrix} + \frac{1}{\sigma Ls}\begin{bmatrix}v_{sd}\\ v_{sq}\end{bmatrix} \quad (21)$$

By considering vector representation, this is a strict feedback form system defined by only two equations and controller design can be performed in two steps.

III. Backstepping Control Design of Induction Motor

This work proposes a cascaded Backstepping control design that contains integrators and load torque observer, while rotor flux is obtained by an estimator from the stator currents. Figure 2 represents the control scheme containing mainly a first control block generating the reference signals related to the auxiliary variables, a second control block generating the signals related to the main Backstepping control law, a load torque observer, a flux estimator and the SVM modulator [21], [22]. Vector state-space representation of induction motor can be written compactly according to the Equations (22) and (23) where input and state-space variables are two-dimensional vectors:

$$\dot{X}_1 = F_1(X_1) + G_1(X_1)X_2 \quad (22)$$

$$\dot{X}_2 = F_2(X_1, X_2) + G_2U \quad (23)$$

with:

$$X_1 = \begin{bmatrix}x_1\\ x_3\end{bmatrix};\ X_2 = \begin{bmatrix}x_2\\ x_4\end{bmatrix};\ U = \begin{bmatrix}v_{sd}\\ v_{sq}\end{bmatrix} \quad (24)$$

and:

$$F_1(X_1) = -\begin{bmatrix}\frac{1}{Tm}x_1 + \frac{T_L}{J}\\ \frac{1}{Tr}x_3\end{bmatrix} \quad (25)$$

$$F_2(X_1, X_2) = \begin{bmatrix}-\frac{1}{Tc}x_2 + \omega s x_4 + \frac{1-\sigma}{\sigma Tr}x_3\\ -\omega s x_2 - \frac{1}{Tc}x_4 - \frac{1-\sigma}{\sigma}px_1x_3\end{bmatrix} \quad (26)$$

$$G_1(X_1) = \begin{bmatrix}0 & \frac{3p}{2J}(1-\sigma)Lsx_3\\ \frac{1}{Tr} & 0\end{bmatrix};\ G_2 = \frac{1}{\sigma Ls} \quad (27)$$

Induction motor is a second-order vector system in strict feedback form which can be easily submitted to Backstepping control design and integral Backstepping control design. Only two steps are necessary to establish the control law [9], [17], [19]. This paper proposes to separate the design into a slow dynamic stage and a fast dynamic stage. This has the advantage of simplifying the control law and thus offering more robustness to the system.

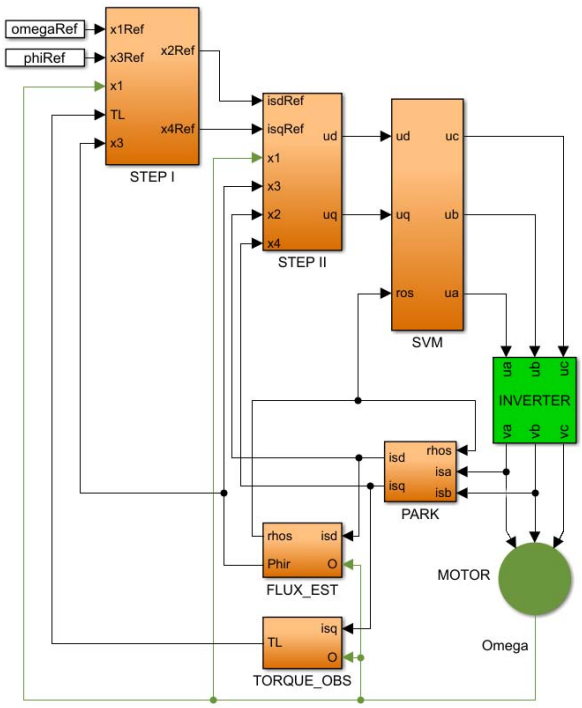

Fig. 2. Synoptic diagram of Backstepping control

III.1. First Step Control Design

The objective of this step is to control the variable X_1, which represents speed and rotor flux, by the intermediate variable X_2. It is necessary to find the intermediate control law X_{2ref} such as:

$$X_2 = X_{2ref} \tag{28}$$

The first error (29) is given, and then a new variable based on this error and its integration (30) is defined [23]. Therefore, the stabilizing control term is introduced in the derivative of this new variable (32).

$$E_1 = X_1 - X_{1ref} \tag{29}$$

$$Z_1 = E_1 + H_1 \int E_1 dt \tag{30}$$

$$\dot{Z}_1 = \dot{E}_1 + H_1 E_1 = \dot{X}_1 - \dot{X}_{1ref} \tag{31}$$

$$\dot{Z}_1 = F_1(X_1) + G_1(X_1) X_{2ref} - \dot{X}_{1ref} + H_1 E_1 = \\ = -K_1 Z_1 \tag{32}$$

In fact, Lyapunov candidate function is positive and its derivative is negative when the coefficients of the diagonal matrix K_1 are positive (33). This ensures stability in this step [24]:

$$V_1 = \frac{1}{2} Z_1^T Z_1 > 0 \rightarrow \dot{V}_1 = Z_1^T \dot{Z}_1 = -Z_1^T K_1 Z_1 < 0 \tag{33}$$

Thus, the provisional control law for this step is given in Equation (34):

$$X_{2ref} = [G_1(X_1)]^{-1} \times \\ \times \left(-K_1 Z_1 - H_1 E_1 - F_1(X_1) + \dot{X}_{1ref}\right) \tag{34}$$

III.2. Second Step Control Design

In this step, the error of the desired provisional control (35) is defined in order to calculate the main control law.

A new variable is defined to introduce integrators (36):

$$E_2 = X_2 - X_{2ref} \tag{35}$$

$$Z_2 = E_2 + H_2 \int E_2 dt \tag{36}$$

$$\dot{Z}_2 = \dot{E}_2 + H_2 E_2 = \dot{X}_2 - \dot{X}_{2ref} \tag{37}$$

$$\dot{Z}_2 = F_2(X_1, X_2) + G_2 U - \dot{X}_{2ref} + H_2 E_2 \\ = -K_2 Z_2 \tag{38}$$

Lyapunov candidate function is positive and its derivative is negative when the coefficients of the diagonal matrix K_2 are positive (39). Therefore, stability is ensured:

$$V_2 = \frac{1}{2} Z_2^T Z_2 > 0 \rightarrow \dot{V}_2 = Z_2^T \dot{Z}_2 = -Z_2^T K_2 Z_2 < 0 \tag{39}$$

The main control law is given in Equation (40):

$$U = G_2^{-1}\left(-K_2 Z_2 - H_2 E_2 - F_2(X_1, X_2) + \dot{X}_{2ref}\right) \tag{40}$$

Finally, control algorithm is given by Equations (41)-(46):

$$E_1 = X_1 - X_{1ref} \tag{41}$$

$$Z_1 = E_1 + H_1 \int E_1 dt \tag{42}$$

$$X_{2ref} = [G_1(X_1)]^{-1}\left(-K_1 Z_1 - H_1 E_1 - F_1(X_1)\right) \tag{43}$$

$$E_2 = X_2 - X_{2ref} \tag{44}$$

$$Z_2 = E_2 + H_2 \int E_2 dt \tag{45}$$

$$U = G_2^{-1}\left(-K_2 Z_2 - H_2 E_2 - F_2(X_1, X_2)\right) \tag{46}$$

$\dot{X}_{1ref}$ is zero when the speed and the rotor flux set points are zero. On the other hand $\dot{X}_{2ref}$ is neglected since the dynamics of the first step is taken very slow compared to the dynamics of the second step:

III.3. Backstepping Controller Parameters Calculation

According to Lyapunov method, the system is stable when the controller coefficients are positive. However, it is necessary to choose the values of these coefficients that guarantee the desired dynamic performances. On one hand, error vectors and their derivatives are given by the Equations (47) and (48):

$$\dot{E}_1 = -H_1 E_1 - K_1 Z_1; \quad \dot{Z}_1 = -K_1 Z_1 \tag{47}$$

$$\dot{E}_2 = -H_2 E_2 - K_2 Z_2; \quad \dot{Z}_2 = -K_2 Z_2 \tag{48}$$

with:

$$E_1 = \begin{bmatrix} e_1 \\ e_3 \end{bmatrix} = \begin{bmatrix} x_1 - x_{1ref} \\ x_3 - x_{3ref} \end{bmatrix} \tag{49}$$

$$E_2 = \begin{bmatrix} e_2 \\ e_4 \end{bmatrix} = \begin{bmatrix} x_2 - x_{2ref} \\ x_4 - x_{4ref} \end{bmatrix} \tag{50}$$

$$Z_1 = \begin{bmatrix} z_1 \\ z_3 \end{bmatrix} = \begin{bmatrix} e_1 \\ e_3 \end{bmatrix} + H_1 \int \begin{bmatrix} e_1 \\ e_3 \end{bmatrix} dt \tag{51}$$

$$Z_2 = \begin{bmatrix} z_2 \\ z_4 \end{bmatrix} = \begin{bmatrix} e_2 \\ e_4 \end{bmatrix} + H_2 \int \begin{bmatrix} e_2 \\ e_4 \end{bmatrix} dt \tag{52}$$

On the other hand, matrices of controller coefficients are given by Equations (53) and (54):

$$K_1 = \begin{bmatrix} k_1 & 0 \\ 0 & k_3 \end{bmatrix}; \quad H_1 = \begin{bmatrix} h_1 & 0 \\ 0 & h_3 \end{bmatrix} \tag{53}$$

$$K_2 = \begin{bmatrix} k_2 & 0 \\ 0 & k_4 \end{bmatrix}; \quad H_2 = \begin{bmatrix} h_2 & 0 \\ 0 & h_4 \end{bmatrix} \tag{54}$$

Thus, it is possible to write the separate error state-space equations (55) and (56) from the vector error equations [8]. These are second order systems:

$$\begin{bmatrix} \dot{e}_1 \\ \dot{z}_1 \end{bmatrix} = \begin{bmatrix} -h_1 & -k_1 \\ 0 & -k_1 \end{bmatrix} \begin{bmatrix} e_1 \\ z_1 \end{bmatrix} \\ \begin{bmatrix} \dot{e}_3 \\ \dot{z}_3 \end{bmatrix} = \begin{bmatrix} -h_3 & -k_3 \\ 0 & -k_3 \end{bmatrix} \begin{bmatrix} e_3 \\ z_3 \end{bmatrix} \tag{55}$$

$$\begin{bmatrix} \dot{e}_2 \\ \dot{z}_2 \end{bmatrix} = \begin{bmatrix} -h_2 & -k_2 \\ 0 & -k_2 \end{bmatrix} \begin{bmatrix} e_2 \\ z_2 \end{bmatrix} \\ \begin{bmatrix} \dot{e}_4 \\ \dot{z}_4 \end{bmatrix} = \begin{bmatrix} -h_4 & -k_4 \\ 0 & -k_4 \end{bmatrix} \begin{bmatrix} e_4 \\ z_4 \end{bmatrix} \tag{56}$$

From Hurwitz characteristic polynomial $P(\lambda)$ of each system, the coefficients are calculated to ensure a unitary damping factor and a natural frequency relative to response time $trv = 200$ ms for velocity and rotor flux, as well as a response time $trc = 20$ ms for direct and quadratic components of stator current. This is the pole placement approach used to ensure the desired behaviour of the controlled system. In this paper, the damping factor is set to the value $m = 1$ in order to avoid any overshoot especially for speed response while natural frequency ω_n is calculated from response time. In this case, the controlled system has two repeated real poles.

- First step:

$$P(\lambda) = \det \begin{bmatrix} \lambda + h_1 & k_1 \\ 0 & \lambda + k_1 \end{bmatrix} = \\ = \det \begin{bmatrix} \lambda + h_3 & k_3 \\ 0 & \lambda + k_3 \end{bmatrix} = (\lambda + \omega_n)^2 \tag{57}$$

$$m = 1 \rightarrow \omega_n = \frac{4.75}{trv} = \frac{4.75}{0.2} = 23.75 \tag{58}$$

$$k_1 = h_1 = k_3 = h_3 = \omega_n = 23.75 \tag{59}$$

- Second step:

$$P(\lambda) = \det \begin{bmatrix} \lambda + h_2 & k_2 \\ 0 & \lambda + k_2 \end{bmatrix} = \\ = \det \begin{bmatrix} \lambda + h_4 & k_4 \\ 0 & \lambda + k_4 \end{bmatrix} = (\lambda + \omega_n)^2 \tag{60}$$

$$m = 1 \rightarrow \omega_n = \frac{4.75}{trc} = \frac{4.75}{0.02} = 237.5 \tag{61}$$

$$k_2 = h_2 = k_4 = h_4 = \omega_n = 237.5 \tag{62}$$

IV. Variables Estimation and Zero Compensation

In this work, quantities that can be measured are voltages, currents, and speed. Rotor flux is not measured but they are required in the elaboration of control law since it is a controlled variable, so it should be estimated.

Load torque also appears in control law, so it should be observed because its value is assumed to be unknown. In fact, adding integrator in speed loop is sufficient for constant disturbance rejection. However, introducing disturbance value in control law improves its rejection even when it is not a constant. Therefore, a load torque observer is proposed in this paper. For more enhancements, a compensating filter is proposed in order to delete speed overshoot.

IV.1. Rotor Flux Estimator

This paper proposes to estimate rotor flux magnitude in the rotor flux reference frame as well as the velocity and the position of this frame relative to the stator. Since this frame is aligned with the rotor flux, the quadrature component is zero and only the direct component has to be estimated [25], [3]. From the state-space representation of induction motor expressed in the rotating reference frame, Equation (63), which allows the rotor flux magnitude estimation, is extracted:

$$\frac{d}{dt} i_{\varphi d} = -\frac{1}{Tr} i_{\varphi d} + \frac{1}{Tr} i_{sd} \tag{63}$$

Then, this estimated rotor flux magnitude is used to estimate velocity of the frame, which is also the speed of the rotor flux vector:

$$\frac{d\rho s}{dt} = p\Omega + \frac{1}{Tr} \frac{i_{sq}}{i_{\varphi d}} \tag{64}$$

Finally, the rotor flux frame reference position is obtained by integration of frame reference velocity:

$$\rho s = \int p\Omega + \frac{1}{Tr} \frac{i_{sq}}{i_{\varphi d}} dt$$

IV.2. Load Torque Observer

In general, the load torque is an unknown variable and independent of the system variables. In the proposed control Backstepping strategy, this torque should be observed and then used by the control algorithm. This work proposes a Luenberger observer in the rotor flux reference frame from the state-space Equation (65). In this equation, the load torque is assumed to be a constant or a slow variable so its derivative is zero or almost zero and control variable comes from flux estimator [17].

Indeed, in many applications such as electric vehicles the load torque is a variable as slow as its derivative can be considered null. Otherwise load torque can be analysed and modelled by using stochastic methods if it does not depend on other variables [17], [26]:

$$\frac{d}{dt} \begin{bmatrix} \Omega \\ T_L \end{bmatrix} = \begin{bmatrix} -\frac{f}{J} & -\frac{1}{J} \\ 0 & 0 \end{bmatrix} \begin{bmatrix} \Omega \\ T_L \end{bmatrix} + \begin{bmatrix} \frac{3p}{2J}(1-\sigma)Ls \\ 0 \end{bmatrix} i_{\varphi d} i_{sq} \tag{65}$$

Thus, the load torque observer's equation is given by (66) where k_{O1} and k_{O2} are the observer parameters:

$$\frac{d}{dt}\begin{bmatrix}\tilde{\Omega}\\ \tilde{T}_L\end{bmatrix}=\begin{bmatrix}-\frac{f}{J} & -\frac{1}{J}\\ 0 & 0\end{bmatrix}\begin{bmatrix}\tilde{\Omega}\\ \tilde{T}_L\end{bmatrix}+ \\ +\begin{bmatrix}\frac{3p}{2J}(1-\sigma)Ls\\ 0\end{bmatrix}i_{\varphi d}i_{sq}-\begin{bmatrix}k_{O1}\\ k_{O2}\end{bmatrix}(\tilde{\Omega}-\Omega) \tag{66}$$

This gives the state-space equation of observation error (67) that helps for parameters calculation:

$$\frac{d}{dt}\begin{bmatrix}\tilde{\Omega}-\Omega\\ \tilde{T}_L-T_L\end{bmatrix}=\begin{bmatrix}-\frac{f}{J}-k_{O1} & -\frac{1}{J}\\ -k_{O2} & 0\end{bmatrix}\begin{bmatrix}\tilde{\Omega}-\Omega\\ \tilde{T}_L-T_L\end{bmatrix} \tag{67}$$

The observer should have a very fast dynamics compared to that of the system respecting the sampling period which is also the step of the control algorithm $T_{SMP}=500$ µs. Thus, response time chosen for the load torque observer is $tro=5$ ms. From characteristic polynomial of the error state-space matrix (67), observer parameters are determined by setting damping factor to $m=1$:

$$P(\lambda)=det\begin{bmatrix}\lambda+\frac{f}{J}+k_{O1} & \frac{1}{J}\\ k_{O2} & \lambda\end{bmatrix}= \\ =\lambda^2+\left(\frac{f}{J}+k_1\right)\lambda-\frac{k_2}{J}= \\ =\lambda^2+2m\omega_n\lambda+\omega_n^2 \tag{68}$$

$$m=1\rightarrow\omega_n=\frac{4.75}{tro}=\frac{4.75}{0.005}=950 \tag{69}$$

This yields:

$$k_{O1}=2\omega_n-\frac{f}{J}\approx 1900 \tag{70}$$

$$k_{O2}=-J\omega_n^2=-45125 \tag{71}$$

IV.3. Compensating Filter

Equation (55) is obtained from Backstepping control law introduce two poles in the transfer function between the controlled variables and their references which has been calculated to satisfy requirements. However, a zero appears in this transfer function due to the integrators added in controller design. The transfer function zero causes an overshoot in the speed response of a step reference and needs to be compensated by inserting a low-pass filter.

From the errors state-space representation of Equation (55) Laplace transform is applied:

$$s\begin{bmatrix}\mathcal{E}_1(s)\\ \zeta_1(s)\end{bmatrix}-\begin{bmatrix}e_1(0)\\ z_1(0)\end{bmatrix}=-\begin{bmatrix}h_1 & k_1\\ 0 & k_1\end{bmatrix}\begin{bmatrix}\mathcal{E}_1(s)\\ \zeta_1(s)\end{bmatrix} \tag{72}$$

Thus:

$$\begin{bmatrix}\mathcal{Y}_1(s)\\ \zeta_1(s)\end{bmatrix}= \\ =-(sI+A)^{-1}\begin{bmatrix}x_{1ref}(0)\\ x_{1ref}(0)\end{bmatrix}+\begin{bmatrix}\mathcal{Y}_{1ref}(s)\\ 0\end{bmatrix} \tag{73}$$

with:

$$\begin{bmatrix}\mathcal{E}_1(s)\\ \zeta_1(s)\end{bmatrix}=\mathcal{L}\left(\begin{bmatrix}e_1\\ z_1\end{bmatrix}\right);\ \begin{bmatrix}\mathcal{Y}_1(s)\\ \mathcal{Y}_{1ref}(s)\end{bmatrix}=\mathcal{L}\left(\begin{bmatrix}x_1\\ x_{1ref}\end{bmatrix}\right) \tag{74}$$

$$A=\begin{bmatrix}h_1 & k_1\\ 0 & k_1\end{bmatrix} \tag{75}$$

For Heaviside step function:

$$\mathcal{Y}_{1ref}(s)=\frac{x_{1ref}(0)}{s} \tag{76}$$

This yields:

$$\begin{bmatrix}\mathcal{Y}_1(s)\\ \zeta_1(s)\end{bmatrix}=\left(\begin{bmatrix}1\\ 0\end{bmatrix}-s(sI+A)^{-1}\begin{bmatrix}1\\ 1\end{bmatrix}\right)\mathcal{Y}_{1ref}(s) \tag{77}$$

Therefore, speed transfer function is given by:

$$\frac{\mathcal{Y}_1(s)}{\mathcal{Y}_{1ref}(s)}=\frac{(h_1+k_1)s+h_1k_1}{(s+h_1)(s+k_1)} \tag{78}$$

Finally, the zero that appears in this transfer function is compensated by the following low-pass filter:

$$F(s)=\frac{h_1k_1}{(h_1+k_1)s+h_1k_1} \tag{79}$$

V. PIL Experimentation

First, the whole control strategy proposed in this work is simulated on Simulink. Then the code related to this control algorithm is generated and transferred to the DSP that communicate with Simulink [27], [1], [7]. The experimental validation is performed using PIL (Processor In the Loop) technique. In fact, control algorithm runs on the DSP TMS320F28069M from Texas Instruments whereas the induction motor and the inverter are implemented on Simulink. Communication between DSP and PC is insured by serial link via an USB port.

The proposed experimental platform is given in Figure 3. It contains a personal computer integrating Matlab/Simulink R2017b with Code Composer Studio CCSv7, the development board LAUNCHXL-F28069M and a serial link using USB ports.

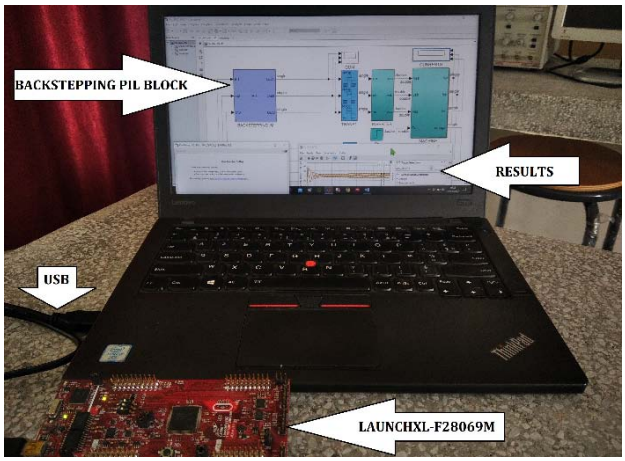

Fig. 3. Experimental platform

For the first part of validation, modulation frequency of the inverter and the sampling frequency have the following value:

$$f_{PWM} = f_{SMP} = 2000 \text{ Hz} \rightarrow T_{SMP} = 500 \text{ µs}$$

The second part of validation is performed under a greater value of this frequency:

$$f_{PWM} = f_{SMP} = 10000 \text{ Hz} \rightarrow T_{SMP} = 100 \text{ µs}$$

Figures 4-7 represent the experimental results of the proposed integral Backstepping strategy combined with load torque observer for $f_{SMP} = 2000$ Hz. Figures 8 and 9 illustrate the experimental results of the electromagnetic torque and the stator currents for the second value of sampling frequency $f_{SMP} = 10$ kHz, which is also the carrier value. At the starting time, the rated rotor flux 0.35 Wb and the speed value 100 rad/s are applied as the controlled variables references. At the time $t = 0.5$ s, the rated load torque 20 Nm is introduced as a load torque disturbance. The SVM inverter can generate a fundamental voltage of RMS 220 V from a DC bus of 539 V instead of 622 V with SPWM technique. In addition, the amplitude of triangular carrier signal is set to 311, which is possible with a DSP, in order to have a unitary average model for the SVM inverter; so that, DC bus and carrier amplitude do not appear in controller design. Figure 4 represents rotor flux and motor speed responses, which are the controlled variables in this work. For both signals, the rotor flux and the speed references are reached with zero static error and no ripples. Moreover, the speed dynamic is in accordance with the requirements about the speed response time $trv = 200$ ms and the damping factor $m = 1$.

The observed overshoot in rotor flux response is due to the zero of its state-space model, which is not compensated like that of the speed. The effect of introducing the estimated value of the load torque is clear in this figure because it limits the speed deviation caused by the load torque.

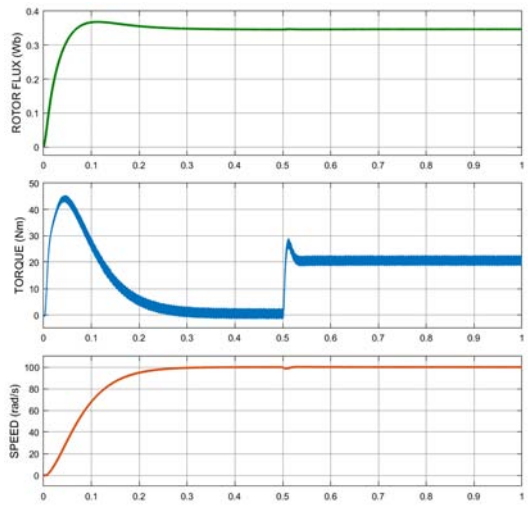

Fig. 4. Rotor flux, torque and speed responses by PIL

This figure gives also the electromagnetic torque response with a pic value limited at $T_{MPIC} = 45$ Nm, which is not excessive compared to the electromagnetic rated value $T_N = 20$ Nm. Measured electromagnetic torque ripple cannot be neglected $\Delta T_M = 20$ %. However its effect on the motor speed is low-pass filtered by the machine behaviour, so no need to decrease this ripple by increasing carrier frequency of the inverter in this context. Figure 5 gives the reference signals coming from the SVM block and intended to drive the voltage-source inverter that feeds the motor and a horizontal zoom of these signals. A typical SVM waveform is obtained during this experimentation and, in the middle of this figure, some distortion resulting from the load torque change can be seen. Of course, reference signals are distorted during the starting phase.

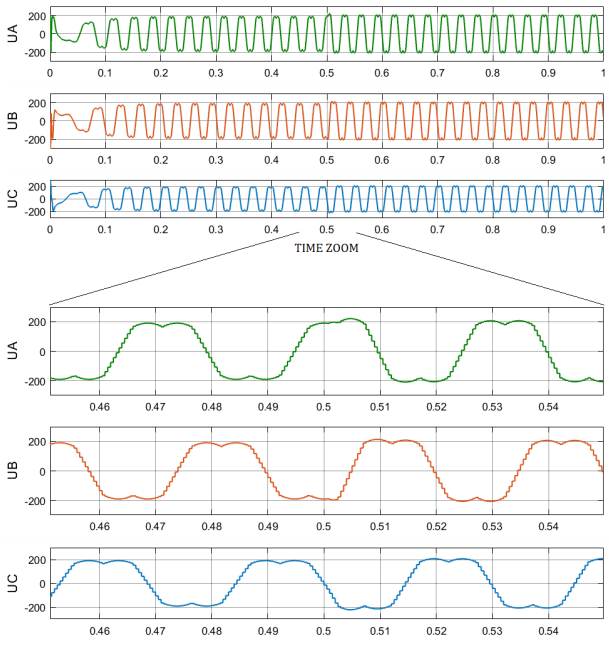

Fig. 5. SVM reference signals for inverter by PIL

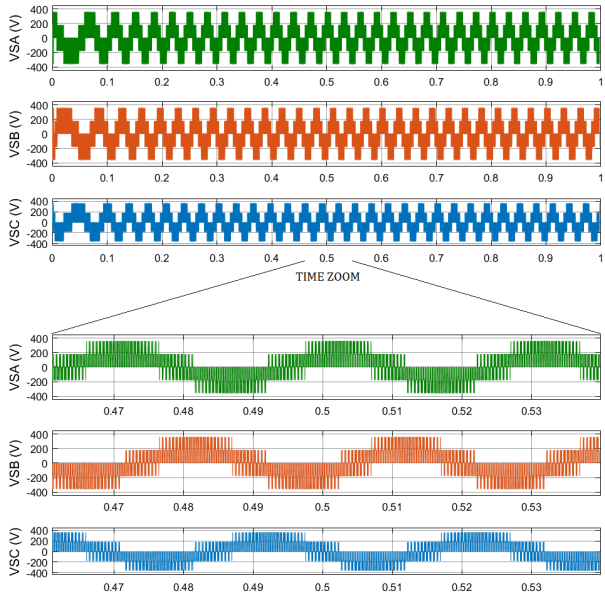

Fig. 6. Stator voltages using PIL technique

Figure 6 shows the generated voltages from the SVM inverter supplying the induction motor and a time zoom of these signals. It is a balanced three-phase system but clearly highly distorted. Figure 7 shows transient and steady-state the stator currents response obtained from PIL technique then a time zoom of these waveforms. An increase of the currents at start-up is observed $I_{PIC} = 42$ A although it is acceptable for induction machine when compared to the current rated value of the controlled motor in this paper $I_N = 7$ A. This pic is due to the choice of a speed response time close to the response time of a natural direct start. When the load torque is applied in the middle of the time axis, it can be clearly observed that stator currents increase. Measured current distortion in this experimentation $THD = 5.65\ \%$ is not an excessive value but it can be reduced by increasing carrier frequency for more efficiency of the induction motor.

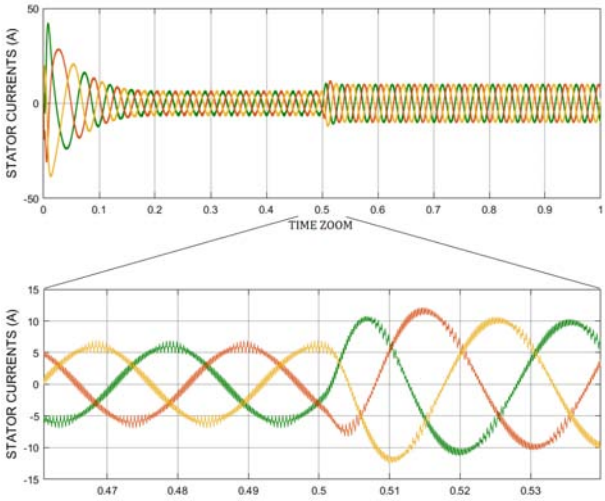

Fig. 7. Stator currents using PIL technique

Thus, in the continuation of this experimentation another test is proposed for a higher carrier frequency $f_{PWM} = 10$ kHz. Results for electromagnetic torque and stator current responses are given in Figures 8 and 9.

Figure 8 represents the electromagnetic torque response when carrier and sampling frequency is set at 10 kHz. When compared to the electromagnetic torque response at 2 kHz illustrated in Figure 4, similarity between waveforms is visually indisputable. However, electromagnetic ripple in the second test is clearly reduced by increasing carrier frequency. Measured electromagnetic torque ripple this time is $\Delta T_M = 5\ \%$ instead of electromagnetic torque ripple $\Delta T_M = 20\ \%$ measured when the carrier frequency was lower in the first test. Figure 9 shows stator currents response obtained from the second PIL test at the carrier frequency 10 kHz with a zoom at 0.5 seconds. Visually, the quality of the currents waveforms is clearly enhanced in term of distortion. Measured total harmonic distortion during this test is $THD = 1.16\ \%$ instead of the value $THD = 5.65\ \%$ obtained in the previous test.

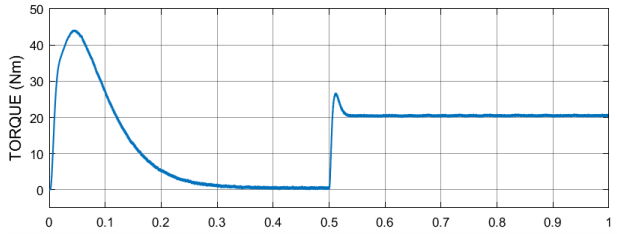

Fig. 8. Electromagnetic torque by PIL for 10 kHz

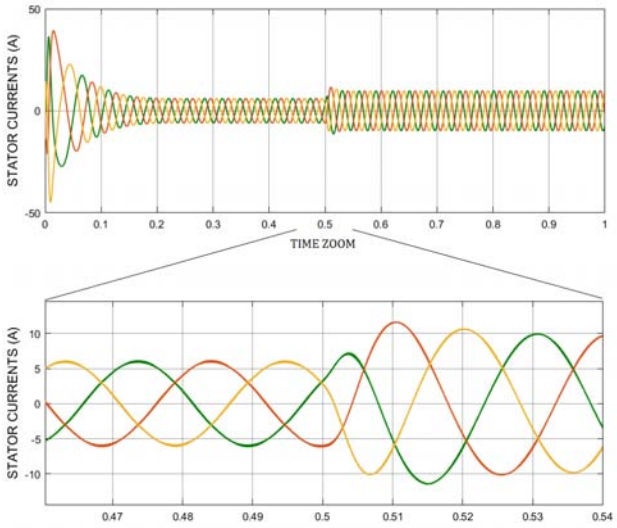

Fig. 9. Stator currents by PIL for 10 kHz

TABLE I
CODE EXECUTION PROFILING REPORT

Section	Maximum Execution Time in ns	Average Execution Time in ns	Calls
BACKSTEPPING_initialize	6178	6178	1
BACKSTEPPING_step	**85133**	84127	10001
BACKSTEPPING_terminate	611	611	1

VI. Conclusion

Backstepping is a nonlinear control strategy that can be easily adapted to the nonlinear SISO or MIMO systems such as the induction motor, which is the subject of this paper. Firstly, induction motor is modelled in the rotor flux reference frame in order to obtain simpler equations. Then this model is written in vector form because it allows controlling two variables at the same time, i.e. rotor flux and motor speed. Secondly, Backstepping control design is performed by adding integrators in order to enhance controller accuracy. This design has consisted in two steps because the induction motor model is fourth order with two variables to control. In order to minimize the effect of the load torque on motor speed, a load torque observer based on the Luenberger method is proposed in this paper. Rotor flux estimator is also required to develop this control strategy, since rotor flux is a controlled variable. In this work, a compensating filter is designed in order to compensate the zero dynamic appearing in the speed loop, so that speed overshot is suppressed. This work proposes especially a method for calculating the Backstepping controller parameters in order to satisfy precisely the dynamic-response requirements of the drive, namely response time and damping factor. After completing the controller design, a Simulink simulation is performed and the code related to the control algorithm is generated and validated on the Texas Instruments F28069M board using PIL technique.

Thus, the code runs on DSP and communicates via a fast USB serial link with the model of the induction motor supplied by a SVM inverter running on Simulink. The obtained results show the good functioning of the controller based on Backstepping with integrators. The speed responds in the time foreseen and does not have any overshoot, just as specified. As for the flux, the precision is respected as well as the dynamics, although an overshoot appears because it is not compensated.

Responses of the SVM reference signals, stator voltages, and currents are typical. In fact, two validation tests are performed using PIL technique for two values of the carrier frequency 2 kHz and then 10 kHz. A comparison of these tests results proves that for the second carrier frequency, electromagnetic torque ripples and stator currents distortion are optimized.

Finally, code execution profiling report obtained after PIL test is given in Table I. In Table I, the most important value is the maximum execution time for one step of the control algorithm $T_{STP} = 85133$ ns which has to be lower than the smallest sampling period $T_{SMP} = 100$ µs. In this work, this condition is guaranteed:

$$T_{STP} < T_{SMP}$$

Therefore, the proposed control algorithm can be used to control an actual association inverter-motor. In conclusion, Backstepping strategy is easily adapted to nonlinear systems, in this case the induction motor. It gives good results especially when it is combined with integrators and disturbance observers, in this work, a limitation of load torque effect is observed. Compared to other works [26], this paper proposes a simple and robust controller design because it is based on a compact vector representation of the induction motor, the use of integrators and the separation of the dynamics in the Backstepping steps. In addition, this work proposes a PIL validation for two values of the carrier frequency and discusses its effect on waveforms ripple and distortion. Results show that for 10 kHz, waveforms quality are better.

Backstepping controller design is simple since it is methodical: there are steps to follow. The implementation of the control algorithm is also simple thanks to the generation of code on Simulink. In future works, the aim is to realize a complete experimental platform.

Appendix 1: Numerical Specifications of Induction Motor

- Rated output power: 3 kW;
- Rated load torque: 20 N m;
- Rated speed: 1455 rpm; p=2;
- Rated voltage and frequency: 220|380 V; 50 Hz;
- Resistances: Rs=0.85 Ω; Rr= 0.16 Ω;
- Cyclic inductances: Ls=0.16 H; Lr= 0.023 H;
- Cyclic mutual Inductance: Msr=0.058 H
- Moment of inertia: J=0.05 kg m^2
- Coefficient of friction: f=0.005 N m/rad s^{-1}
- Time constants: Ts=0.188 s; Tr= 0.144 s;
- Current time constant: τ=7.36 ms;
- Dispersion coefficient: σ=0.08587
- DC bus voltage: E $= 220\sqrt{2}\sqrt{3} = 539$ V

Appendix 2: Specifications of Development Board LAUNCHXL-F28069M

- CPU and Frequency: C28x, CLA;90 Mhz;
- Memory: 100kB RAM, 256kB Flash;
- Analog/Digital Converters ADC: Dual Sample & Hold, 16 Channels, 12 bits;
- Pulse Width Modulation PWM: 12 Channels;
- Quadrature Encoder Interfaces QEP: 2;
- Digital I/O GPIO: 54;
- Communication Bus: 2 SCI, 2 SPI, 1 I2C, 1USB;
- Timers: 3 32-Bit CPU, 1 WD;
- On-board emulator: XDS100v2.

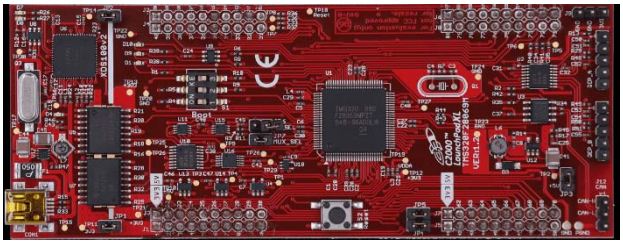

Fig. 1A. Development board

References

[1] M. Elhaissouf, E. Lotfi, B. Rached, M. Elharoussi, and A. Barazzouk, DSP Implementation In the Loop of the Indirect Rotor Field Orientation Control for the Three-Phase Asynchronous Machine, *Assoc. Comput. Mach.*, 2017.

[2] N. Kabache, S. Moulahoum and H. Houassine, FPGA Implementation of direct Rotor Field Oriented Control for Induction Motor, *2013 18th International Conference on Methods & Models in Automation & Robotics (MMAR)*, Miedzyzdroje, Poland, 2013, pp. 485-489. doi: 10.1109/MMAR.2013.6669958

[3] El Haissouf, M., El Haroussi, M., Ba-razzouk, A., Processor in the Loop Comparative Study of Indirect Rotor Field Oriented Control, Direct Self Control, Direct Torque Control and Space Vector Modulation Based Direct Torque Control for Induction Motor Drives, (2021) *International Review on Modelling and Simulations (IREMOS)*, 14 (6), pp. 451-465. doi: https://doi.org/10.15866/iremos.v14i6.20997

[4] M. Aktas, K. Awaili, M. Ehsani, and A. Arisoy, Direct torque control versus indirect field-oriented control of induction motors for electric vehicle applications, *Eng. Sci. Technol. an Int. J.*, vol. 23, no. 5, pp. 1134–1143, 2020.

[5] V. Kosti, M. Petronijevi, N. Mitrovi, and B. Bankovi, Experimental Verification Of Direct Torque Control Methods For Electric Drive Application, *Autom. Control Robot.*, vol. 8, 2009.

[6] G. Gatto, I. Marongiu, A. Serpi and A. Perfetto, A Predictive Direct Torque Control of Induction Machines, *2008 International Symposium on Power Electronics, Electrical Drives, Automation and Motion*, Ischia, Italy, 2008, pp. 1103-1108. doi: 10.1109/SPEEDHAM.2008.4581129

[7] F. Mehazzem, A. Lokmane, A. Reama, and D. Constantine, Real time implementation of backstepping-multiscalar control to induction motor fed by voltage source inverter, *Int. J. Hydrogen Energy*, vol. 42, no. 28, pp. 17965–17975, 2017. doi: 10.1016/j.ijhydene.2017.05.035

[8] R. Trabelsi, A. Khedher, M. Faouzi, and M. Faouzi, Backstepping control for an induction motor using an adaptive sliding rotor-flux observer, *Electr. Power Syst. Res.*, vol. 93, pp. 1–15, 2012. doi: 10.1016/j.epsr.2012.06.004

[9] F. Mehazzem, A. L. Nemmour, A. Reama, and H. Benalla, Nonlinear Integral Backstepping Control for Induction Motors, *Acemp - Electromotion*, no. September, pp. 8–10, 2011.

[10] Abbou, A., Mahmoudi, H., Design of a new sensorless controller of induction motor using backstepping approach, (2008) *International Review of Electrical Engineering (IREE)*, 3 (1), pp. 166-173.

[11] Benzineb, O., Salhi, H., Tadjine, M., Boucherit, M. S., Benbouzid, M. E. H., A PI/Backstepping Approach for Induction Motor Drives Robust Control, (2010) *International Review of Electrical Engineering (IREE)*, 5 (2), pp. 426-432.

[12] Ouchatti, A., Abbou, A., Akherraz, M., Taouni, A., Induction Motor Controller Using Fuzzy MRAS and Backstepping Approach, (2014) *International Review of Electrical Engineering (IREE)*, 9 (3), pp. 511-518.

[13] Aichi, B., Bourahla, M., Kendouci, K., High-Performance Speed Control of Induction Motor Using a Variable Gains Backstepping: Experimental Validation, (2018) *International Review of Electrical Engineering (IREE)*, 13 (4), pp. 342-351. doi: https://doi.org/10.15866/iree.v13i4.15314

[14] Moutchou, M., Mahmoudi, H., Abbou, A., Sensorless sliding mode-backstepping control of the induction machine, using sliding mode-MRAS observer, (2013) *International Review on Modelling and Simulations (IREMOS)*, 6 (2), pp. 387-395.

[15] Bennassar, A., Abbou, A., Akherraz, M., A New Sensorless Control Design of Induction Motor Based on Backstepping Sliding Mode Approach, (2014) *International Review on Modelling and Simulations (IREMOS)*, 7 (1), pp. 35-42.

[16] Madark, M., Ba-Razzouk, A., Abdelmounim, E., El Malah, M., An Effective Method for Rotor Time-Constant and Load Torque Estimation for High Performance Induction Motor Vector Control, (2017) *International Review on Modelling and Simulations (IREMOS)*, 10 (6), pp. 410-422. doi: https://doi.org/10.15866/iremos.v10i6.12624

[17] C. Chen, H. Yu, F. Gong, and H. Wu, Induction Motor Adaptive Backstepping Control and Efficiency Optimization Based on Load Observer, *Energies*, 2020. doi: 10.3390/en13143712

[18] Y. Azzoug, M. Sahraoui, R. Pusca, and T. Ameid, High-performance vector control without AC phase current sensors for induction motor drives : Simulation and real-time implementation, *ISA Trans.*, vol. 109, pp. 295–306, 2021.

[19] N. Djeghali, M. Ghanes, and J. P. Barbot, Sensorless Fault Tolerant Control Based On Backstepping Strategy For Induction Motors, vol. 44, no. 1. *IFAC*, 2011.

[20] H. B. Imen, Backstepping Controller Design using a High Gain Observer for Induction Motor, *Int. J. Comput. Appl.*, vol. 23, no. 3, pp. 1–6, 2011.

[21] H. Ouadi, F. Giri, A. Elfadili, and L. Dugard, Control Engineering Practice Induction machine speed control with flux optimization, *Control Eng. Pract.*, vol. 18, no. 1, pp. 55–66, 2010. doi: 10.1016/j.conengprac.2009.08.006

[22] M. Jalalifar and A. F. Payam, Dynamic Modeling and Simulation of an Induction Motor with Adaptive Backstepping Design of an Input-Output Feedback Linearization Controller in Series Hybrid Electric Vehicle, *SERBIAN J. Electr. Eng.*, vol. 4, no. 2, pp. 119–132, 2007.

[23] G. Abdelmadjid, B. S. Mohamed, T. Mohamed, S. Ahmed, and M. Youcef, An improved stator winding fault tolerance architecture for vector control of induction motor: Theory and experiment, *Electr. Power Syst. Res.*, vol. 104, pp. 129–137, 2013. doi: 10.1016/j.epsr.2013.06.023

[24] C. Ben Regaya, F. Farhani, and A. Zaafouri, An Adaptive Sliding-Mode Speed Observer, *ICIC Int.*, vol. 11, no. 4, pp. 763–771, 2017.

[25] P. Martin and P. Rouchon, Two simple flux observers for induction motors, *Int. J. Adapt. Control Signal Process.*, vol. 1115, no. March, 2000. doi: 10.1002/(SICI)1099-1115(200003/05)14

[26] F. L. Mapelli, D. Tarsitano, and F. Cheli, MRAS rotor resistance estimators for EV vector controlled induction motor traction drive : Analysis and experimental results, *Electr. Power Syst. Res.*, vol. 146, pp. 298–307, 2017. doi: 10.1016/j.epsr.2017.02.005

[27] L. E. Ortega-García, D. Rodriguez-Sotelo, J. C. Nuñez-Perez, Y. Sandoval-Ibarra, and F. J. Perez-Pinal, DSP-HIL Comparison between IM Drive Control Strategies, *Electronics*, vol. 10, no. 8, p. 921, 2021.

Authors' information

Department of Applied Physics, MISI Laboratory, FST Settat, University Hassan 1stSettat, Morocco.

Mohammed El Haissouf received Master's degree in Automatic, Signal Processing and Industrial Computing from FST, Hassan 1st University, Settat, Morocco in 2017.Currently, he is preparing his PhD titled "Variable speed drives for AC machines based on advanced digital controls" in the Laboratory of System Analysis and Information Processing at Hassan 1stUniversity.His research consists in advanced control of the AC machines and algorithm implementation.

Mustapha El Haroussi received his PhD in Error Correcting Codes from Mohammed V University Morocco in 2013. In 2014 he joined, as Professor, applied Physics department of FST, Hassan I University, Settat, Morocco. His current research interests include hardware design of algorithms applied to information processing and control of industrial systems at System Analysis and Information Technology Laboratory at Hassan I University, Settat, Morocco.

Abdellfattah Ba-razzouk received the Master's degree (M.Sc.A.) in industrial electronics from the Université du Québec à Trois-Rivières (UQTR), Quebec, Canada, in 1993, and the Ph.D. degree in electrical and computer engineering from the École Polytechnique de Montréal, Quebec, Canada, in 1998. From 1997 to 2003, he was a Lecturer in "motors modelling and control" at the Department of Electrical and Computer Engineering, UQTR. In September 1998, he joined the Hydro-Quebec Industrial Research Chair on Power and Electrical Energy, UQTR, where he has been a Professional Research Scientist working on "high-performance intelligent control of electrical drives". Since June 2009, he is a Professor in electrical engineering with the Department of Applied Physics and a Researcher affiliated to "Systems Analysis and Information Processing Laboratory", both at the Faculté des Sciences et Techniques, Université Hassan 1er of Settat, Morocco. His research interests include high performance control of adjustable speed drives, parameter identification and adaptive control of electrical motors, neural networks, real-time embedded control systems, renewable energy systems, modelling and computer aided design, and real-time simulation of power electronics systems using multiprocessors platforms.

International Review of Automatic Control (I.RE.A.CO.), Vol. 16, N. 2
ISSN 1974-6059 March 2023

An Extended Kalman Filter-Based Simultaneous Localization and Mapping Algorithm for Omnidirectional Indoor Mobile Robot

Wafa Batayneh[1], Yusra Aburmaileh[1], Ahmad Bataineh[1], Ashfaq Khokhar[2]

Abstract – *Simultaneous Localization And Mapping (SLAM) is the ability of an autonomous robot to localize itself within the surroundings, while also constructing a map. It has several applications in a variety of industries, especially in indoor navigation, Autonomous driving, and robotics. This research uses an omnidirectional mobile robot to present the SLAM algorithm based on Extended Kalman Filter (EKF) in an indoor environment. Usually, SLAM combines data from odometry and other sensors, in order to overcome the accumulating error due to the wheel sliding that usually appears when using the odometry alone. Thus, in this study a Kinect sensor is used along with an odometer sensor in an unknown environment to reach a predefined point with a free collusion path using three main fuzzy controllers as part of its navigation system. The first fuzzy controller is responsible for the goal-seeking problem, where the robot moves towards the goal, the second and third controllers are responsible for static and dynamic obstacles avoidance. The robot changes its direction to avoid the static obstacles and its direction and speed to avoid the dynamic obstacles. An EV3 Lego robot is used to verify the effectiveness of the proposed study. Results shows the effectiveness of the used algorithm; the decentralized algorithm simplifies the control process, which decreases the error with the help of EKF.*

Keywords*: SLAM, EKF, Kinect, Fuzzy, Navigation, Omnidirectional Wheel, Obstacle Avoidance*

Nomenclature

$\boldsymbol{\omega}$	Angular velocities of the robot's wheels
$\mathbf{q_r}$	Posture of the robot corresponding to the global frame
$\dot{\mathbf{q}}_\mathbf{r}$	Velocity of the robot corresponding to the global frame
$\mathbf{m}$	Velocity of the robot corresponding to the body frame
ω_c	Rotational moving corresponding to the body frame
H	Horizontal moving corresponding to the body frame
V	Vertical moving corresponding to the body frame
$\mathbf{q}$	Augmented state vector
$\mathbf{q_i}$	State vector of ith landmark
$\mathbf{R_2}$	Rotation matrix
$\hat{\mathbf{q}}^+$	Mean of the posterior position
$\mathbf{P}^+$	Covariance matrix of the posterior distribution
$\mathbf{P}_{rr}{}^+$	Covariance of robot pose estimate
$\mathbf{P}_{ri}{}^+$	Cross-covariance matrix between the robot and landmarks estimates
$\mathbf{P}_{ij}{}^+$	Map covariance matrices
$\nabla_x h^T$	Jacobian of the observation model
$\hat{\mathbf{q}}_i{}^+$	Augmentation model
$\mathbf{u}$	Control input
$\mathbf{v}$	Process noise
$\mathbf{Z}$	Observation model
$\mathbf{W}$	Zero mean white observation noise
$\mathbf{S}$	Innovation covariance matrix
$\mathbf{e_b}$	Error of goal seeking corresponding to the body frame
$\mathbf{q_{des}}$	Desired posture
S	Kinect's maximum detecting range
S_O	Distance between the static obstacle and the robot
v_D	Dynamic obstacle's velocity
$d_n(i\text{-}1)$	Distance between the dynamic obstacle and the robot
$d_n(i)$	Distance between the robot and the dynamic obstacle after δt time step
v_R	Robot velocity
v_{DR}	Relative velocity between the robot and the dynamic obstacle
SLAM	Simultaneous Localization And Mapping
EKF	Extended Kalman Filter
DoF	Degree of Freedom
EKFSLAM	Extended Kalman Filter Simultaneous Localization And Mapping
GSFC	Goal Seeking Fuzzy Controller
SOAFC	Static Obstacles Avoidance Fuzzy Controller
DOAFC	Dynamic Obstacles Avoidance Fuzzy Controller

 https://doi.org/10.15866/ireaco.v16i2.23401

SISO	Single-Input-Single-Output
MISO	Multi-Input-Single-Output
MIMO	Multi-Input-Multi Output
FoV	Field of View

I. Introduction

The Simultaneous Localization And Mapping (SLAM) is a problem of spatial exploration, where the robot enters an unknown space, observes it, moves inside it; builds a spatial model of it and defines its location inside it. SLAM technique can be found in indoor applications to assist users in navigating through challenging areas including airports, museums, and shopping centers. It can also be used in autonomous driving to navigate the car through traffic, find the best path, and avoid obstacles. Moreover, it has many applications in robotics; such as, mobile robots, drones, and industrial automation. SLAM contains a moving agent; a robot, which is equipped with at least one exteroceptive sensor that can acquire information about its surrounds including a camera, a laser scanner, or a sonar. Moreover, the robot can integrate additional proprioceptive sensor to track its own motion, including wheel encoders, accelerometers, or gyrometers. SLAM includes three basic operations repeated every time step:

1. The motion model, where a mathematical model is required while the robot moves, to eliminate noise and errors in robot location;
2. The inverse observation model, where the robot builds a map of the surrounding environment with the help of some features called landmarks. The inverse observation model is used to find the position of the landmarks depending on the data obtained by the sensors. A landmark is a feature or object in the surrounding that helps the robot locate itself, determine its direction, and build a map of its environment and maintain its position within that map. It can be corners, edges, unique textures, or even other robots;
3. The direct observation model, where the robot uses the landmarks that had been previously mapped to correct its localization and the all landmarks localization.

The SLAM problem is described using probabilistic solution for unknown environments. According to the literature, there are two main types of probabilistic solutions; Kalman filters family [1]-[3] and particle filters (PF) family [4], [5]. The SLAM problem was first proposed in [6] based on Extended Kalman Filter (EKF), and then in 2002, the authors in [7] proposed the FastSLAM by integrating PF and EKF. The efficiency of SLAM algorithms is still being developed and improved until now. Integrating the aforementioned models with an estimator engine (EKF) provides an automated solution to SLAM, where every time one of the three situations occurs, EKF estimation directly offers recursive solutions to localization problems and is appropriate to the robot and landmark positions, and EKFSLAM has been shown to offer the best convergence and consistency [8], [9].

Kim et al. [10] presented a SLAM for outdoor speedy UAV in GPS-denied environment. The system conducted with LiDAR and IMU sensors, where the three dimensional LiDAR system can overcome the lake of GPS. Various strategies were presented in SLAM studies such as the integration in [11] and [12].

Omnidirectional-wheeled robot is distinguished from the differential wheeled mobile robot by its three Degrees of Freedom (DoF), where it moves freely and its motion can be controlled easily. For example, it has been implemented for a trajectory tracking in [13], the control system was developed with Fuzzy controller and the result showed that the error was maintain at 0.2 m. Fuzzy logic controller can be considered as an effective tool for nonlinear controller design [14]-[17]. In [17], a PD-Fuzzy-P controller has been used to enable the robot track the sharp curves' maneuverability successfully, where the decentralized algorithm allows the controller to control each motor separately. The authors of [18] developed a fuzzy control method for an autonomous tricycle robot used in Precision Agriculture (PA), where the study was able to have a 0.2 m tracking error. Usually, SLAM combines data from odometry and other sensors, in order to overcome the accumulating error due to the wheel sliding that usually appears when using the odometry alone. Thus, a Kinect sensor is used along with an odometer sensor to overcome this type of error [19]-[21]. Mihir Kulkarni et al. in [19] have proposed a novel method to enhance a traditional Visual SLAM, where KinectV2 was used for the vision and YOLOv3 was used for detection method. the author in [20] has used TurtleBot2 robot conducted with KinectV2 for indoor SLAM navigation. In [21] the degeneracy cases has been solved with an Inertial Measurement Unit (IMU) with KinectV2 in Visual SLAM. This study provides an Extended Kalman Filter Simultaneous Localization And Mapping (EKFSLAM)-based system for an omnidirectional robot that is constructed using an EV3 Mindstorm. Under unknown environment, the odometer sensor and Kinect sensor feedback are merged, where three main fuzzy controllers are employed for the navigation system to reach a certain goal and avoid static and dynamic obstacles. The decentralized algorithm is used in robot control and uses the three independent components of robot's motion with respect to the body coordinate frame; rotational movement (ω_c), horizontal movement (H) and vertical movement (V), which can be controlled separately with different sub-controllers for each task. In this study, seven sub-controllers are used for the main three controllers; the Goal Seeking Fuzzy Controller (GSFC) uses three sub-controllers to control H, V, and ω_c independently, the Static Obstacles Avoidance Fuzzy Controller (SOAFC) uses two sub-controllers to control H, V independently, and the Dynamic Obstacles Avoidance Fuzzy Controller (DOAFC) uses two sub-controllers to control H, V independently. For experimental validation, an EV3 Mindstorm equipped with omnidirectional wheels is used as a prototype with the help of Kinect sensor.

The remainder of this paper is organized as follows: Section II introduces the System Design of the Mobile Platform. The PD-FUZZY Controller for the three tasks is presented in Section III. Section IV describes the system, and a set of experiments is carried out to demonstrate the superiority of the proposed method in Section V. Finally, conclusion remarks are made in Section VI.

II. System Design of the Mobile Platform

II.1. Omnidirectional Robot Kinetic Model with Decentralized Algorithm

The robot kinetic model will be used with the EKF-SLAM algorithm that determines the instant robot's position at a time. A flexible robot navigation is obtained when the algorithm controlling the robot's motion gives each motor the appropriate speed for each new movement.

Figs. 1 show the configuration of a three-wheel omnidirectional robot where each wheel separated 120° from each other in addition to the EV3 Lego Omnidirectional wheel utilizing a Kinect sensor used for experimental validation.

The angular velocities of the omnidirectional robot's wheels are denoted by $\boldsymbol{\omega}$=[ω_1 ω_2 ω_3], the posture of the robot corresponding to the global frame is denoted by $\mathbf{q_r}$=[x y θ]^T and the velocity is denoted by $\dot{\mathbf{q}}_\mathbf{r}$, where the obtained kinematic equation corresponding to the global frame is:

$$\dot{\mathbf{q}}_r = r\mathbf{A}^{-1}(\theta)\boldsymbol{\omega}_C \tag{1}$$

where:

$$\mathbf{A}(\theta) = \begin{bmatrix} -\sin\theta & \cos\theta & L \\ -\sin(\pi/3-\theta) & -\cos(\pi/3-\theta) & L \\ \sin(\pi/3+\theta) & -\cos(\pi/3+\theta) & L \end{bmatrix}$$

The decentralized algorithm uses the kinematic model that is presented in the body frame, which has been verified in authors' previous work [16], the three velocity components of the omnidirectional robot are shown in Fig. 2, which are vertical motion; *V*, rotational motion; ω_c, and horizontal motion; *H*, which are denoted by **m**=[*H V* ω_c]:

$$\boldsymbol{\omega} = (1/r)\begin{bmatrix} -\sin\theta & \cos\theta & L \\ -\sin(\pi/3-\theta) & -\cos(\pi/3-\theta) & L \\ \sin(\pi/3+\theta) & -\cos(\pi/3+\theta) & L \end{bmatrix} \times \begin{bmatrix} \dot{x} \\ \dot{y} \\ \dot{\theta} \end{bmatrix} = (1/r)\mathbf{A}(\theta)\dot{\mathbf{q}}_r \tag{2}$$

The system in Eq. (1) can be transformed to the body frame as the following:

$$\dot{\mathbf{q}}_r = \mathbf{R}_2(\theta)\mathbf{m} \tag{3}$$

where $\mathbf{R}_2 = \begin{bmatrix} \cos\theta & -\sin\theta & 0 \\ \sin\theta & \cos\theta & 0 \\ 0 & 0 & 1 \end{bmatrix}$ is the rotation matrix.

By substituting Eq. (3) into Eq. (2), yields:

$$\boldsymbol{\omega} = (1/r)\mathbf{A}(\theta)\mathbf{R}_2(\theta)\mathbf{m} \tag{4}$$

and by simplifying $\mathbf{A}(\theta)\mathbf{R}_2(\theta)$ in Eq. (4), yields:

$$\boldsymbol{\omega} = (1/r)\mathbf{B}\mathbf{m} \tag{5}$$

where $\mathbf{B} = \mathbf{A}(\theta)\mathbf{R}_2(\theta) = \begin{pmatrix} 0 & 1 & L \\ -(3)^{1/2}/2 & -1/2 & L \\ (3)^{1/2}/2 & -1/2 & L \end{pmatrix}$,

which is a full rank matrix.

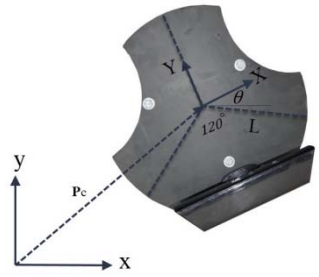

(a)

(b)

Figs. 1. (a) A three Omni-directional wheeled robot configuration. (b) An EV3 Lego Omnidirectional wheel utilizing a Kinect sensor

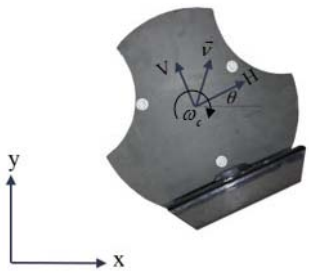

Fig. 2. The velocity vector configuration of the omnidirectional robot corresponding to the body coordinate frame

II.2. EKF-SLAM

The EKF-SLAM-based system is reviewed and summarized in this section. The robot's state vector at time step k is $\mathbf{q_r}(k)$, where N is the static landmarks in the surrounding, and ith landmark's state vector is $\mathbf{q}_i(k)$.

Therefore, the augmented state vector is given by:

$$\mathbf{q}(k) = \begin{bmatrix} \mathbf{q}_r(k)^T & \mathbf{q}_i(k)^T \end{bmatrix}^T \quad i = 1, \ldots, N \tag{6}$$

The mean and covariance of the posterior probability distribution of the state variable $\mathbf{q}$ are estimated by EKF.

$\hat{\mathbf{q}}^+(k)$ denotes the mean of the posterior position each k time. The covariance matrix of the posterior distribution is presented by:

$$\mathbf{P}^+(k) = \begin{bmatrix} \mathbf{P}_{rr}{}^+(k) & \mathbf{P}_{ri}{}^+(k) \\ \mathbf{P}_{ir}{}^+(k) & \mathbf{P}_{ij}{}^+(k) \end{bmatrix} \tag{7}$$

where $\mathbf{P}_{rr}{}^+(k)$ is the covariance of robot pose estimate.

$\mathbf{P}_{ri}{}^+(k) = \mathbf{P}_{ir}{}^+(k)^T$ is the cross-covariance matrix between the robot and landmarks estimates, and $\mathbf{P}_{ij}{}^+(k)$ denotes the map covariance matrices. The robot and landmarks corresponding process model is:

$$\begin{bmatrix} \mathbf{q}_r(k+1) \\ \mathbf{q}_i(k+1) \end{bmatrix} = \begin{bmatrix} f(\mathbf{q}_r(k), \mathbf{u}(k+1)) \\ \mathbf{q}_i(k) \end{bmatrix} + \begin{bmatrix} \mathbf{v}(k+1) \\ 0 \end{bmatrix} \tag{8}$$

where the robot's motion model is f, $\mathbf{u}(k)$ is control input, and $\mathbf{v}(k)$ is the process noise that is zero mean with covariance $\mathbf{w}(k)$. The EKF combines the information from Kinect sensor with the observation model:

$$\mathbf{Z}(k) = h(\mathbf{q}(k)) + \mathbf{w}(k) \tag{9}$$

It can be written with the difference between the robot position and orientation and the observed landmark:

$$\begin{bmatrix} \mathbf{Z}_{r,k} \\ \mathbf{Z}_{\varphi,k} \end{bmatrix} = \begin{bmatrix} \sqrt{\left(x_{r,k} - x_{i,k}\right)^2 + \left(y_{r,k} - y_{i,k}\right)^2} \\ \arctan\left(\dfrac{y_{r,k} - y_{i,k}}{x_{r,k} - x_{i,k}}\right) - \theta_{r,k} \end{bmatrix} + \begin{bmatrix} w_r \\ w_\varphi \end{bmatrix} \tag{10}$$

The Extended Kalman Filter fundamental stages are:

- *Prediction:* The mean and covariance of probability distribution at time step k+1 can be predicted using the probability distribution of k as:

$$\begin{aligned} \hat{\mathbf{q}}^-(k+1) &= f(\hat{\mathbf{q}}^+(k), \mathbf{u}(k)) \\ \hat{\mathbf{Z}}^-(k+1) &= h(\hat{\mathbf{q}}^-(k+1)) \\ \mathbf{P}^-(k+1) &= \nabla_X f(k) \cdot \mathbf{P}^+(k) \nabla_X f^T(k) + \mathbf{Q}(k) \end{aligned} \tag{11}$$

- *Observation:* Measurement error is estimated upon observation of the ith landmark and assuming accurate data association as:

$$\mathbf{v}(k+1) = \mathbf{Z}_i(k+1) - \hat{\mathbf{Z}}_i^-(k+1) \tag{12}$$

and innovation covariance matrix is given by:

$$\mathbf{S}(k+1) = \nabla_X h \cdot \mathbf{P}^-(k+1) \nabla_X h^T(k) + \mathbf{R}(k+1) \tag{13}$$

- *Update:* The mean and covariance of posterior distribution can be obtained as the following:

$$\begin{aligned} \hat{\mathbf{q}}^+(k+1) &= \hat{\mathbf{q}}^-(k+1) + \mathbf{W}(k+1)\mathbf{v}(k+1) \\ \mathbf{P}^+(k+1) &= \mathbf{P}^-(k+1) + \mathbf{W} \cdot \mathbf{S}(k+1)\mathbf{W}^T \end{aligned} \tag{14}$$

Kalman gain is obtained as:

$$\mathbf{W}(k+1) = \mathbf{P}^-(k+1) \nabla_X h^T(k) \cdot \mathbf{S}^{-1}(k+1) \tag{15}$$

where $\nabla_X h^T$ is the Jacobian of the observation model about the predicted state $\hat{\mathbf{q}}^-(k)$. The flow chart of EKFSLAM algorithm is demostrated in Fig. 3.

- *Augmentation:* An Augmentation model is used when a new landmark is observed:

$$\hat{\mathbf{q}}_i{}^+(k+1) = g_i(\hat{\mathbf{q}}_r{}^+(k), \mathbf{Z}(k)) \tag{16}$$

II.3. Kinect Sensor

Both Infrared and ultrasonic sensors have problems regarding to the accuracy and range limitation. Kinect sensor, which is released by Microsoft Company, is able to produce a 3D scan for the surrounding environment with more accuracy. Therefore, in this research, it is used for landmarks and obstacles detection. Where the effective distance of the depth image obtained by Kinect is approximately 0.5 m to 4.5 m, and 60˚ vertical by 70˚ horizontal angle for the Field Of View (FOV). The detected data are used for robot localization and obstacle avoidance.

III. The Fuzzy Controller

Three main tasks for the omnidirectional-wheeled robot are performed to reach the goal with free-collision path including; goal seeking, static and dynamic obstacles avoidance. Each task has its main PD-Fuzzy controller; Goal Seeking Fuzzy Control (GSFC), Static Obstacle Avoidance Fuzzy Control (SOAFC), and Dynamic Obstacle Avoidance Fuzzy Control (DOAFC). The robot starts its path to reach the goal with GSFC with the help of EKF, beyond that, one or both of the two obstacle-avoidance fuzzy controllers will be activated if the Kinect sensor detects any static or dynamic obstacle, then SOAFC and/or DOAFC takes the control depending on the type of the obstacle.

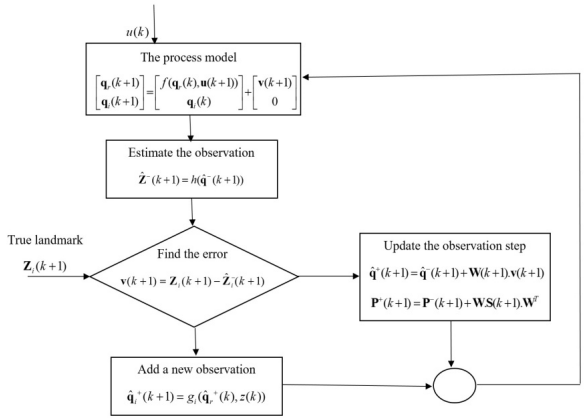

Fig. 3. EKF flowchart

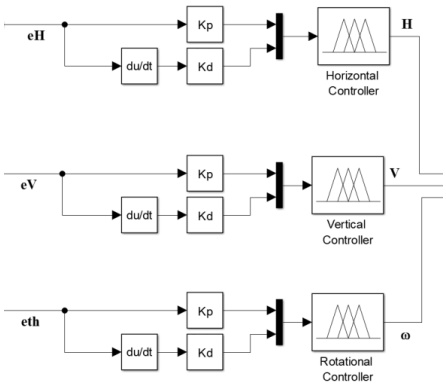

Fig. 4. The GSFC contains three sub controllers

Each of the three main controllers has three PD-Fuzzy sub-controllers for the three motion-component of the robot; the rotational, horizontal and vertical velocities of the robot are the outputs and can be controlled separately.

Using the decentralized algorithm allows to use seven sub-controllers for a flexible collision-free navigation, the seven sub-controllers in this case are Single-Input-Single-Output (SISO) or Multi-Input-Single-Output (MISO) controllers rather than Multi-Input-Multi Output (MIMO) controllers. As a result, each *H*, *V*, and ω_c can be controlled independently in goal seeking or obstacle avoidance tasks.

III.1. Goal Seeking Fuzzy Controller (GSFC)

Reaching a certain goal autonomously is obtained by GSFC. As previously stated, the entire GSFC contains three separate PD-fuzzy sub-controllers as shown in Fig. 4. The three sub-controllers have two inputs, the error *e* and its derivative d*e*/d*t* and one output, which is the change in *H* for the first sub controller, the change in *V* for the second sub controller and the change in ω_c for the third one:

$$\mathbf{e} = \mathbf{R}(-\theta)(\mathbf{q}_{des} - \mathbf{q}) \tag{17}$$

where $\mathbf{R} = \begin{bmatrix} \cos\theta & -\sin\theta & 0 \\ \sin\theta & \cos\theta & 0 \\ 0 & 0 & 1 \end{bmatrix}$ is the rotation matrix, $\mathbf{q}_{des} = \begin{bmatrix} x_d & y_d & \theta_d \end{bmatrix}^T$ is the desired posture vector, and $\mathbf{q}_r = \begin{bmatrix} x & y & \theta \end{bmatrix}^T$ is the posture vector of the omnidirectional wheeled robot. GSFC's rules are designed to update *H*, *V* and ω_c based on changes in error and its derivative at each move. The ranges of the inputs and outputs are normalized to [−1 to 1] range. The error of goal seeking is demonstrated in the body coordinate frame as shown in Fig. 5, and Figs. 6 present the membership functions of *H*, *V*, and ω in GSFC: (a) Membership functions of *e* and the change of *H*, *V*, and (b) Membership functions of d*e*/d*t*.

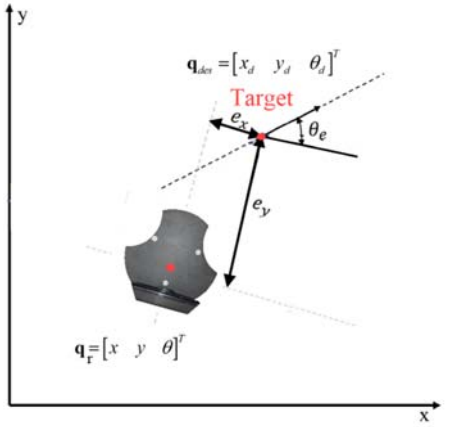

Fig. 5. The error between the mobile robot and target point represented in the body frame

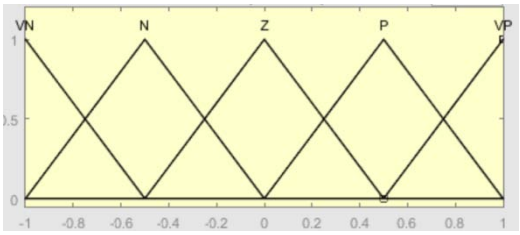

(a)

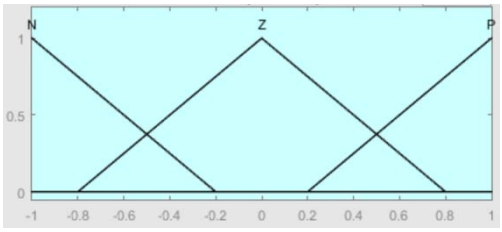

(b)

Figs. 6. The membership functions of H, V, and ω in GSFC. (a) e and the change of H, V and ω_C; (b) The change of e

The ranges of the error, *V*, *H*, and ω vary as Very negative (VN), Negative (N), Zero (Z), Positive (P), and Very positive (VP) in SOAFC, and the range of the change of the error varies as Negative (N), Zero (Z), Positive (P), where all ranges are normalized to [−1 to 1] range.

III.2. Static Obstacle Avoidance Fuzzy Controller (SOAFC)

The fuzzy controller that is used to avoid static obstacles takes into consideration the distance between the robot and the near obstacle. SOAFC has two sub-controllers as shown in Fig. 7, each one has three inputs and one output. The three inputs of the sub-controllers represent the distance between robot and the obstacle, in three regions of the FoV: right, front, and left of the robot that is specified by Kinect sensor. The change in *H* is the output of the first sub-controller and the change in *V* is the output of the second controller. As long as the Kinect sensor detects an obstacle in any of the three regions, the SOAFC starts controlling *H* and *V* to move the robot against the detected obstacle based on the controller membership functions. Once the FoV is clear from obstacles, the system switches to the GSFC and continues eliminating the error. Fig. 8 shows the FoV of Kinect, S is the Kinect's maximum detection range, which is 4.5 m and the distance between the robot and the static obstacle is presented by So. The range of the Kinect distance is between [0 to 4.5] m and the corresponding fuzzy membership varies as Near, Medium, Far for SOAFC. The outputs are provided as Very negative (VN), Negative (N), Zero (Z), Positive (P), and Very positive (VP). The ranges of the inputs are normalized to [0 to 1] range. Figs. 9 present the membership functions of *H* and *V* in SOAFC: (a) The input distance between the robot and the static obstacle in the right, front, and left regions, (b) the change in *H* and *V*.

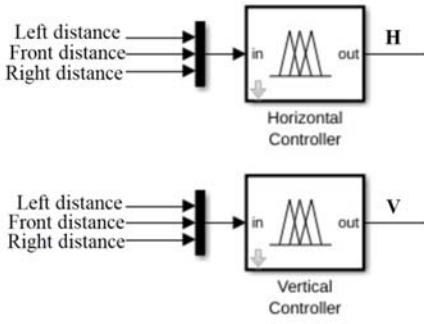

Fig. 7. The SOAFC contains two sub controllers

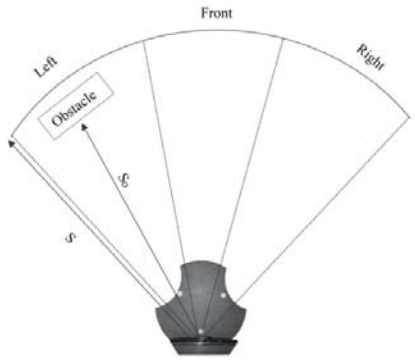

Fig. 8. The Kinect's maximum detecting range and the distance between the robot and the static obstacle

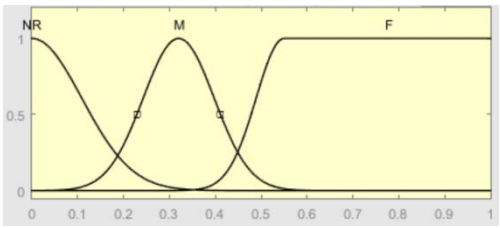

(a)

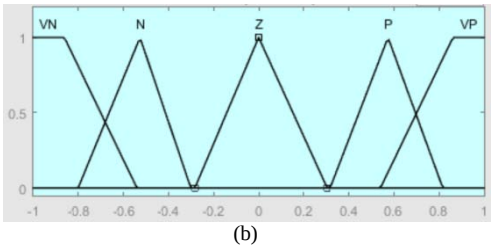

(b)

Figs. 9. Membership functions of H and V in SOAFC (a) The input distance between the robot and the static obstacle in the right, front, and left regions; (b) The change in H and V

III.3. Dynamic Obstacle Avoidance Fuzzy Controller (DOAFC)

DOAFC is responsible to avoid the robot from the dynamic obstacles, where two sub-controllers give the robot the appropriate value of *H* and *V* independently to move away from the dynamic obstacle depending on the distance between the robot and the dynamic obstacle, and its relative velocity. Each sub-controller has six inputs and one output as shown in Fig. 10, the inputs are; the left, front, and right distances between the obstacle and the robot, and the left, front, and right relative velocities between them. The change in *H* is the output of the first sub-controller and the change in *V* is the output of the second sub-controller. As long as the Kinect sensor detects a dynamic obstacle in any of the three regions, the DOAFC starts controlling *H* and *V* to move the robot against the detected obstacle with appropriate speed based on the controller membership functions. Once the FoV is clear from obstacles, the system switches to the GSFC and continues eliminating the error. The second three inputs are the relative velocity between the obstacle and the robot in the right, front, and left regions of the FoV.

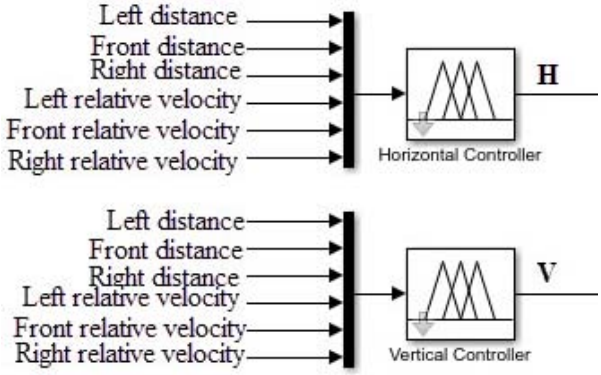

Fig. 10. The DOAFC contains two sub controllers

The dynamic obstacle velocity is calculated using Eq. (12); where v_D is the dynamic obstacle velocity, and as shown in Fig. 11, $d_n(i\text{-}1)$ is the distance between the robot and the dynamic obstacle in n region at specific time, $d_n(i)$ is the distance between the robot and the dynamic obstacle after δt time step:

$$v_D = \frac{d_n(i-1) - d_n(i)}{\delta t} \tag{18}$$

The relative velocity between the robot and object is calculated according to Eq. (13) to be provided to the sub-controllers; where v_R is the robot velocity and v_{DR} is the relative velocity between the robot and the dynamic obstacle:

$$v_{DR} = v_R - v_D \tag{19}$$

The corresponding fuzzy membership varies as Near (NR), Medium (M), and Far (F) for the distance and Slow (S), Medium (M), and Fast (FT) for the relative velocity.

The change in *H* and *V* are provided as Very negative (VN), Negative (N), Zero (Z), Positive (P), and Very positive (VP). The ranges of the inputs are normalized to [0 to 1] range.

Figs. 12 present the membership functions for the horizontal and vertical motions in DOAFC: (a) the membership functions for the input distance between the robot and the dynamic obstacle in the right, front, and left regions; (b) the membership functions for the relative velocity between the robot and the dynamic obstacle in the right, front, and left regions; (c) the membership functions for the changes in *H* and *V*.

IV. System Description

In this study, the robot moves on a flat ground and runs four threads in parallel; going to a desired goal, localizing itself, mapping the environment, and avoiding static and dynamic obstacles.

EKF-SLAM algorithm with static and dynamic obstacles flowchart is presented in Fig. 13, the robot starts seeking a predefined goal using GSFC with an initial position and linear and angular velocities. During its movement, it uses the odemeter as a motion sensor and a Kinect sensor as a visual sensor. The Kinect sensor obtains the data regarding the landmarks and obstacles. If the Kinect sensor detects an obstacle in its FoV, then one of the SOAFC and DOAFC starts working depending on the type of the obstacle. Once the obstacle gets away from the FoV, the system switches the controller back to the GSFC.

As long as the robot moves to the goal, the landmarks and the odometer help the EKF to update the state estimate, where the robot's next state is predicted using the previous state estimate. The robot keeps seeking the goal, localizing itself, updating the map with the extracted features until the end of the mission.

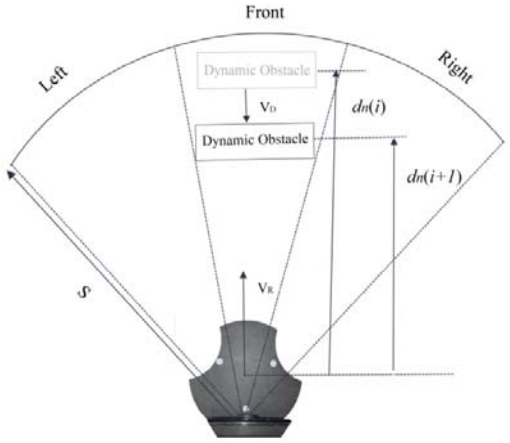

Fig. 11. The relation between the robot and the dynamic obstacle

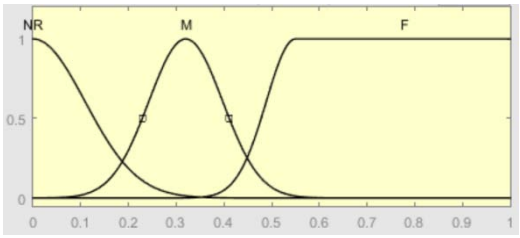

(a)

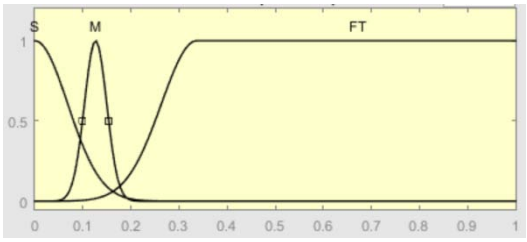

(b)

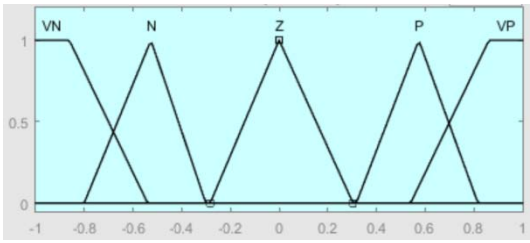

(c)

Figs. 12. The membership functions of of H and V in DOAFC (a) The input distance between the robot and the dynamic obstacle in the right, front, and left regions; (b)The relative velocity between the robot and the dynamic obstacle in the right, front, and left regions;
(c) The change in H and V

V. Experimental Result

The proposed EKF-SLAM algorithm is tested using a real EV3 Lego Omnidirectional robot and a Kinect sensor as a main sensor with static landmarks in the surrounding environment. Three tests are performed to demonstrate the effectiveness of the system; in the first test, the robot reached a goal with absence of landmarks and existence of three static obstacles.

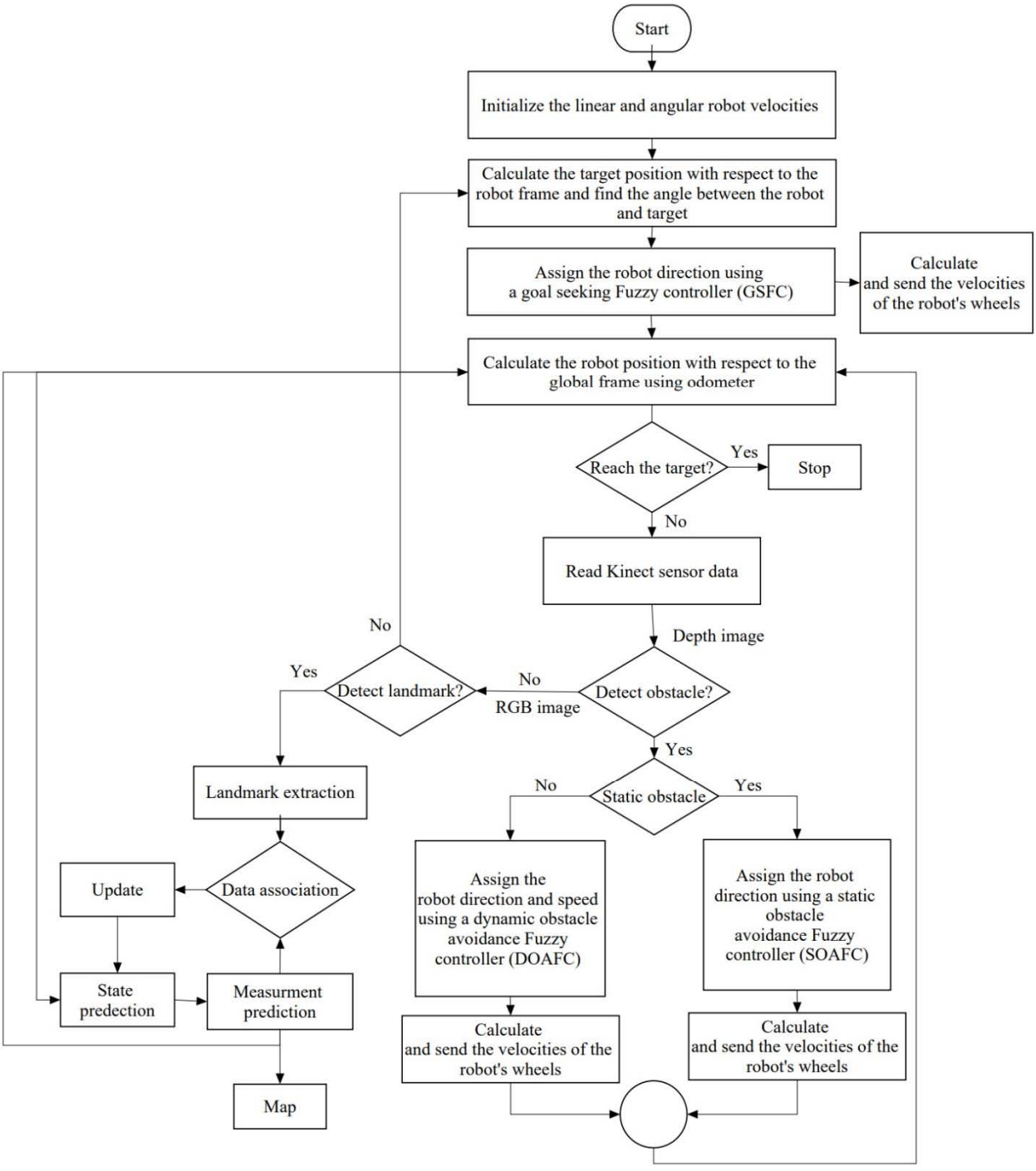

Fig. 13. EKF SLAM algorithm with static and dynamic obstacles flowchart

In the second test, two static landmarks were added to the environment, where the robot was able to localize itself and find collision free path. In the third test, mix of static and dynamic obstacles were added to robot workspace, the robot showed its ability to reach the goal, avoid collision with dynamic obstacles, and produce a map for the environment. The following subsections present the details for each experiment. Figs. 14 show the experimental results with existence of three different static obstacles and absence of landmarks; Fig. 14(a) is the experimental scene, and Fig. 14(b) is the robot path with the extracted map with three static obstacles. Starting at (0,0), the robot moves toward the target point at (4.4, 2.5) m. It starts to find its path to reach the goal point using GSFC, during its path it detects the first obstacle using the depth sensor and switches to SOAFC, it avoids it, generates a new path to the goal, and switches back to GSFC. Another static obstacle faces the robot; the robot uses SOAFC again and avoids it. At the end, it generates the last path to the goal and uses GSFC. Figs. 15 show the

experimental results with existence of three different obstacles and two landmarks; landmarks help the robot to localize itself in the environment. Fig. 15(a) is the experimental scene, and Fig. 15(b) is the robot path with the extracted map with three static obstacles and two landmarks. Starting at (0,0), the robot moves toward the target point at (4.4, 2.5) m, each time the robot faces an obstacle detected by the depth sensor, the system switches the controller to SOAFC until the obstacle is not seen by the Kinect. The robot updates its location each time the Kinect sensor detects a landmark using the RGB camera.

The absolute error and percentage error between the robot and the goal in *H*, *V*, and ω_c with and without existence of landmarks is shown in Table I, where the error is decreased by adding landmarks.

V.1. Dynamic Obstacles Environment

During the robot navigation, the robot keeps switching between GSFC, SOAFC, and, DOAFC. It depends if the Kinect sensor detects static/dynamic obstacle or not. Figs. 16 show the experimental results with existence of three different static obstacles and one dynamic obstacle (A person). Fig. 16(a) is the experimental scene, and Fig. 16(b) is the robot path with the extracted map with three static obstacles and one dynamic obstacle.

(a)

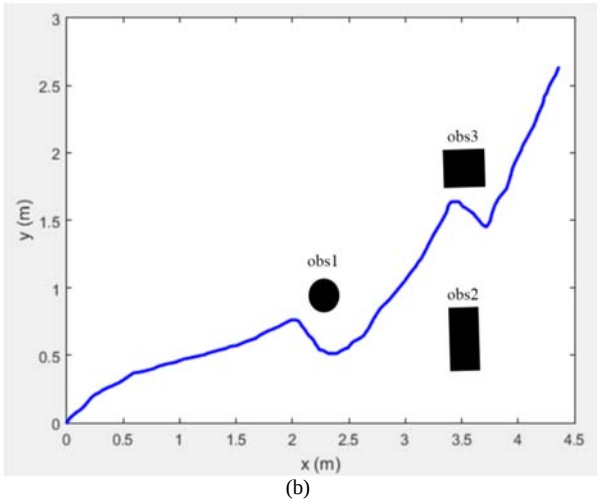

(b)

Figs. 14. The robot path with existence of three different static obstacles and absence of landmarks

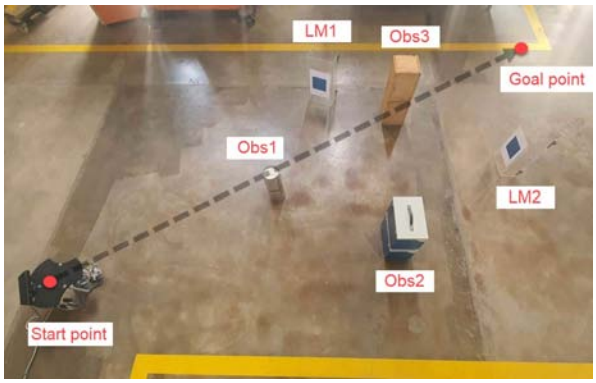

(a)

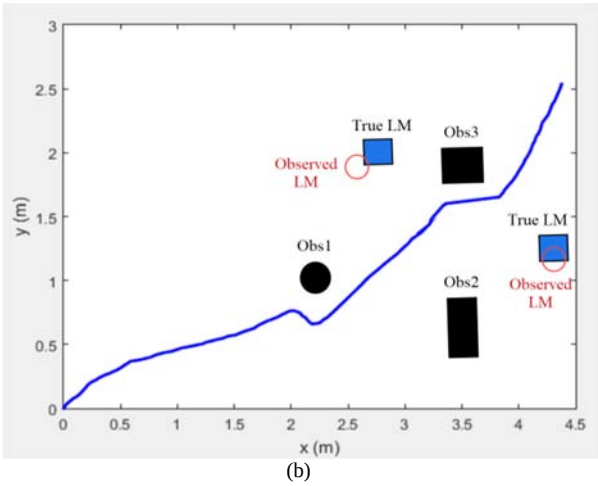

(b)

Figs. 15. The robot bath with existence of three different static obstacles and two landmarks

TABLE I
THE ABSOLUTE ERROR AND PERCENTAGE ERROR BETWEEN THE ROBOT AND THE GOAL IN H, V, AND ω_C WITH EXISTENCE OF STATIC OBSTACLES

	Without landmarks		With landmarks	
	Absolute error	Percentage error %	Absolute error	Percentage error %
H	0.10 m	2.27	0.05 m	1.13
V	0.13 m	5.2	0.03 m	1.2
ω_C	8°	16	6°	12

Starting at (0,0), the robot moves toward the target point at (4.4, 2.5) m with constant speed 0.3 m/s. After a while, the Kinect sensor detects a dynamic obstacle with 0.6 m/s speed, the robot uses DOAFC and changes its direction and speed to avoid the dynamic obstacle. After the dynamic obstacle is not in the FoV of the Kinect, the robot keeps switching between GSFC and SOAFC until it reaches the goal point. The absolute error and percentage error between the robot and the goal in *H*, *V*, and ω_c with the existence of the dynamic obstacle is shown in Table II.

TABLE II
THE ABSOLUTE ERROR AND PERCENTAGE ERROR BETWEEN THE ROBOT AND THE GOAL IN H, V, AND Ω WITH EXISTENCE OF STATIC AND DYNAMIC OBSTACLES AND TWO LANDMARKS.

Motion component	Absolute error	Percentage error %
H	0.03	0.7
V	0.05	2
ω_C	5°	10

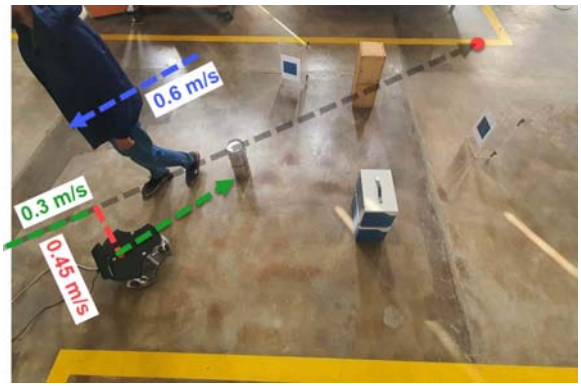

(a)

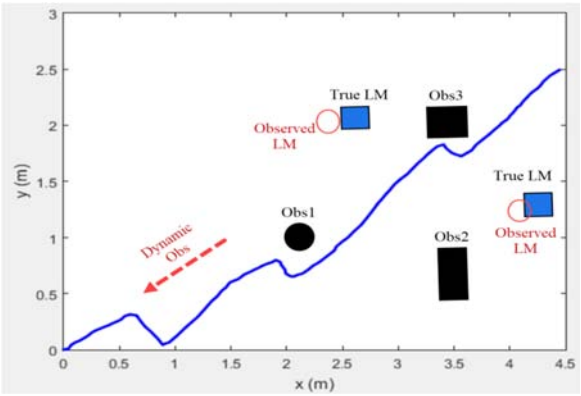

(b)

Figs. 16. The robot bath with existence of static and dynamic obstacles

VI. Discussion

The overall results of this study show that the EKF-SLAM robot can navigate, avoid static and dynamic obstacles, reach a specific goal, and localize itself with unknown landmarks using a Kinect sensor experimentally. The linear and angular velocities of the robot has been controlled separately using the decentralized algorithm, which simplified the control process.

The navigation of the robot has been tested in three scenarios; in the first one, the robot reached a goal with absence of landmarks and existence of three static obstacles. In the second one, two static landmarks were added to the environment, where the robot was able to localize itself and find collision free path. In the third test, mix of static and dynamic obstacles were added to robot workspace with the existence of two static landmarks.

In the three scenarios, the robot could recognize and classify the static and dynamic obstacles using the IR depth sensor of the Kinect sensor and the landmarks using the RGP camera of the Kinect sensor. Avoiding the static and dynamic obstacles, which has been shown in the aforementioned figures, indicates that the three main controllers could control the linear and angular velocities effectively. Accordingly, Table I and Table II have carried out that the error with existence of the landmarks was relatively low despite of the existence of the dynamic obstacles.

VII. Conclusion

This work presented an EKF-SLAM algorithm for Omni-directional robot navigates in an indoor environment, where the omnidirectional-wheeled robot odometry and a Kinect sensor are combined under an unknown environment. The robot reaches a goal with free collusion path, where three main fuzzy controllers are used for the navigation system; goal seeking autonomously using GSFC with three sub-controllers to control H, V, and ω_c independently, static obstacles avoidance using SOAFC with two sub-controllers to control H, V independently, and dynamic obstacles avoidance using DOAFC with two sub-controllers to control H, V independently. The proposed navigation system was tested using a real EV3 Lego robot with various environment of existence and absence of the static and dynamic obstacles and the landmarks. The robot showed its ability to reach the goal, avoid collision with dynamic and static obstacles, and produce a map for the environment. This paper concerns to study the slam technique in an indoor application, likewise, there are various applications in a variety of industries, such as; Autonomous driving and robotics.

Acknowledgements

"This research was funded by the deanship of research at Jordan university of Science and Technology, Grant number 20220196."

References

[1] Tang, M., Chen, Z. & Yin, F. SLAM with Improved Schmidt Orthogonal Unscented Kalman Filter. Int. J. *Control Autom. Syst.* 20, 1327–1335 (2022). doi: https://doi.org/10.1007/s12555-020-0896-5

[2] Do, C.H., Lin, H.Y.: Incorporating neuro-fuzzy with extended Kalman filter for simultaneous localization and mapping. *Int. J. Adv. Rob. Syst.* 16(5), 172988141987464 (2019).

[3] Hammia, S., Hatim, A., Bouaaddi, A., Najoui, M., Jakjoud, F., Ez-ziymi, S., Efficient EKF-SLAM's Jacobian Matrices Hardware Architecture and its FPGA Implementation, (2021) *International Review of Electrical Engineering (IREE)*, 16 (5), pp. 484-496. doi:https://doi.org/10.15866/iree.v16i5.20149

[4] D. Talwar and S. Jung, Particle Filter-based Localization of a Mobile Robot by Using a Single Lidar Sensor under SLAM in ROS Environment, 2019 *19th International Conference on Control, Automation and Systems (ICCAS)*, 2019, pp. 1112-1115. doi: 10.23919/ICCAS47443.2019.8971555

[5] M. Montemerlo, S. Thrun, D. Koller, and B. Wegbreit, Fast SLAM 2.0: An Improved Particle Filtering Algorithm for Simultaneous Localization and Mapping, *Proceedings of IJCAI*, 2003.

[6] J. J. Leonard and H. F. Durrant-Whyte, Mobile robot localization by tracking geometric beacons, *Robotics and Automation, IEEE Transactions*, vol. 7, pp. 376-382, 1991.

[7] M. Montemerlo, S. Thrun, D. Koller, and B. Wegbreit, FastSLAM: A Factored Solution to the Simultaneous Localization and Mapping Problem, *In Eighteenth national conference on Artificial intelligence*, Menlo Park, CA, USA, 2002, pp. 593-598.

[8] Esparza-Jiménez, J.O.; Devy, M.; Gordillo, J.L. Visual EKF-SLAM from Heterogeneous Landmarks. *Sensors* 2016, 16, 489. doi: https://doi.org/10.3390/s16040489

[9] Pei, F-J, Wu, M., Zhang, S.: Distributed SLAM Using Improved Particle Filter for Mobile Robot Localization, *The Scientific World*

Journal, 86, Paper, (2014).
doi: https://doi.org/10.1155/2014/239531
[10] Karam, S.; Lehtola, V.; Vosselman, G. Strategies to Integrate IMU and LIDAR SLAM for Indoor Mapping. *ISPRS Ann. Photogramm. Remote Sens. Spat. Inf. Sci.* 2020, *V-1*–2020, 223–230.
[11] Karam, S.; Nex, F.; Chidura, B.T.; Kerle, N. Microdrone-Based Indoor Mapping with Graph SLAM. *Drones* 2022, *6*, 352.
[12] Kim, H.; Kim, D.; Kim, S. Real-time Geospatial Positioning for UAVs in GPS-Denied Environment Using LiDAR Data. In *Proceedings of the AIAA Scitech 2020 Forum*, Orlando, FL, USA, 6–10 January 2020; p. 2194.
[13] El Farnane, A., Youssefi, M., Mouhsen, A., Kachmar, M., Oumouh, A., El Aissaoui, A., Trajectory Tracking of Autonomous Driving Tricycle Robot with Fuzzy Control, (2022) *International Review of Automatic Control (IREACO)*, 15 (2), pp. 80-86.
doi: https://doi.org/10.15866/ireaco.v15i2.21719
[14] Batayneh, W., Bataineh, A., Jaradat, M., Intelligent Adaptive Fuzzy Logic Genetic Algorithm Controller for Anti-Lock Braking System, (2021) *International Review on Modelling and Simulations (IREMOS)*, 14 (1), pp. 44-54.
doi: https://doi.org/10.15866/iremos.v14i1.19838
[15] Bataineh, A., Batayneh, W., Okour, M., Intelligent Control Strategies for Three Degree of Freedom Active Suspension System, (2021) *International Review of Automatic Control (IREACO)*, 14 (1), pp. 17-27.
doi: https://doi.org/10.15866/ireaco.v14i1.20057
[16] Batayneh, W.; AbuRmaileh, Y. Decentralized Motion Control for Omnidirectional Wheelchair Tracking Error Elimination Using PD-Fuzzy-P and GA-PID Controllers. *Sensors* 2020, 20, 3525.
doi: https://doi.org/10.3390/s20123525
[17] Batayneh, W., Aburmaileh, Y., Bataineh, A., Experimental Implementation of Tracking Error Elimination for Omnidirectional Wheelchair Using PD-Fuzzy-P Controller, (2021) *International Review of Automatic Control (IREACO)*, 14 (2), pp. 102-112.
doi: https://doi.org/10.15866/ireaco.v14i2.20654
[18] N. V. Belov, D. P. Airapetov, B. Y. Buyanov and V. A. Verba, SLAM Implementation For Mobile Robots Using Physical Sensors, *Systems of Signals Generating and Processing in the Field of on Board Communications*, 2019, pp. 1-6.
doi: 10.1109/SOSG.2019.8706786
[19] M. Kulkarni, P. Junare, M. Deshmukh and P. P. Rege, Visual SLAM Combined with Object Detection for Autonomous Indoor Navigation Using Kinect V2 and ROS, *2021 IEEE 6th International Conference on Computing, Communication and Automation* (ICCCA), 2021, pp. 478-482.
doi: 10.1109/ICCCA52192.2021.9666426
[20] Ganiev, A., & Lee, K. H. (2018). A study of autonomous navigation of a robot model based on SLAM, ROS, and kinect. *International Journal of Engineering and Technology (UAE)*, 7(3.33), 28-32.
[21] Cho, H.; Yeon, S.; Choi, H.; Doh, N. Detection and Compensation of Degeneracy Cases for IMU-Kinect Integrated Continuous SLAM with Plane Features. *Sensors* 2018, 18, 935.
doi: https://doi.org/10.3390/s18040935

Authors' information

[1]Mechanical Engineering Department, Jordan University of Science and Technology, Irbid, Jordan.

[2]Department of Electrical and Computer Engineering, Iowa State University, Ames, Iowa, USA.

Wafa Batayneh (Corresponding Author) is a Mechanical Engineering professor at Jordan University of Science and Technology. She received her PhD and master degrees from Rensselaer Polytechnic Institute, Troy, NY, USA in 2005. Her areas of interest include mechanical design, robotics, mechatronics systems design and embedded control systems. During her integrated experience, she has several research projects, prototypes, awards, patent and publications in these areas, where she is an author and coauthor of more than thirty five journals and conferences publications. Prof. Batayneh has received several national awards in recognition of her achievements.

Yusra Aburmaileh received the B.Sc. degree in Mechatronics engineering from Hashemite University, Zarqa, Jordan, in 2015 and M.Sc. degree in Mechanical/Mechatronics engineering from Jordan University of Science and Technology (JUST), Irbid, Jordan, in 2019. She is working in the Mechatronics Research Laboratory at JUST. Her current and previous research interests include robotics, Artificial Intelligence, and control systems.

Ahmad Bataineh is an associate professor of Mechanical Engineering at Jordan University of Science and Technology (JUST). Dr. Bataineh earned his PhD in Mechanical Engineering from State University of New York at Binghamton (SUNY Binghamton). He joined JUST in September 2014, His research interests are in the area of Mechatronics System Integration and Application, Artificial Intelligent Applications, Characterization of Micro-Electro Mechanical Systems (MEMS). He has more than 20 publications in these areas as an author and co-author in journals and conferences.

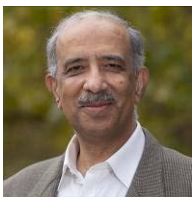

Ashfaq Khokhar is currently Professor & Palmer Department Chair of the Department of Electrical and Computer Engineering at Iowa State University. He previously served as Chair and Professor in the Department of Electrical and Computer Engineering at the Illinois Institute of Technology in Chicago, Illinois. He has also served as Professor and Director of Graduate Studies in the Department of Electrical and Computer Engineering at the University of Illinois, Chicago. Dr. Khokhar has received various types of scholarly recognition and awards, including the NSF CAREER Award in 1998 for his work on multi-threaded algorithms for multimedia applications. In 1996, he won an Outstanding Paper Award for his presentation at the International Conference on Parallel Processing. He has served as associate editor on the editorial board of numerous journals. Khokhar was elected an Institute of Electrical and Electronics Engineers (IEEE) Fellow in 2009 for his work on multimedia computing and databases, and he is a member of the Honor's Society Phi Kappa Phi.

International Review of Automatic Control (I.RE.A.CO.), Vol. 16, N. 2
ISSN 1974-6059 March 2023

Review of Computerized Prosthetic Knee Joints in Terms of Mechanical and Control Design

Ahmed Khaleel Abdulameer, Mohsin Abdullah Al-Shammari

Abstract – *The computerized prosthetic knee joints equipped with advanced embedded systems that enable control of lower limb movements for amputees using hardware and software components. The hardware of the embedded system represents each of the actuators, sensors, and microcontrollers while the software uses algorithms of artificial intelligence that control movements of the knee joint by a microcontroller that receives the input signal from sensors and transmits it to the actuator to conduct the required motion. An overview comprehensive will be presented of everything related to the mechanical and control design of computerized prosthetic knee joints by exploring the complete mechanical design, including mechanisms, materials, actuators, numerical analysis, and control design, including, sensing system, control method, and microcontroller, this paper fills a gap in the existing literature and offers a more comprehensive understanding of the field, unlike the available recent review articles related to the smart prosthetic knee joints that have typically focused on individual aspects, such as specific actuators or control methods for active prosthetic knee joints. A systematic approach was followed. A group of relevant papers was selected, covering the period up to October 2022. Then, these papers were categorized based on the mechanical and control design aspects of smart prosthesis. This paper will be given a complete image for all researchers interested in prosthetics, especially intelligent prosthesis for all used actuators, sensory system, microcontrollers and opinions of previous authors related to numerical analysis thus they will enrich the researchers and will be a starting point for future works.*

Keywords: *Computerized Prosthetic Knee Joint, Powered Knee, Mechanical Design, Powered Actuators, Variable Damping Actuator*

I. Introduction

Lower limb amputations can result from various causes, including traumatic, dysvascular, oncological disorders, infections, and even security issues in some countries [1]-[3]. Transfemoral amputees require a prosthetic knee, shank, ankle joint, and foot to replace the missing part of the thigh, making research related to prosthetic knee joints crucial. The knee joint plays a crucial role in daily locomotion by coordinating muscles, bones, ligaments, and other parts [4]. However, above-knee amputees lack this joint, which affects their ability to stand, sit, or walk. Prosthetic knee joints can be classified into three groups: passive, active-damping-controlled, and power-controlled [5] as shown in Figure 1. This review focuses on active damping controlled and power-controlled prosthetic knee joints. Variable-damping-controlled knees, which use hydraulic, pneumatic, or magneto-rheological dampers as actuators and microcontrollers to mimic the role of the musculoskeletal system during various activities, are the most common knee prostheses worldwide [6]. Power-controlled prostheses, such as the fully powered Power Knee produced by össur, use brushless DC motors or pneumatic actuators [7]-[8].

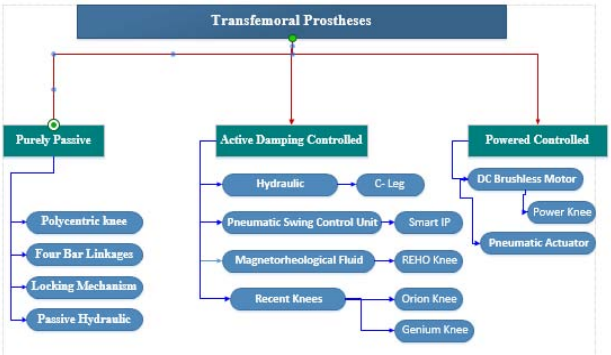

Fig. 1. Categories of above-knee prostheses

The performance of prosthetic knees depends on factors such as actuators, mechanical design, and control methods (including sensing systems, algorithms, and machine learning) [9]-[10]. There are numerous scientific focused on active and semi-active prosthetic knee joints, most of them studied the mechanical and control design of microprocessor prosthetic knee joints, with a greater emphasis on sensing systems, algorithms, and machine learning rather than mechanical design. some researchers designed and manufactured a smart prosthetic knee joint using different metals with various actuators and

 https://doi.org/10.15866/ireaco.v16i2.23412

mechanisms [11]-[12], where they used the finite element method that has an important effect on the design of prosthetic limbs [13]. while others have used a DC motor through a ball screw to create a mono-centric prosthetic knee joint [14]-[15]. Some researchers have focused on sensing systems to restore the necessary motion for daily living activities based on the patient's intent [16]-[17].

This review provides a comprehensive overview of smart and semi-active prosthetic knee joints, including their mechanisms, materials, actuators, and control methods up to October 2022. The aim is to assist researchers and engineers working in prosthetics and orthotics engineering with their future work.

The structure of this paper will be as follows. Section II briefly classifies computerized prosthetic knee joints based on their structure, actuators, electronic circuits, and control methods. Section III includes future works and evaluations, while Section IV presents the conclusions.

The paper also discusses the state-of-the-art related to microprocessor prosthetic knee joints.

II. Methods

This paper offers a comprehensive review of computerized prosthetic knee joints, covering both active and semi-active types, including their mechanisms, materials, actuators, and control methods. Unlike previous review articles that have focused solely on individual actuators and control methods for active prosthetic knee joints [12], [18]-[20], this review categorizes included papers and theses into two main areas: mechanical design, which includes actuators, materials, numerical analysis, and mechanisms; and control design, which encompasses sensing systems, electronic systems, and control methods.

II.1. Mechanical Design

Designing a smart prosthetic knee joint requires careful consideration of various factors, including the actuator type (powered, variable damping, or passive) and mechanism (single-axis or poly-centric). The appropriate actuator should be selected based on the identified joint type. The mechanical design should prioritize dimensions, weight, strength, range of motion, speed, cost, fatigue life, quality, and aesthetic value.

Actuators, materials, mechanisms, and numerical analysis are critical components of the design of microchip prosthetic knee joints, and the length of the user's leg should also be considered.

II.1.1. Actuators

Actuators used in prosthetics can be classified into three categories: passive (damper and spring), active variable-damping (hydraulic, pneumatic, and magneto-rheological damper), and powered (active) (such as a rigid actuator, pneumatic artificial muscles, and series elastic actuator). An actuator with elastic properties is typically preferred, as it compensates for energy loss during motion and improves body balance. The selection of the appropriate actuator type should be based on the amputee's activity level, with an active actuator being more crucial during activities such as the stair ascending.

This review focuses on active and active variable-damping actuators, which are essential components in the production of smart prosthetics, while passive actuators will be overlooked.

II.1.1.1. Active Actuators

Active actuators in prosthetics are fully powered electro-mechanical actuation systems, and they can be classified into three categories: rigid actuators, Serial Elastic Actuators (SEA), and pneumatic artificial actuators [21]. The serial elastic actuator utilizes an elastic mechanism in combination with a small motor mass to reduce impact force and enhance force control during gait assistance [22], while the Pneumatic Artificial Muscle (PAM) is a pneumatically-powered actuator and stands out from other actuator categories. The power knee developed by Össur Corporation is the only commercially available active prosthetic knee joint that employs a serial elastic actuator. Selecting the appropriate actuator for an active prosthetic knee joint requires the calculation of five parameters: maximum peak torque, maximum speed, maximum position, rated torque, and inertia [23]. Among the rigid actuators, the electro-mechanical system that includes a motor connected with a ball screw is commonly used. Kamel et al., utilized a linear actuator from ULTRAMOTION Corporation, while Al-Maliky et al., used a ball screw (ISSOKU GTR0802) with a brushless motor (EC-i40 130-watt) from Maxon, and Hoover et al., utilized a ball screw (Nook ECS-10020-RA) with a 150-watt brushed DC motor (Maxon RE40) [24]-[26]. These actuators are heavy and lengthy, which can have a negative impact on the weight and height of smart prosthetic knee joints. As a result, they are mainly used for single-axis mechanisms. In the design of prosthetic knee joints, the choice of the actuator is crucial and can greatly affect the performance of the device. The researchers employed several types of actuators to power prosthetic knee joints.

El-Sayed et al utilized a high-torque Maxon spindle drive motor with a gear ratio of 492:1, while Jo et al designed a similar structure using a DC motor and a ball screw [27],[28]. Liu et al used a Maxon DC motor with a ball screw weighing 480g, and Borjian et al., employed a brushed motor connected to a parallel belt driven by a ball screw mechanism [16],[29]. Valencia et al used a low-cost electric linear actuator manufactured by Progressive Automations with a stroke length of 2 inches and a force of 50 lbs. powered with 12 DC, but it required a high current with a full load and thus needed a battery with high ampere-hours and high weight for a smart prosthetic knee joint [30]. Other researchers used various types of actuators; rigid and elastic actuators that being a popular choice. The rigid actuator typically

includes an electro-mechanical system with a motor connected to a worm gear or driver shaft mechanism. For instance, Islam et al., utilized a worm wheel as a knee joint actuator, with the gear deriving motion from the motor through meshed gears [31]. Another example is Kadhim et al., who employed a DC motor (BOSCH) as an actuator with the rack and pinion mechanism, where the pinion moves the rack within the actuator parts [11].

On the other hand, serial elastic actuators are a second category of active actuators that include an elastic element combined with the motor. Martinez-Villalpando et al., suggested an agonist-antagonist array consisting of two series of elastic actuators in parallel around the knee axis, where one of them acts in flexion and the other in extension [32]. Rouse et al., developed a Clutch-able Series Elastic Actuator (CSEA) that precisely controls the force and protects the motor transmission system from shock loads [33]. Jannati et al., designed a series of elastic actuators for active prosthetic knees using a motor that transferred its output power to a ball screw through a timing belt and pulley [34]. Finally, Peng et al., created a Variable Stiffness Actuator (VSA) using two motors, with the first driving the knee joint to rotate and the second providing stiffness-regulating motion [35]. These studies demonstrate the potential of different types of rigid and elastic actuators in the design of prosthetic legs, each with its unique advantages and limitations. The third type of actuator commonly used in prosthetic knee joints is pneumatic artificial muscles, which mimic biological muscles and generate force through radial expansion and axial contraction when pressurized with compressed air. These muscles can be classified into four types based on their construction, with the braided pneumatic muscle being the most common [36].

Commercially available McKibben muscles, produced by companies such as Shadow and FESTO, are also widely used in varying lengths and diameters. Dabiri et al., [37] incorporated two Festo pneumatic muscles (MAS-40) as actuators in their powered prosthetic knee joint design, which were attached to the thigh and shin with brackets and eye bolts, respectively. This design required external compressed air from a compressor to operate, as depicted in Figure 2.

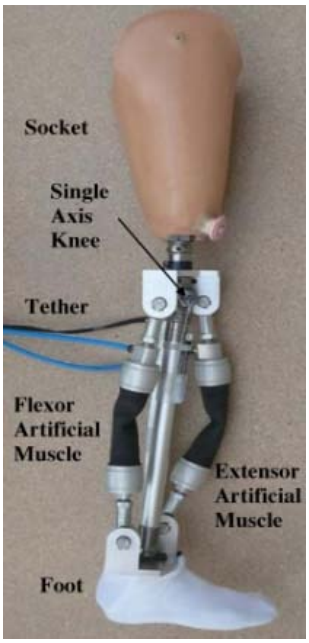

Fig. 2. Powered prosthetic knee joint using pneumatic muscles [37]

II.1.1.2. Variable-Damping Actuators

Variable-damping actuators are a class of devices that can adjust the amount of energy they dissipate by consuming low power. They can be categorized into three types, namely hydraulic, pneumatic, and magneto-rheological (MR). Active variable-damping actuators, which incorporate smart materials, provide a controllable damping force or torque and are divided into two groups, linear and rotary MR actuators [38]. While active actuators used in powered transfemoral prostheses can provide suitable torque for driving and controlling the desired motion during walking, they have deficiencies such as high energy consumption, decreased battery life, increased weight, and potential instability.

On the other hand, variable-damping actuators, such as those utilizing magneto-rheological fluid, require low power consumption and can respond to changes in walking speeds and motion patterns, providing a more natural walking experience for amputees [17]. Bram et al., designed an electrohydraulic damper with two separate hydraulic modes of operation, an active mode using a pump, and a passive mode controlling a variable position valve [39]. Wang et al., proposed a novel solution that utilizes an active variable-damping actuator with valves controlling the flow of hydraulic oil [40].

Similarly, Cao et al., used the same hydraulic variable damping actuator in an intelligent prosthetic knee joint, where a single motor was used to control the hydraulic cylinder and modulate the damping properties [17]. Cao et al., also utilized a hydraulic damper with two separate needle valves controlled by a linear motor to produce joint resistance for flexion and extension locomotion [41]. In another study, Dedić et al., used hydraulic cylinders from SMC company and an electric motor and hydraulic pump from JUNG company to control the hydraulic cylinder for the prototype of an intelligent prosthetic knee joint [42]. By utilizing these advanced technologies, researchers are constantly striving to develop improved variable-damping actuators to enhance the performance of prosthetic limbs. Pillai et al., utilized two linear hydraulic actuators connected to a single electric motor-driven pump to design a semi-active smart prosthetic knee-ankle joint [43]. Meanwhile, pneumatic actuators can be classified into two types: Pneumatic Artificial Muscles (PAM) and pneumatic actuators.

Although pneumatic actuators have low costs, they cannot withstand high loads compared to hydraulic actuators, generate high noise, and require a compressor for control, which affects the weight and volume of the smart prosthetic knee joint [24]. To produce (2270 N) of

outward axial force and (2070 N) on the return, Sup et al., employed double-acting pneumatic actuators with the model (17-3-DP) for the knee joint and model (17-2.75-DP) for the ankle joint, which manufactured by Bimba company [8][44]. On the other hand, Orhanlı et al., used an electronically controlled pneumatic actuator designed by Akdoğan to manufacture the smart prosthetic knee joint with a mono-centric joint design [45]. Magneto-rheological fluid has been widely investigated as an adaptive actuator for rehabilitation applications in amputees, particularly for prosthetic ankle/knee using MR dampers that enable control over damping and stiffness characteristics [46]. The operational modes of magneto-rheological fluid can be classified into three modes: flow mode (valve mode), shear mode (clutch mode), and squeeze mode. Magneto-rheological dampers can be classified into two types: linear and rotary, based on the motion of the piston. Linear MR dampers are further categorized into mono-tube, twin-tube, and double-ended types, with mono-tube being the most commonly used. Rotary MR dampers can be divided into the continuous angle and limited angle types. Linear MR dampers operate in valve mode, while rotary MR dampers work in shear mode. The controllability of damping force in MR dampers is achieved by changing the applied magnetic field, which induces polarization in suspended particles, causing chains of particles to form and limiting movement of the MR fluid, resulting in increased viscosity and damping [46]. Carlson et al., were the first to use mono-tube MR damper in the design and manufacturing of smart prosthetic knee joints. In addition, Nandi et al., utilized a magneto-rheological damper for knee actuation in prosthetics, with a peak-to-peak damping force of 2224 N, maximum operating temperature of -71 °C, and a response time of less than 25 ms [47]-[48]. These studies demonstrate the potential of MR dampers for use in smart prosthetic knee joints, providing effective control over damping and stiffness characteristics. Various researchers have utilized MR dampers in the design and manufacturing of smart prosthetic knee and ankle joints. Li et al., developed an intelligent bionic leg (Polycentric) using the RD-1005-3 MR damper manufactured by LORD Corporation, chosen for its advantages similar to the properties of ligament and muscle [49]. Ochoa-Diaz et al., designed and manufactured a polycentric smart knee joint utilizing the RD-8040-1 MR damper manufactured by LORD, which offers controllable damping force, rapid response, and lower power consumption [50]. Arteaga et al., developed a mono-tube MR damper for manufacturing smart prosthetic knee/ankle joints using magneto-rheological fluid type (140 CG) produced by LORD Corporation, with a maximum damping force of 2500 N, an outer diameter of the cylinder of 42 mm, and a stroke length of 20 mm [51]. Shastry et al., designed a smart prosthetic leg (Four-bar mechanism) using a twin-tube MR damper that utilized commercially available magneto-rheological fluid (140CG) [52]. Akalın et al., designed an intelligent prosthetic knee joint (Single-axis mechanism) using a mono-tube MR damper as the actuator and conducted a comparison between the magneto-rheological prosthetic knee and the pneumatic prosthetic knee [53]. Rotary MR dampers have also been utilized in the design of smart prosthetic knee joints.

Össur company used a rotary MR damper with similar working principles to the MR brake to manufacture a smart prosthetic knee. Kim et al., designed a rotary MR brake, consisting of a rotary cylinder filled with magneto-rheological fluid and two connected ports, utilizing the pressure drops in the duct as a force of resistance [54]. Herr et al., suggested a user-adaptive MR knee prosthesis actuated using a magneto-rheological brake and compared it with a non-adaptive knee prosthesis in terms of its clinical effects [55].

Gudmundsson et al., optimized the geometrical design of the MR brake, achieving a maximum braking torque of 61 N m using a field-induced method [56]. In summary, the above-mentioned actuators can be chosen and improved or combined to develop a smart prosthetic knee joint, giving researchers more options to design and manufacture better devices.

II.1.2. Materials

The weight of a smart prosthetic knee is an important design consideration, and the materials used to manufacture the frame and hinge must satisfy specific requirements, including high strength, lightweight, low cost, and availability in the researcher's country. Metals and composite materials are commonly used for fabrication, with aluminum alloys, titanium alloys, and stainless steel being the most commonly used metals, while the choice of composite materials depends on the type of fibers and resin used, as well as the number of fiber layers. Parameters such as strength-to-weight ratio and stiffness-to-weight ratio are critical in prosthetic design [57]-[60]. Various researchers have employed different materials to design smart prosthetic knee joints.

Kadhim et al., used aluminum alloys (Al 7075 and Al 6061) and steel alloy (AISI 4130) to manufacture the hinge and discovered that aluminum alloy (Al 6061) was the best metal for their design due to its stability, comfort, and low cost [11]. Similarly, Lim et al., used aluminum alloy (Al 6061) to design and fabricate the tibial shell (frame) and the hinge of an active prosthetic knee that was satisfactorily light and agile [61]. Kamel et al., and Rupar et al., chose aluminum alloy (Al 2024 T3) to manufacture an intelligent prosthetic knee joint because of its superior properties in terms of lightweight, high strength, low cost, and high quality [24]. Sayem et al., made all components of the prosthetic knee using aluminum alloy (Al 1060-H16), except for the ball bearing, sleeve bearing, and bushing pin [62]. Wu et al., designed an active prosthetic knee using PAM as an actuator and proposed to use the aluminum alloy (Al 2014 T6) to manufacture the frame and hinge [63].

Lambrecht et al., used two types of materials in the design of a smart prosthetic knee, utilizing a carbon

fiber-reinforced material for the frame and an unknown type of aluminum alloy for the hinge [39]. Torrealba et al., manufactured prosthetic knee joints using aluminum plates for the frame, which were arranged to fit the internal surface of an ABS cover [64]. Aluminum alloy is a frequently utilized material in the production of prosthetic knee joints due to its affordability, widespread availability, and favorable physical and mechanical properties, as noted in numerous prior publications in this field, and supported by the findings of the various researchers mentioned above.

II.1.3. Numerical Analysis and Mechanism

The mechanical design process relies on three key tools: Computer-Aided Design (CAD), Computer-Aided Engineering (CAE), and Computer-Aided Manufacturing (CAM). These technologies have revolutionized the manufacturing process by allowing complex objects to be designed and produced quickly. In this section, numerical analysis of prosthetic knee structures will be examined, including mechanisms and boundary conditions, and discuss how these legs must be able to withstand the stresses of walking and other activities. To test the structural integrity of single-axis prosthetic knees, some researchers simulated uniaxial compression loads using the finite element method for static analysis. The load was applied perpendicularly to the pyramid adapter that connects the knee joint (hinge) with the socket, with values equal to the amputee's body weight or three times that weight with a safety factor, at zero knee angle. The sagittal and frontal forces were ignored due to their lower magnitude compared to the axial force, and the bottom of the frame was fixed. [11], [30], [65]-[67]. Another group of researchers analyzed the frame of a mono-centric prosthetic knee joint using ANSYS software, conducting a static analysis with an axial compression load applied perpendicularly to the pyramid adapter. The load was tested at various knee angles (0°, 30°, 45°, 60°, 90°, and 110°), with the bottom of the frame fixed. The researchers discovered that the maximum stress occurred at a 110° knee joint angle [24]. Lim et al. used actual data from Winter's investigation of a male subject weighing 56.7 kg to design an active prosthetic knee.

They applied boundary conditions by subjecting the knee joint to compression axial load and moment for 21 frames, with the greatest force occurring at frame 17.

They discovered that the ball screw joint was the weakest component during their analysis [61]. So far in the review, all mechanical design subjects have been considered based on published papers, except for determining the dimensions of the frame and knee joint. None of the papers provide information on how to define these dimensions.

II.2. Design of Control System

A smart prosthetic knee joint comprises hardware components like an actuator, sensors, microcontroller, and software for information processing. The hardware functions as muscles, nerves, and brain, while software controls the prosthesis. The sensors are inputs for the controller, and the commands are outputs to the actuator.

The prosthesis's behavior depends on the sensing system and control methods, which can be classified into common five methods, including classical, force-based control method, adaptive, bioelectrical signal-based control methods, and hybrid control methods. There are five types of sensors used in prosthetics for efficient control of the smart prosthetic knee joint.

II.2.1. Sensing System

Smart prosthetic knee joints use sensory systems to detect the user's activities and phases of the gait cycle. The sensing system generates data, including kinematic and kinetic information, for the controller algorithm to process. Prosthetics use five groups of sensors, including EMG, inertial, force, fluid pressure, and positioning sensors. These sensors are typically combined to match the actuator and the applied control. Bioelectrical signals from muscles are detected by EMG sensors, which allow for predictive control. Surface electrodes are preferred over needle electrodes because they are easy to use and do not cause pain [68]. EMG sensors have been used in various applications such as identifying walking patterns on different terrains, controlling active prosthetic knees, actuating bionic prosthetic knees, and controlling robotic legs for sitting and standing actions [69]-[72]. Inertial Measurement Units (IMUs) containing accelerometers, gyroscopes, and magnetometers are used as a second type of sensor in smart prosthetic knees to provide gait cycle data during both stance and swing phases [39], [50], [73]-[75]. Force sensors, including load cells and Force-Sensitive Resistors (FSR), are used to measure variables related to ground reaction force during weight-bearing, particularly during the stance phase of the gait cycle [28], [76]-[78]. Fluid pressure sensors are used on the hydraulic cylinder to regulate the knee at a specific torque [39]. Finally, positioning sensors, such as encoders, are used to measure the motion or location of an object relative to a specific reference point, with the most straightforward sensor being an encoder for measuring the knee angle [28], [79]-[81].

II.2.2. Control Methods

In designing an embedded system, selecting the appropriate microcontroller and software is crucial to achieving the desired function of the system. The performance of the final system relies heavily on the sensors utilized to link the interaction between the hardware and software components. Control methods for smart prosthetic knee joints can be broadly classified into five categories, and finite-state machines are often used as a mathematical model in many of these methods. Sup et al., used impedance control (force-based control method), which enables stable interaction between the

knee prosthesis and its environment, where it controls the torque at each joint during a stance phase. They used finite state machines that have been successfully integrated with various types of controllers, mainly impedance controllers by classifying the gait cycle into four essential finite states [44], while Dabiri et al., utilized the finite state machine by segmenting the gait cycle into seven modes to control the motion of a powered prosthetic knee joint based on the contact of the foot with the floor and the sign of the velocity of knee flexion, but they did not mention the type of control method that used [37]. Kamel et al., utilized the PID control algorithm (classical control method) to control powered knee prosthesis using a finite-state machine dividing the gait cycle into five modes [24]. It should be noted that FSMs as a mathematical model compatible with various types of controllers, with impedance controllers being the most common choice. Merewether and Hsieh utilized a position control method during the swing phase and an impedance control method (Hybrid control method) during the stance phase using a linear force-position relationship provided by the series elastic actuator [81]. Herr et al., used used-adaptive control (adaptive control method) to control the semi-active prosthetic knee during the swing phase, and they found that controlled maximum swing flexion angle to satisfactory biological limits [82]. Lawson et al., proposed a hybrid control method that combined piecewise-passive impedance-based control and high-impedance trajectory-tracking control, they noted that using this hybrid control method to control powered prosthetic knee joint during the terminal stance and swing phase, was effective in creating a more natural and efficient gait for the amputee subjects [83]. Ekkachai et al., developed neural network predicative control (hybrid control method) to control of semi-active prosthetic knee during the swing phase at different walking speeds, they discovered that this approach after optimization using a genetic algorithm is better that user-adaptive method and can mimic the knee trajectory for the healthy gait [84].

Fu et al., proposed a sliding mode trajectory tracking control (nonlinear control), which showed good control impact and robustness for prosthetic knee during swing phase in simulation results [85]. Sharma et al., used a hybrid control method that combined fuzzy logic control and PID control to analyze the performance of tracking control of human gait, they found that FLC-PID control method outperform of PID controller [86], also and Nordinet al., utilized FLC-PID control method to control of MR damper based prosthetic knee [87]. Raheema et al., utilized hybrid control method that combines the (PID) controller with the Adaptive Neuro-Fuzzy Inference System (ANFIS) to control of knee prosthesis, they showed that its excellent response and accepted stable performance [88]. Kevin et al., used myoelectric control method (adaptive control method) where the found that this method provide same movement pattern as a healthy knee joint [89]. Huang et al., employed electromyography signal control (Bioelectrical signal-based control methods), where this type does not always effective in the swing phase of gait, which can lead to instability and falls [90].

II.2.3. Microcontroller

Microcontrollers are programmable devices that play a crucial role in controlling and coordinating various components of embedded systems, including prosthetic devices. It provides advanced control systems and artificial intelligence algorithms that enable human-like bionic lower limb control, improve walking speed, gait symmetry, obstacle negotiation, and reduced stumbles and falls compared to non-microcontroller-based prosthetic knees. From the above benefits, it lies the importance to study and choose the appropriate microcontroller used in prosthetic knee joint. Choosing the appropriate microcontroller for an intelligent or smart prosthetic knee joint depends on several factors, such as the number of input/output requirements, memory requirements, communication capabilities, and processing power. The common microcontrollers that used in control design of intelligent prosthetic knee joint; Arduino mega 2560, Raspberry Pi, Teensy 4.1, PIC microcontroller, STM32, and ESP32. The popularity of using these microcontrollers in prosthetic knee joints can be attributed to their inclusion of the following features:

1. Processing power that are equipped with powerful processors or processor cores. This processing power enables them to handle complex computations and execute sophisticated control algorithms required for real-time control of prosthetic knee joints;
2. Memory and storage: These microcontrollers typically provide sufficient memory and storage capacities, allowing for the storage of control algorithms, sensor data, and program variables;
3. Programmability and flexibility: these microcontrollers mentioned above are programmable, allowing researchers to write and customize software code specific to the control requirements of prosthetic knee joints;
4. I/O Peripherals: microcontrollers offer various input/output (I/O) peripherals, including analog-to-digital converters, digital-to-analog converters, Pulse-Width Modulation (PWM) outputs, and serial communication interfaces. These peripherals enable seamless integration with sensors, actuators, and communication modules, facilitating sensor data acquisition, actuator control, and communication with external devices;
5. Cost-Effectiveness: many of these microcontrollers offer a cost-effective solution for prosthetic knee joint applications. They provide a balance between functionality, performance, and affordability, making them accessible for research, prototyping, and commercial development purposes;
6. Community and ecosystem support: the microcontrollers mentioned have active developer communities, and vast online resources. This support

network provides access to libraries, example codes, tutorials, and troubleshooting assistance, making the development and implementation process smoother for prosthetic knee joint control systems.

Kamel et al., utilized Arduino mega 2560 [24], while Al-Maliky et al., used EPOS2 P24/5 microcontroller from Maxon [25]. Tran et al., uses (PIC32) microcontroller to run the algorithms of the intelligent prosthetic leg [91]. AVR Atmel Mega32 microcontroller has been utilized to process the data coming from the heel strike sensor to control smart prosthetic leg [92] whereas Ochoa-Diaz et al., employed a Teensy 3 microcontroller. All authors in the selected papers did not use technologies and communication methods, such as Wi-Fi or Bluetooth where these technologies can provide advantages such as enabling wireless communication between the prosthetic knee joint and external devices or systems. For example, Wi-Fi or Bluetooth connectivity could be utilized to transmit data between the prosthetic knee joint and a mobile application or a computer for monitoring, control, or adjustment purposes.

III. Discussion and Future Perspectives

III.1. About the Mechanical Design of Intelligent Prosthetic Knee Joint

This section discusses the important factors in the mechanical design of computerized knee joints for active and semi-active prostheses, including actuator selection, material choice, numerical analysis, and mechanism design, to meet criteria such as weight, strength, range of motion, speed, cost, fatigue life, and quality. Material selection plays a crucial role in achieving these criteria, including comfort, patient fatigue, and stability.

However, the weight and cost of a smart prosthetic knee joint also depend on the actuator, which should have small dimensions to be suitable for above-knee amputees worldwide. The type of actuator used determines whether the prosthetic knee is active or semi-active. Powered prostheses using electromechanical actuation are common due to their controllability and power, but designs must also consider modes such as walking on uneven surfaces and stumbling. The prosthetic knee joint powered by a Pneumatic Artificial Muscle (PAM) exhibits a larger force-to-weight ratio than those using motors, and its elastic properties are similar to those of biological muscles. However, due to the cumbersome size and weight of the air compressor required to power the artificial muscles, this technology is currently impractical. Therefore, future research should focus on improving this aspect. It is also noteworthy that the reviewed studies only considered walking on level ground, neglecting other modes of walking such as going up and down stairs, sitting down, and standing up. Hence, future studies should address these limitations.

Variable damping actuators, especially magneto-rheological dampers, are a good alternative for semi-active control, with advantages such as small size, simple structure, low power consumption, shorter response times, and high damping force or torque range. However, the use of magneto-rheological fluid produced by other corporations or the manufacturing of new MR fluid with lower density should be studied in future works. The reviewed scientific papers demonstrate a lack of inclusivity for designs that rely on local citizens' height, and designs should consider various walking modes to restore the capability of above-knee amputees to perform their daily activities.

III.2. About the Control Method of the Intelligent Prosthetic Knee Joint

The review covered a wide range of control strategies, such as classical, force-based, adaptive, bioelectrical signal-based, and hybrid control techniques. Most researchers used the hybrid control method for the design control of an intelligent prosthetic knee joint because it offered better performance and versatility than single control methods.

Hybrid control methods can achieve specific control goals, such as stability, a smooth gait, or less energy use. By combining multiple control techniques, the nonlinearities and uncertainties in the system dynamics can be dealt with. In upper limb prosthetics, bioelectrical signal-based control has been studied a lot for decades, but there aren't many papers on EMG-based control methods in knee prosthetics. One problem with using EMG technology in knee prosthetics is that it is very sensitive to sweat and movements of the stump, which can make it hard to detect muscle activity for long periods of time. EMG signals are affected by electrode placement, muscle fatigue, and signal noise.

This can reduce the control signal's reliability and cause prosthetic knee joint control errors, to overcome these problems it is important to do studies for improving signal processing, improving electrode designs, exploring alternative bioelectrical signals like electroencephalography (EEG) or electrooculography (EOG), and combining bioelectrical signal-based control methods with force-based or adaptive control to solve these issues. These solutions can boost bioelectrical signal-based control methods' performance, reliability, and user quality of life. However, the use of EMG-based control methods offers user control in a way that is both natural and intuitive, which can lead to an overall improvement in the user's quality of life.

IV. Conclusion

In this review article, a comprehensive overview of selected papers, theses, and dissertations on the mechanical and control design of computerized prosthetic knee joints has been presented.

The papers were categorized based on their mechanical design and control design and then sub-categorized. Unlike recent review articles, this review provides a complete image of smart prosthetic knee joints, covering different types of mechanisms, materials

used for structures, types of actuators, and control methods for both active and semi-active prosthetic knee joints. The review includes an overview of all used actuators, such as variable damping and powered actuators, and numerical analysis and materials used in manufacturing. In addition, several scientific papers on control methods that provide trajectory tracking and react to the amputee's intent were reviewed, which will be valuable to researchers in the field and serve as a starting point for future work.

References

[1] Abdulameer, A., Al-Shammari, M., Fatigue Analysis of Syme's Prosthesis, (2018) *International Review of Mechanical Engineering (IREME)*, 12 (3), pp. 293-301. doi: https://doi.org/10.15866/ireme.v12i3.14390

[2] Jweeg, Muhsin J., Ahamed A. Al-Beiruti, and Kadhim K. Al-Kinani. Design and Analysis of New Prosthetic Foot. *Al-Khwarizmi Engineering Journal* 3, no. 1 (2007): 12-25.

[3] Hameed, Mohammed Ismael, and Ahmed Abdul Hussein Ali. Finite Element Design and Manufacturing of a Woven Carbon Fiber Prosthetic Foot. *Association of Arab Universities Journal of Engineering Sciences* 29, no. 2 (2022): 09-18.

[4] S. B. O'Sullivan, T. J. Schmitz, and G. Fulk, *Physical rehabilitation*, FA Davis, 2019.

[5] Z. W. Lui, M. I. Awad, A. Abouhossein, A. A. Dehghani-Sanij, and N. Messenger, Virtual prototyping of a semi-active transfemoral prosthetic leg, *Proceedings of the Institution of Mechanical Engineers, Part H: Journal of Engineering in Medicine*, vol. 229, no. 5, pp. 350-361, 2015.

[6] J. H. Campbell, P. M. Stevens, and S. R. Wurdeman, OASIS 1: Retrospective analysis of four different microprocessor knee types, *Journal of Rehabilitation and Assistive Technologies Engineering*, vol. 7, p. 2055668320968476, 2020.

[7] B. E. Lawson, H. A. Varol, A. Huff, E. Erdemir, and M. Goldfarb, Control of stair ascent and descent with a powered transfemoral prosthesis, *IEEE Transactions on Neural Systems and Rehabilitation Engineering*, vol. 21, no. 3, pp. 466-473, 2012.

[8] F. C. Sup and M. Goldfarb, Design of a pneumatically actuated transfemoral prosthesis, in *ASME International Mechanical Engineering Congress and Exposition*, vol. 47683, pp. 1419-1428, 2006.

[9] M. R. Tucker et al., Control strategies for active lower extremity prosthetics and orthotics: a review, *Journal of Neuroengineering and Rehabilitation*, vol. 12, no. 1, pp. 1-30, 2015.

[10] M. A. Price, P. Beckerle, and F. C. Sup, Design optimization in lower limb prostheses: A review, *IEEE Transactions on Neural Systems and Rehabilitation Engineering*, vol. 27, no. 8, pp. 1574-1588, 2019.

[11] F. M. Kadhim, J. S. Chiad, and A. M. Takhakh, Design and manufacturing knee joints for a smart transfemoral prosthesis, in *IOP Conference Series: Materials Science and Engineering*, vol. 454, no. 1, p. 012078, IOP Publishing, 2018.

[12] S. H. Kamel, M. N. Hamzah, Q. A. Atiyah, and S. A. Abdulateef, Modeling and Analysis of a Novel Smart Knee Joint Prosthesis for Transfemoral Amputation, in *IOP Conference Series: Materials Science and Engineering*, vol. 1094, no. 1, p. 012109, IOP Publishing, 2021.

[13] H. Saad, M. Q. Abdullah, and H. R. Wasmi, The Modeling and Effect of FEM on Prosthetic limb, *International Journal of Current Engineering and Technology*, vol. 7, no. 3, pp. 892-895, 2017.

[14] M. Liu, P. Datseris, and H. H. Huang, A prototype for smart prosthetic legs-analysis and mechanical design, in *Advanced Materials Research*, vol. 403, pp. 1999-2006, Trans Tech Publications Ltd., 2012.

[15] M. Liu, F. Zhang, P. Datseris, and H. H. Huang, Improving finite state impedance control of active-transfemoral prosthesis using dempster-Shafer based state transition rules, *Journal of Intelligent & Robotic Systems*, vol. 76, no. 3, pp. 461-474, 2014.

[16] Z. Liu, W. Lin, Y. Geng, and P. Yang, Intent pattern recognition of lower-limb motion based on mechanical sensors, *IEEE/CAA Journal of Automatica Sinica*, vol. 4, no. 4, pp. 651-660, 2017.

[17] W. Cao, H. Yu, W. Chen, Q. Meng, and C. Chen, Design and evaluation of a novel microprocessor-controlled prosthetic knee, *IEEE Access*, vol. 7, pp. 178553-178562, 2019.

[18] K. Li, J. Zhang, L. Wang, M. Zhang, J. Li, and S. Bao, A review of the key technologies for sEMG-based human-robot interaction systems, *Biomedical Signal Processing and Control*, vol. 62, 102074, 2020.

[19] R. K. Mohanty, R. C. Mohanty, and S. K. Sabut, Application of control strategies and machine learning techniques in the prosthetic knee: a systematic review, *Advances in Computational Intelligence*, vol. 2, no. 1, pp. 1-15, 2022.

[20] Geng, Y., Xu, X., Chen, L., & Yang, P. (2010, November). Design and analysis of active transfemoral prosthesis. In IECON 2010-36th *Annual Conference on IEEE Industrial Electronics Society (pp. 1495-1499). IEEE*.

[21] Vadiati, A., Bagheri, A., Mahjoob, M., & Sadigh, M. (2018). Design, control, and prototype a series elastic actuator for an active knee orthosis. *Engineering Solid Mechanics*, 6(3), 241-252.

[22] Haddadin, S., Mansfeld, N., & Albu-Schäffer, A. (2012, October). Rigid vs. elastic actuation: Requirements & performance. In 2012 *IEEE/RSJ International Conference on Intelligent Robots and Systems (pp. 5097-5104). IEEE*.

[23] Awad, M. I., Abouhossein, A., Dehghani-Sanij, A. A., Richardson, R., Querin, O. M., Moser, D., & Zahedi, S. (2015). Estimation of Prosthetic Knee Actuation System Requirements. *IEEE Transactions on Neural Systems and Rehabilitation Engineering*, 23(6), 976-984.

[24] Kamel, S. H., Hamzah, M. N., Atiyah, Q. A., & Abdulateef, S. A. (2021, February). *Design and manufacture of a smart knee joint for a transfemoral amputation*. Dissertation in Mechanical Engineering department, University of Technology, Iraq.

[25] Al-Maliky, F. T., & Chiad, J. S. (2022). *Design and analysis of intelligent prosthetic knee joint and its comparison with the commercial knees*, Dissertation in Mechanical Engineering department, Al-Nahrain University, Iraq.

[26] Hoover, C. D., Fulk, G. D., & Fite, K. B. (2012). Stair ascent with a powered transfemoral prosthesis under direct myoelectric control. *IEEE/ASME Transactions on Mechatronics*, 18(3), 1191-1200.

[27] El-Sayed, A. M., Hamzaid, N. A., & Osman, N. A. A. (2014). Modeling and control of a linear actuated transfemoral knee joint in basic daily movements. *Applied Mathematics and Information Sciences*, 7, 1-11.

[28] B. Jo and Y. S. Lee, "Design and Control of an Active Powered Knee Prosthesis System using Position-based Impedance Control," *in Proceedings of the 3rd World Congress on Mechanical, Chemical, and Material Engineering (MCM'17), 2017*.

[29] R. Borjian, J. Lim, M. B. Khamesee, and W. Melek, The design of an intelligent mechanical active prosthetic knee, in 2008 *34th Annual Conference of IEEE Industrial Electronics*, pp. 3016-3021, Nov. 2008.

[30] F. Valencia, D. Ortiz, and D. Ojeda, Design and testing of low-cost knee prosthesis, *in 2017 IEEE Second Ecuador Technical Chapters Meeting (ETCM), pp. 1-6, Oct. 2017*.

[31] M. R. Islam, A. M. Haque, S. N. Amin, and K. S. Rabbani, Design and development of an EMG driven microcontroller based prosthetic leg, *Bangladesh Journal of Medical Physics*, vol. 4, no. 1, pp. 107-114, 2011.

[32] E. C. Martinez-Villalpando and H. Herr, Agonist-antagonist active knee prosthesis: a preliminary study in level-ground walking, *Journal of Rehabilitation Research & Development*, vol. 46, no. 3, 2009.

[33] E. J. Rouse, L. M. Mooney, and H. M. Herr, Clutchable series-elastic actuator: Implications for prosthetic knee design, *The International Journal of Robotics Research*, vol. 33, no. 13, pp. 1611-1625, 2014.

[34] S. Jannati, S. M. Ayati, and A. Yousefikoma, Designing and Implementation of an Online Control Interface for Knee Prosthesis Based on Electromyography Signals, *Modares Mechanical Engineering*, vol. 20, no. 6, pp. 1435-1448, 2020.

[35] F. Peng, H. Wen, C. Zhang, B. Xu, J. Li, and H. Su, Adaptive robust force position control for flexible active prosthetic knee using gait trajectory, *Applied Sciences*, vol. 10, no. 8, pp. 2755, 2020.

[36] G. C. Waycaster, *Design of a powered above knee prosthesis using pneumatic artificial muscles*, The University of Alabama, 2010.

[37] Y. Dabiri, S. Najarian, M. R. Eslami, S. Zahedi, and D. Moser, A powered prosthetic knee joint inspired from the musculoskeletal system, *Biocybernetics and Biomedical Engineering*, vol. 33, no. 2, pp. 118-124, 2013.

[38] A. M. A. Soliman and M. M. S. Kaldas, Semi-active suspension systems from research to mass-market–A review, *Journal of Low-Frequency Noise, Vibration and Active Control*, vol. 40, no. 2, pp. 1005-1023, 2021.

[39] B. G. Lambrecht and H. Kazerooni, Design of a semi-active knee prosthesis, in *2009 IEEE International Conference on Robotics and Automation*, May 2009, pp. 639-645.

[40] X. Wang, Q. Meng, and H. Yu, Design and Preliminary Testing of a Novel Variable-Damping Prosthetic Knee, *IETE Journal of Research*, vol. 67, no. 3, pp. 407-414, 2021.

[41] W. Cao, H. Yu, W. Zhao, J. Li, and X. Wei, Target of physiological gait: Realization of speed adaptive control for a prosthetic knee during swing flexion, *Technology and Health Care*, vol. 26, no. 1, pp. 133-144, Jan. 2018.

[42] R. Dedić, F. Ustamujić, Z. Jelačić, Ž. Husnić, and V. Kvesić, Concept design and design optimization of the transfemoral prosthetic leg prototype, *IOP Conference Series: Materials Science and Engineering*, vol. 1208, no. 1, p. 012017, Nov. 2021.

[43] M. V. Pillai, H. Kazerooni, and A. Hurwich, Design of a semi-active knee-ankle prosthesis, in 2011 *IEEE International Conference on Robotics and Automation*, May 2011, pp. 5293-5300.

[44] F. Sup, A. Bohara, and M. Goldfarb, Design and control of a powered knee and ankle prosthesis, in *Proceedings 2007 IEEE International Conference on Robotics and Automation*, April 2007, pp. 4134-4139.

[45] T. Orhanlı and A. Yılmaz, Finite State Control of the semi-active knee joint with pneumatic damper, in 2014 *18th National Biomedical Engineering Meeting*, Oct. 2014, pp. 1-5.

[46] F. Imaduddin, S. A. Mazlan, and H. Zamzuri, A design and modeling review of the rotary magneto-rheological damper, *Materials & Design*, vol. 51, pp. 575-591, Jan. 2013.

[47] J. D. Carlson, W. Matthis, and J. R. Toscano, Smart prosthetics based on magneto-rheological fluids, in *Smart structures and materials 2001: industrial and commercial applications of smart structures technologies*, vol. 4332, June 2001, pp. 308-316.

[48] G. C. Nandi, A. J. Ijspeert, V. Soneker, and A. Nandi, Developing Hardware-Software Suite for AMAL-Adaptive Modular Active Leg, in *Disability Rehabilitation Management Through ICT*, River Publishers, 2022, pp. 111-138.

[49] F. Li, H. Xie, W. Yuan, and Y. Liu, The application research of MR damper in the intelligent bionic leg, in *2009 Chinese Control and Decision Conference*, IEEE, June 2009, pp. 1327-1331.

[50] C. Ochoa-Diaz, T. S. Rocha, L. de Levy Oliveira, M. G. Paredes, R. Lima, A. P. L. Bó, and G. A. Borges, An above-knee prosthesis with magneto-rheological variable-damping, in *5th IEEE RAS/EMBS International Conference on Biomedical Robotics and Biomechatronics*, IEEE, August 2014, pp. 108-113.

[51] O. Arteaga, A. Cevallos, M. I. Erazo, K. D. Morales, D. B. Tenezaca, and E. M. Argüello, Application of magneto-rheological fluids in the design of a leg prosthesis with active damping, in *MATEC Web of Conferences*, vol. 192, EDP Sciences, 2018, p. 02055.

[52] G. Shastry, A. Toby, S. B. Choi, V. G. Kamble, and T. Jagadeesha, Design, Modeling, and Simulation of Low-Cost Magneto-rheological Fluid-Based Prosthetic Leg, in *Recent Advances in Manufacturing Processes and Systems*, Springer, Singapore, 2022, pp. 281-294.

[53] Ç. Akalın, T. Orhanlı, A. Yılmaz, and İ. Şahin, Dynamic tests of MR (Magneto rheologic) damper and analysis of response characteristics in a semi-active knee prosthesis, in *2017 25th Signal Processing and Communications Applications Conference (SIU)*, IEEE, May 2017, pp. 1-4.

[54] J. H. Kim and J. H. Oh, Development of an above knee prosthesis using MR damper and leg simulator, in *Proceedings 2001 ICRA. IEEE International Conference on Robotics and Automation (Cat. No. 01CH37164)*, vol. 4, IEEE, May 2001, pp. 3686-3691.

[55] H. Herr and A. Wilkenfeld, User-adaptive control of a magneto-rheological prosthetic knee, *Industrial Robot: An International Journal*, vol. 30, no. 4, pp. 323-330, 2003.

[56] K. H. Gudmundsson, F. Jonsdottir, and F. Thorsteinsson, A geometrical optimization of a magneto-rheological rotary brake in a prosthetic knee, *Smart Materials and Structures*, vol. 19, no. 3, p. 035023, 2010.

[57] Al-Shammari, M., & Abd Alameer, A. K. (2018). Material characterization and fatigue analysis of lower limb prosthesis materials. *Association of Arab Universities Journal of Engineering Sciences*, 25(3), 137-154.

[58] Al-Shammari, Mohsin Abdullah, and Sahar Emad Abdullah. Stiffness to weight ratio of various mechanical and thermally loaded hyper composite plate structures. In *IOP Conference Series: Materials Science and Engineering*, vol. 433, no. 1, p. 012051. IOP Publishing, 2018.

[59] Jweeg, Muhsin J., Samira K. Radhi, and Haider F. Neama. An experimental comparative study between polypropylene and laminated lower limb prosthetic socket. *Al-Khwarizmi Engineering Journal* 3, no. 1 (2007): 40-46.

[60] M. A. Al-Shammari and A. K. Abdulameer, Parametric Analysis to Investigate the Stiffness to Weight Ratio of Syme's Socket, *International Journal of Current Engineering and Technology*, vol. 8, no. 1, 2018, pp. 57-62.

[61] J. Lim, *The mechanical design and analysis of an active prosthetic knee* (Master's thesis, University of Waterloo, Waterloo, ON, Canada, 2008).

[62] M. Sayem and H. Bhuiyan, *Design and development of mechanically controlled above knee prosthesis* (Doctoral dissertation, University of Malaya, Kuala Lumpur, Malaysia, 2017).

[63] S. K. Wu, *Lower-limb robotic devices: Controls and design* (Doctoral dissertation, University of Alabama Libraries, Tuscaloosa, AL, USA, 2012).

[64] R. R. Torrealba, L. A. Zambrano, E. Andara, G. Fernández-López, and J. C. Grieco, Medium-cost electronic prosthetic knee for transfemoral amputees: a medical solution for developing countries, in *World Congress on Medical Physics and Biomedical Engineering, September 7-12, 2009, Munich, Germany*, Berlin, Heidelberg, Springer, 2009, pp. 456-459.

[65] S. Bhatt, A. Godiyal, D. Joshi, and P. K. Rakesh, Design Analysis and Fatigue Life Prediction of an Indigenously Developed Affordable Knee Prosthesis, in *Advances in Engineering Design*, Singapore, Springer, 2021, pp. 3-13.

[66] M. I. Saleem, M. U. Qadir, I. ul Haq, N. Akhtar, M. T. Afridi, and K. Shah, Self-Adjustable Intelligent Knee Mimicking the Real Human Gait-Cycle Using Machine Learning, in *2020 International Conference on Electrical, Communication, and Computer Engineering (ICECCE)*, IEEE, 2020, pp. 1-5.

[67] K. H. Yusof, M. A. Zulkipli, A. S. Ahmad, M. F. Yusri, S. Al-Zubaidi, and M. N. Mohammed, Design and Development of a Prosthetic Leg with a Mechanical System, in *2021 IEEE 12th Control and System Graduate Research Colloquium (ICSGRC)*, IEEE, 2021, pp. 217-221.

[68] P. R. Cavanagh and P. V. Komi, Electromechanical delay in human skeletal muscle under concentric and eccentric contractions, *European journal of applied physiology and occupational physiology*, vol. 42, no. 3, 1979, pp. 159-163.

[69] D. Jin, J. Yang, R. Zhang, R. Wang, and J. Zhang, Terrain identification for prosthetic knees based on electromyographic signal features, *Tsinghua Science and Technology*, vol. 11, no. 1, 2006, pp. 74-79.

[70] S. K. Wu, G. Waycaster, and X. Shen, Active knee prosthesis control with electromyography, in *Dynamic Systems and Control Conference*, IEEE, 2010, pp. 785-791.

[71] E. Shultz and J. Desai, Design of an EMG Driven Bionic Prosthetic for Transfemoral Amputees, *IEEE Transactions on Neural Systems and Rehabilitation Engineering*, vol. 18, no. 1, pp. 1-9, Feb. 2010.

[72] R. Chereshnev and A. Kertész-Farkas, GaIn Human gait inference

for lower limbic prostheses for patients suffering from double trans-femoral amputation, *Sensors*, vol. 18, no. 12, p. 4146, Dec. 2018.
[73] G. Chen, Z. Liu, L. Chen, and P. Yang, Control of powered knee joint prosthesis based on finite-state machine, *in Proceedings of the Chinese Intelligent Automation Conference*, Z. Deng and H. Li, Eds. Springer-Verlag Berlin Heidelberg, 2015, pp. 395-403.
[74] J. Park, G. H. Yoon, J. W. Kang, and S. B. Choi, Design and control of a prosthetic leg for above-knee amputees operated in semi-active and active modes, *Smart Materials and Structures*, vol. 25, no. 8, p. 085009, Jul. 2016.
[75] R. C. Martinez, R. L. Avitia, M. E. Bravo, and M. A. Reyna, A low-cost design of powered ankle-knee prosthesis for lower limb amputees, in *Proceedings of the BIODEVICES-2014*, 2014, pp. 253-258.
[76] M. Awad, K. S. Tee, A. A. Dehghani-Sanij, D. Moser, and S. Zahedi, Analysis and performance of a semi-active prosthetic knee, in *Proceedings of the International Conference on Mechanical Engineering and Mechatronics (ICMEM 2012)*, Aug. 2012, p. 213.
[77] F. Sup, A. Bohara, and M. Goldfarb, Design and control of a powered transfemoral prosthesis, *The International Journal of Robotics Research*, vol. 27, no. 2, pp. 263-273, Feb. 2008.
[78] S. Pandit, A. K. Godiyal, A. K. Vimal, U. Singh, D. Joshi, and D. Kalyanasundaram, An affordable insole-sensor-based trans-femoral prosthesis for normal gait, *Sensors*, vol. 18, no. 3, p. 706, Mar. 2018.
[79] C. Kim, J. J. Lee, and X. Xu, Design of Biped Robot with Heterogeneous Legs for an advanced prosthetic knee application, in *2006 SICE-ICASE International Joint Conference*, Oct. 2006, pp. 1852-1855.
[80] K. S. Mahmood, A. I. Hasan, S. Iqbal, S. Pal, and M. I. Tahmid, Design and Control of an Electrically Powered Knee Prosthesis by Taking Feedback from a Fully Functional Leg, *Proceedings of the International Conference on Industrial & Mechanical Engineering and Operations Management* Dhaka, Bangladesh, December 26-27, 2020.
[81] G. Merewether and T. H. Hsieh, *Impedance Control of a Knee-Ankle Prosthesis*.
[82] Herr, Hugh, and Ari Wilkenfeld. User-adaptive control of a magnetorheological prosthetic knee. *Industrial Robot: An International Journal* 30, no. 1 (2003): 42-55.
[83] B. E. Lawson, J. Mitchell, D. Truex, A. Shultz, E. Ledoux, and M. Goldfarb, A robotic leg prosthesis: Design, control, and implementation, *IEEE Robotics & Automation Magazine*, vol. 21, no. 4, pp. 70-81, 2014.
[84] Ekkachai, Kittipong, and Itthisek Nilkhamhang. Swing phase control of semi-active prosthetic knee using neural network predictive control with particle swarm optimization. *IEEE Transactions on Neural Systems and Rehabilitation Engineering* 24, no. 11 (2016): 1169-1178.
[85] Q. Fu, D. H. Wang, L. Xu, and G. Yuan, A magneto-rheological damper-based prosthetic knee (MRPK) and sliding mode tracking control method for an MRPK-based lower limb prosthesis, *Smart Materials and Structures*, vol. 26, no. 4, pp. 045030, 2017.
[86] Sharma, Richa, Prerna Gaur, Shaurya Bhatt, and Deepak Joshi. "Performance assessment of fuzzy logic control approach for MR-damper based-transfemoral prosthetic leg. *IEEE Transactions on Artificial Intelligence* 3, no. 1 (2021): 53-66.
[87] Nordin, NH Diyana, Asan GA Muthalif, M. Khusyaie M. Razali, Abdelrahman Ali, and Ayman Mustafa Salem. "Development and implementation of energy-efficient Magnetorheological Fluid bypass damper for prosthetics limbs using a fuzzy-logic controller. *IEEE Access* 10 (2022): 18978-18987.
[88] Raheema, Mithaq N., Dhirgaam A. Kadhim, and Jabbar S. Hussein. Design an intelligent hybrid position/force control for above knee prosthesis based on adaptive neuro-fuzzy inference system. *Indones. J. Electr. Eng. Comput. Sci* 23 (2021): 675-685.
[89] Ha, Kevin H., Huseyin Atakan Varol, and Michael Goldfarb. "Myoelectric control of a powered knee prosthesis for volitional movement during non-weight-bearing activities. In *2010 Annual International Conference of the IEEE Engineering in Medicine and Biology*, pp. 3515-3518. IEEE, 2010.
[90] Huang, He, Todd A. Kuiken, and Robert D. Lipschutz. A strategy for identifying locomotion modes using surface electromyography. *IEEE Transactions on Biomedical Engineering* 56, no. 1 (2008): 65-73.
[91] Tran, Minh, Lukas Gabert, Sarah Hood, and Tommaso Lenzi. A lightweight robotic leg prosthesis replicating the biomechanics of the knee, ankle, and toe joint. *Science Robotics* 7, no. 72 (2022): eabo3996.
[92] Nandy, Anup, Soumik Mondal, Pavan Chakraborty, and Gora Chand Nandi. Development of a robust microcontroller based intelligent prosthetic limb. In *Contemporary Computing: 5th International Conference*, IC3 2012, Noida, India, August 6-8, 2012. Proceedings 5, pp. 452-462. Springer Berlin Heidelberg, 2012.
[93] Ochoa-Diaz, Claudia, Thiago S. Rocha, Lucas de Levy Oliveira, Miguel G. Paredes, Rafael Lima, Antônio Padilha L. Bó, and Geovany A. Borges. An above-knee prosthesis with magnetorheological variable-damping. In *5th IEEE RAS/EMBS International Conference on Biomedical Robotics and Biomechatronics*, pp. 108-113. IEEE, 2014.

Authors' information

University of Baghdad, Iraq.

Ahmed Khaleel Abdulameer, born on December 28, 1979, is currently a PhD student in the Mechanical Engineering Department at the College of Engineering, University of Baghdad. He obtained his undergraduate degree from Al-Mustansiriya University in 2003. His research interests are related to biomedical Engineering. Ahmed's primary area of interest lies in the field of Prosthetics.
E-mail: mecahmed15@gmail.com

Prof. Dr. **Mohsin Abdullah Al-Shammari** was born in Baghdad, Iraq. He received the B.Sc. degree in mechanical engineering from the University of Baghdad, in 1992, M.Sc. in mechanical engineering in 1997 from the University of Baghdad and the Ph.D. degree in mechanical engineering in 2010. He was professor in applied mechanics from 2019 till now at the university of Baghdad, college of engineering, Mechanical engineering department. With expertise in the fields of Prostheses and Orthoses, Mechanical Vibrations, and Composite Materials, he has made significant contributions to these areas through his extensive research and publications.
E-mail: dr.alshammari@uobaghdad.edu.iq

International Review of Automatic Control (IREACO)

Aims and scope

The **International Review of Automatic Control (IREACO)** is a peer-reviewed journal that publishes original theoretical and applied papers on all aspects of Automatic Control. The topics to be covered include, but are not limited to:

Control of linear/nonlinear systems, Stability, Controllability and Observations, Modeling Estimation and Prediction, Real-Time Systems control, Real-Time and Fault-Tolerant Systems, Multidimensional Systems control, Large Scale Control Systems, Robust Control, Intelligent Control Systems; Stochastic Control, Fuzzy Control Systems, Neuro-Controllers, Neuro-Fuzzy Controllers, Genetic Algorithms, Adaptive Control Techniques; Control methods, modelling and identification of processes in the fields of industry, ecology, natural resources, including physical, biological and organizational systems; the coverage includes but are not limited to: Power System Control, Automatic Control of Chemical Processes, Automotive Control Systems, Thermal System Control, Robot and Manipulator Control, Process Control, Aerospace Control Systems, Motion and Navigation Control, Traffic and Transport Control, Defense and Military Systems Control, Studies on nuclear systems control, Control analysis of Social and Human Systems, Biomedical control systems.

Instructions for submitting a paper

Contributions may consist of invited tutorials or critical reviews; original scientific research papers (regular paper); letters to the Editor and research notes which should also be original presenting proposals for a new research, reporting on research in progress or discussing the latest scientific results in advanced fields.
All papers will be subjected to a fast editorial process.
Any paper will be published within two months from the submitted date, if it has been accepted.

Papers must be correctly formatted, in order to be published.
An ***Author guidelines*** template file can be found on our web site:

www.praiseworthyprize.org/jsm/?journal=ireaco

Manuscripts should be sent on-line or via e-mail as attachment in .doc and .pdf formats to:

editorialstaff@praiseworthyprize.com

Abstracting and Indexing Information:

Academic Search Complete (EBSCO Information Services)
Cambridge Scientific Abstracts (CSA/CIG)
Elsevier Bibliographic Database SCOPUS
ProQuest
Index Copernicus - IC Journal Master List 2021: ICV 116.69

Autorizzazione del Tribunale di Napoli n. 54 del 08/05/2008

2533-2260(202303)16:2;1-#